공학박사학위논문

역제동 흡수식 레이저 펄스 폭 변조를 사용한 레이저 유도 플라스마 분광법에 관한 연구

A study of laser-induced plasma spectroscopy using inverse-Bremsstrahlung pulse-width modulation

2021 년 2 월

서울대학교 대학원

기계항공공학부

오 성 균

Abstract

A study of laser-induced plasma spectroscopy using inverse-Bremsstrahlung pulse-width modulation

Sungkyun Oh
Department of Mechanical and Aerospace Engineering
The Graduate School
Seoul National University

Laser-induced breakdown spectroscopy (LIBS) is a quantitative optical measurement method providing composition and density information within nanoseconds (ns) timescale. Compared to other laser-based measurement techniques, LIBS requires a simpler optical setup, single optical access window, and lower input laser energy, but provides better signal strength. The LIBS signal is based on light-emission from plasma created by an optical breakdown at the measurement target. Optical breakdown in neutral dielectric gas accompanies rapid electron production through photon-molecule, photon-electron, and electron-molecule interactions, which results in high electron number density above a critical value. Subsequently, the seed electrons rapidly absorb optical energy in the inverse-Bremsstrahlung (IB) process. For non-intrusive LIBS measurements, however, the IB process should be limited; thus, the laser pulse width needs to be reduced below a certain value. In general, the pulse width of high-power lasers capable of inducing plasma breakdown is not variable, and the ns-laser system is commonly used for LIBS measurements. Therefore, applications of LIBS have been limited, for example, to the fuel mixtures outside the explosive and flammable range, or in post-reaction products.

In this study, a newly devised laser pulse control technique is developed to provide sub-ns pulses of the proper pulse width. The laser pulse generated

from a commercially available ns-laser source is focused into a pressure cell to induce gas breakdown. Prior to the breakdown at the cell, air at the focus is perfectly transparent to the laser beam. However, the intense IB photon absorption suddenly makes the medium opaque, acting as a *virtual shutter*. It is shown that the shutter time is controllable primarily by the cell pressure. Similarly, by increasing the number of photons passing through the focal volume the breakdown delay can be adjusted to close the shutter earlier. In this work, a correlation of the "closing time" dependence is established and verified with experimental results.

The laser pulse control technique is applied to develop a non-intrusive LIBS measurement. In conventional LIBS, the IB-induced gas heating causes unwanted disturbances to the measurement target by inducing initiation and/or amplification of chemical reactions, pressure waves, and rapid temperature rise; and in this respect the LIBS measurement is *intrusive*. Nevertheless, LIBS also require sufficiently strong plasma emission for quantitative measurements. Thus, the laser pulse-width modulation technique is applied to generate a sub-ns pulse, which can induce gas breakdown stably while providing a sufficiently strong emission signal. The result showed that while the IB process can effectively raise the signal strength, the IB process can be limited by reducing the laser pulse duration. Additionally, the new LIBS diagnostic offers higher SNR compared to conventional methods with improved spatiotemporal resolution.

The feasibility of the proposed minimally-intrusive LIBS technique is demonstrated in a highly flammable environment. The potential for cold-gas probing is proven with measurements (i.e., not causing ignition) of highly-flammable flow. The modulated pulses are used for LIBS, and the 2D concentration distribution of a stoichiometric laminar methane-air flow in ambient air is recorded.

Keywords: Laser-induced plasma, Optical diagnostics, Laser pulse-width, Pulse-width modulation, Plasma spectroscopy

Student Number: 2015-22716

Contents

List of Figures

List of Tables

Nomenclature

A_{ij}	Einstein coefficient [s^{-1}]
E	laser pulse energy [J]
f	focal length [m]
g_j	energy state degeneracy [-]
h	Plank constant [J s]
I	photon intensity [W m^{-2}]
n_e	electron number density [m^{-3}]
N	neutral molecule number density [m^{-3}]
P	pressure [N m^{-2}]
R^2	coefficient of determination [-]
S_L	laminar flame speed [m s^{-1}]
t	time [s]
T	temperature [K]
U	flow speed [m s^{-1}]

Greek letters

γ	heat capacity ratio [-]
ε	emission coefficient [J m^{-3} s^{-1}]
λ	wavelength [m]
ν	photon frequency [Hz]
ρ	gas density [kg m^{-3}]
τ	laser pulse width [s]
ϵ	ionization potential [J mol^{-1}]
ϕ	equivalence ratio [-]

Subscripts

ad	adiabatic
bd	breakdown
c	critical electron density
cc	cascade
d	camera gate delay
e	electron
i	ionization
in	inlet
m	integer part of multi-photon interaction
p	laser pulse
w	camera gate width

Acronyms

APE	absorbed pulse energy
FL	focal lens
FWHM	full-width at half maximum
IB	inverse-Bremsstrahlung
IS	integrating sphere
LIBS	laser-induced breakdown spectroscopy
LTE	local thermodynamic equilibrium
MPI	multi-photon ionization
PAD	photon absorption delay
PIR	peak intensity ratio
ROI	region of interest
SA	saturable absorber
SNR	signal-to-noise ratio
UV	ultraviolet

Acknowledgment of Copyright

Part of chapter 1&2 is reprinted and adapted with permission from The Optical Society© upon request.

As per the publisher's copyright policy, the materials in [1] including the dedicated sections, figures, and tables are all retained by the first author and allowed to be posted in the web-version of the dissertation with full acknowledgment of its original publication in the OSA journal.

Part of chapter 1&4&5 is reprinted and adapted with permission from Elsevier©.

As per the publisher's copyright policy, the materials in [2] including the dedicated sections, figures, and tables are all retained by the first author and allowed to be posted in the web-version of the dissertation with full acknowledgment of its original publication in the Elsevier journal.

Part of chapter 5 is reprinted and adapted with permission from Elsevier©.

As per the publisher's copyright policy, the materials in [3] including the dedicated sections, figures, and tables are all retained by the first author and allowed to be posted in the web-version of the dissertation with full acknowledgment of its original publication in the Elsevier journal.

The author confirms that the copyrighted materials were not reproduced from any other source when published in their original publication.

Chapter 1 Introduction

1.1 Background & Motivation

Laser-induced breakdown spectroscopy (LIBS) is a quantitative optical measurement method providing composition and density information that can be extracted from emission spectra of laser-induced plasmas. To generate plasmas of sufficient photon emission, high-power nanosecond-to-femtosecond laser pulses are focused, causing dissociation and photo-ionization in the solid, liquid, or gaseous target medium. The plasma emission is then collected by a spectrometer to provide instantaneous emission spectra. Compared to other laser-based techniques (e.g. spontaneous Raman scattering [4]), LIBS requires a simpler optical setup, single optical access point (e.g., a single window), and lower input laser energy, but provides a higher signal-to-noise ratio (SNR). Therefore, this optical technique has been widely used for composition analysis [5, 6] and can potentially be employed in extreme conditions, including space exploration [7, 8] and nuclear detection [9, 10]. Moreover, real-time gas composition and density monitoring in high-temperature combustion environments is enabled by LIBS. For example, the local equivalent fuel-air (F/A) ratio was monitored in flames and combustion products [11-14], power-plant combustors [15, 16], and propulsion systems [17-20].

The LIBS signal is from the plasma created by an optical breakdown at the measurement target location. Dynamics of the plasma are found to be strongly dependent on the laser pulse characteristics such as wavelength [21-23] and pulse energy [24-26] that determine plasma temperature, electron density, and photon emission intensity. It was also revealed that the temporal width of the focused laser pulse is one of the major factors affecting the plasma behavior, particularly via the dominant photon-matter interaction mechanism [27-33]. For example, the inverse-

Bremsstrahlung (IB) process is the primary photon absorption mechanism with focused nanosecond (ns) laser pulses in atmospheric conditions. Free electrons absorb photon energy much faster than heavy particles (atoms and molecules) through the IB process and are thereby quickly accelerated; subsequently, the electrons collide with and ionize the heavy particles. When the IB process dominates the photon-matter interaction, the breakdown plasma is accompanied by rapid and significant gas heating. The abrupt gas temperature rise in the plasma is due to the collisions with the high-temperature free electrons absorbing the laser photon energy; the typical electron-neutral collision time scale at relevant conditions is on the order of 1 – 100 picoseconds (ps) [29-31]. Accordingly, strong broadband emission appears during the IB process. Therefore, quantifiable spectral features, which are essential for LIBS measurements, are captured at least a few tens of nanoseconds after the laser radiation is terminated to avoid the broadband emission.

On the other hand, femtosecond (fs) laser-induced plasmas do not induce such intense heating [29, 30], and the broadband (Bremsstrahlung) emission can be greatly suppressed [27]. In this case, multiphoton ionization (MPI) and tunneling ionization play a major role in electron production and photon absorption [29], while the electron number density is not high enough for the IB process to dominate the photon absorption mechanism. Plasmas induced by focused ps-laser pulses absorb the laser photon energy primarily through the IB process near the end of the pulse duration [32]; therefore, the plasma density (or electron number density) can be greatly elevated by the IB process that prompts cascade ionization, although the gas heating is much less than that in ns-laser induced plasmas. Consequently, it is evident that the laser pulse width, which can limit or intensify the IB process, directly influences the fraction or amount of the absorbed laser pulse energy (APE) and gas heating. It is clear that the LIBS diagnostic using focused ns-laser pulses capable of igniting flammable mixtures cannot be used to monitor the properties of flammable reactants.

1.2 Literature Review

Noack [33] showed that the APE in water differs with varying pulse width, which alters the dominating photon absorption mechanism. In another recent study utilizing fs-laser pulses for combustion diagnostics [34], it was reported that an extremely small fraction of the laser pulse energy (<1%) was deposited in the plasma filamentation volume, while over 80% of pulse energy was absorbed in ns-laser-induced plasmas [24, 26, 31]. As the fraction of APE increases with the IB process activated, the measurement target species will significantly be heated, eventually causing remarkable fluid disturbances, chemical reformation and reactions. In flammable mixtures, the IB-induced gas heating can initiate combustion chain reactions [24]. It was reported that a high-temperature (4,000 K - 10,000 K) region persisted up to 20 μs after the gas breakdown induced by ns-laser pulses [35], which is more than sufficient for combustion ignition. Nevertheless, for non-intrusive LIBS measurements, particularly in flammable mixtures, the IB process should be limited; thus, the laser pulse width needs to be reduced below a certain value. Of course, when the pulse energy absorption is low, the population of the electronically excited species may be too low for sufficient SNR [27]. Considering that the photon energy absorption and the plasma density are also a function of gas condition (such as the density and composition [20]), the proper laser pulse width for minimizing the perturbations but inducing sufficient emission signal also depends on the target gas condition. However, the pulse width of high-power lasers capable of causing optical breakdown is not variable in general, and ns-lasers are most commonly used for LIBS measurements and widely available across the globe. Therefore, LIBS applications in combustion environments have been limited in fuel mixtures outside the flammable range [6, 36] or combustion products [11, 12, 15, 17, 19]. Meanwhile, fuel probing in flammable reactants prior to burning is essential for monitoring the fuel-air mixing quality in the reactants, which is a dominant factor determining

combustion stability and efficiency. Therefore, various numerical [37-39] and experimental [40-43] works have attempted to provide accurate fuel concentration profiles in reactants.

Spontaneous Raman [44] and Rayleigh scattering [45, 46], on the other hand, can be used for non-reacting fuel concentration measurements in flammable mixtures, and both are "standard", often excellent, tools for gas-phase diagnosis. However, the output signal of the two methods is relatively weak (~1/1000 of typical LIBS signals), due to the small scattering cross-sections, and can thus be obscured by unintended laser-induced fluorescence (of molecules in the probing location) and even by flame chemiluminescence. Both techniques typically require high laser pulse energy (especially Raman scattering)—which can likewise exacerbate fluorescence interferences—to compensate for the low scattering cross-sections, as well as spatiotemporal beam shaping (in some cases) to prevent optical breakdown and damage to optical-access windows. Furthermore, while Rayleigh scattering cross-sections are significantly higher than spontaneous Raman scattering cross-sections (and thus SNRs with Rayleigh scattering are generally significantly higher), Rayleigh scattering, unlike Raman scattering, is susceptible to stray scattering interferences from particles and surfaces, which can make its application challenging except to clean, dust-free, and idealized environments. Filtered Rayleigh scattering [47] (FRS) has been used to suppress surface and particle scattering but generally requires the use of an injection-seeded or single-mode laser source (with frequency tunability) as well as some atomic or molecular absorption filter, which will necessarily reduce the gas scattering signal and thus SNR.

The experimental investigation conducted by Espey et al. [45] reported fuel concentration measurements in a diesel spray using planar Rayleigh scattering. The scattering cross-section of the evaporated diesel fuel is 305 times greater than that of the air; therefore, the scattering from the air becomes negligible in the non-reacting spray jet condition. Even with the remarkably enhanced scattering signal due to the large scattering cross-section of the target fuel species, the output signal is still not

strong enough to ignore the background light that raised the measurement uncertainty up to 17 - 21% in the study. It was also shown that the unwanted interference signals from Mie scattering and stray background are typically one or two orders of magnitude (x 10-100) stronger than the output signal. In addition, the influences of the reflection/absorption by optical access windows, and uncertainties from laser pulse energy variation and beam path steering are all non-negligible due to the weak output signal intensity.

On the other hand, filtered Rayleigh scattering (FRS) utilizing a high-power pulse laser source and an iodine filter was employed for fuel concentration measurements when the difference between the scattering cross-sections of the target fuel species and the air is insignificant, e.g., in methane-air mixtures [48]. Here, Mie scattering sand reflected/stray laser scatter are absorbed/blocked by the filter, and therefore the interfering background signal can be remarkably reduced. For this reason, FRS becomes an excellent diagnostic for concentration and gas density even considering its weak output signal intensity. However, even when limiting its application to a zero-dimensional quantitative concentration measurement, FRS still has a much weaker output signal intensity in comparison with that of LIBS; therefore, the measurement uncertainty with FRS is inherently higher. Moreover, sophisticated controls over the laser source, which should be injection-seeded, and the iodine filter are essential in FRS (e.g., the spectral width of the laser pulse and the wavelength range in where the filter blocks transmission should be precisely controlled within an extremely narrow range of several pico-meters). Preventing optical breakdown and window damages while keeping sufficiently high output signal strength is again another critical issue in implementing the FRS.

1.3 Objectives & Outline of the Dissertation

To the best of the author's knowledge, there has not been a single study reporting successful LIBS measurements of equivalence ratio in flammable mixtures (reactants) without ignition using ns-pulses. As will be discussed in this work, flammable mixtures were always ignited with the ns-pulses (6-ns pulse-width from a standard, commercially available Q-switched laser) when the pulse energy is above the breakdown threshold, which is the minimum pulse energy capable of generating plasmas. In other words, this is the first study wherein cold flammable reactants were characterized using LIBS with an ns-laser source, which is enabled by a simple laser pulse modulation setup.

Achieving (1) short enough pulse width not to ignite flammable mixtures and (2) high enough pulse energy to cause gas breakdown stably providing sufficiently strong emission intensity is the primary goal of the pulse modulation technique developed in this study.

In Chapter 2, the gas breakdown phenomenon and inverse-Bremsstrahlung photon absorption process are carefully described with the aid of a mathematical expression that bases the pulse-width modulation. Following the remark on the microscopic aspects of the breakdown plasmas, experimental investigation of the laser energy partitioning and time-dependent characteristics is presented to interpret the breakdown process. The energy fractions resulting from the time-dependent laser photon absorption processes, i.e., MPI earlier and IB later, are discussed. The influencing parameters that determine time-dependency (photon absorption delay, PAD) were theoretically modeled and validated with experimental data sets.

In Chapter 3, the plasma emission resulting from controlled pulse breakdown is captured and analyzed. Time-dependent plasma emission behavior is characterized using fast-gated direct imaging and schlieren photography. The spectral emission profile of the self-emission is recorded from the ultra-violet to near infra-red wavelength range. The experiment confirms that the visible light from the plasma

emission can be useful for concentration measurement. From the spectrum data set, plasma temperature is estimated based on the 2-line Boltzmann approach and line-to-continuum ratio.

In Chapters 4 & 5, the novel method for adjusting the pulse-width of the ns-laser pulse is employed for non-intrusive LIBS measurements in a flammable mixture. The pulse width was controllable to induce sufficiently strong plasma emission but without ignition in flammable reactant mixtures. Additionally, the new LIBS diagnostic offers higher SNR with an improved spatial resolution (and good temporal resolution). The capability of "ignition-free" LIBS is examined and demonstrated in a highly flammable gas flow.

Chapter 2 Laser pulse-width modulation

2.1 Theory of inverse-Bremsstrahlung (IB) photon absorption

Gas breakdown is a thermo-physical process of molecular bond-dissociation and ionization in neutral gas that accompanies formations of high temperature (5,000 - 100,000 K) and pressure (1 – 200 bar) plasmas. In particular, focused laser pulses can induce gas breakdown when the power density at the focus exceeds a breakdown threshold (e.g., bonding energy and ionization potential). The threshold is dependent on the condition of the material (e.g., phase, composition, and density) at the focal point, the focal length of the focusing lens, and the characteristics of the laser pulse (e.g., pulse energy, directionality, and temporal/spatial beam profile). Optical breakdown in neutral gas, which is the primary focus of this study, is due to the rapid electron production via photon-molecule, photon-electron, and electron-molecule interactions, which consequently results in the high electron number density (n_e) above a critical value (n_c).

The early photon energy absorption process leading to gas breakdown can be described as an electron accumulation process that continues until the n_e at the focus reaches a critical value ($n_{e,f}$) [33]. Growth of n_e can be described by a differential equation involving several gain and loss mechanisms through attachment, recombination, and diffusion. The growth of n_e at the focus can conveniently be expressed as

$$\frac{dn_e}{dt} = W_m I^m N + (\nu_i - \nu_{irr}) n_e \tag{2.1}$$

where W_m, I, m, N, v_i, and v_{irr} are the respective multi-photon ionization rate coefficient for m-photon interactions, the laser radiation intensity in W/cm^2, the integer part of $\epsilon_I/h\nu$+1 (ϵ_I, h, and ν are ionization potential, Planck constant, and photon frequency, respectively), the neutral species number density, the collisional ionization rate, and the electron loss rate through attachment, recombination, and diffusion. Before the breakdown, during the early period of the plasma absorption delay, initiatory seed electrons will primarily be produced via the multi-photon ionization (MPI) process at the rate of $W_m I^m N$, which ionizes neutral species requiring multiple photons ($\geq$ m). In this process, more than a single photon is required to overcome the ionization potential of the target at the focus. These electrons can rapidly absorb laser photon energy in the inverse-Bremsstrahlung (IB) process. Then, these high-energy electrons, through collisions with molecules, can produce additional electrons much faster than in the MPI process at the rate v_i. At the onset time when ne reaches $n_{e,f}$, the IB process dominates to readily increase the photon energy absorption rate at the focus (IBA: IB-dominant rapid absorption), which is coincident with the breakdown seen as the abrupt rise of n_e.

Based on the collisional breakdown theory provided in previous works, the breakdown threshold ($I_{bd,cc}$), depending on wavelength, can be expressed as below [49].

$$I_{bd,cc} = 1.44 \times 10^6 (\mathrm{P}^2 + 2.2 \times 10^5 \lambda^{-2}) \tag{2.2a}$$

where $I_{bd,cc}$ is the threshold irradiance in W/cm^2, λ is the laser wavelength in microns, P is the pressure in atm, and t_p is the laser pulse width in seconds (s). In addition, the effective electric field (E_{eff}) related to the momentum transfer during cascade ionization in the plasma would become [50],

$$E_{eff} = E\left(1 + \frac{\omega^2}{\nu_m{}^2}\right)^{-1/2} \tag{2.2b}$$

where E, ω, and ν_m represent electric field amplitude in V/cm, the laser frequency, and electron collision frequency, respectively. Equation 2.2b reveals that sufficient momentum transfer rate is essential in electron excitation that is exposed to the laser's electromagnetic (EM) field, which depends on the amplitude of the EM wave, frequency of the laser light, and the collision frequency that is dependent on the target condition (e.g., temperature). Thus, based on the scaling law in Eqn. 2.2a, the longer-wavelength laser sources would be able to activate the IB process at lower pulse energy for the same focal size.

2.2 Photon absorption delay

When the incident laser pulse energy is low, weak photon-matter interactions, such as Rayleigh and/or Mie scattering, can be expected to occur at the laser focus. On the other hand, it is noteworthy a large fraction of the energy (> 50 - 90 %) can be primarily absorbed and scattered, and the remaining energy will be transmitted particularly with the laser irradiance (W/cm^2) exceeding the breakdown threshold. This is primarily due to the dielectric breakdown and formation of the plasma at the focus. The optical energy supplied by the laser is re-distributed during the breakdown process since there exists a time delay (usually in ns-order) for significant photon energy absorption and scattering to occur after the arrival of the laser photons. The initial photon energy absorption process ($n_e < n_c$) is quite slow and different from that the processes involving after dielectric breakdown ($n_e > n_c$), which requires preceding photon absorption processes to provide initiatory seed electrons. Those seed electrons in turn accelerate and amplify photon absorption and electron generation processes in the IB process.

In general, laser beam characteristics [51], optics [52], gas conditions at the focus [23, 24, 53] all affect the temporally evolving photon absorption characteristics and presumably the time delay for triggering the IBA (photon absorption delay, t_{PAD}). A given laser and optics setup, laser radiation intensity (I) and neutral molecule number density at the focus (N) will determine the t_{PAD}. In this respect, influences of I and N on the temporal plasma breakdown characteristics are investigated, ultimately for controlling the t_{PAD} which is the shutter 'closing time' to chop the ns laser pulse passing through the focal point.

Prior to proceeding to the discussion of photon absorption delay (PAD), this chapter is dedicated to providing novel insight into the plasma absorption related to t_{PAD}. By fully analyzing the optical energy partitioning during the plasma breakdown, the fundamental physics of PAD is given. A detailed description of the measurement setup will be additionally provided in section 4.2.1.

An optical setup shown in Fig. 2.1 is used for inducing gas breakdown to characterize laser pulse energy re-distribution (or energy partitioning) during the plasma breakdown. A Q-switched Nd:YAG laser (10Hz, 532/1064 nm, not injection-seeded) shown in Fig. 2.2 is used for generating plasma. The maximum energy per pulse of the 532 nm beam is 400 mJ. The pulse-profile is measured using an ns-traceable photodiode, and the pulse-width (Full-width half maximum, FWHM) is estimated at 6 ns (Fig. 2.3). The laser beam is focused using an f = 75 mm plano-convex lens and the transmitted beam is collimated using the lens with the same focal length. In Fig. 2.1, the central yellow circle indicates the high-temperature plasma region. The details of laser-plasma temperature, typically greater than 10,000 K, will be further discussed in Chapter 3.

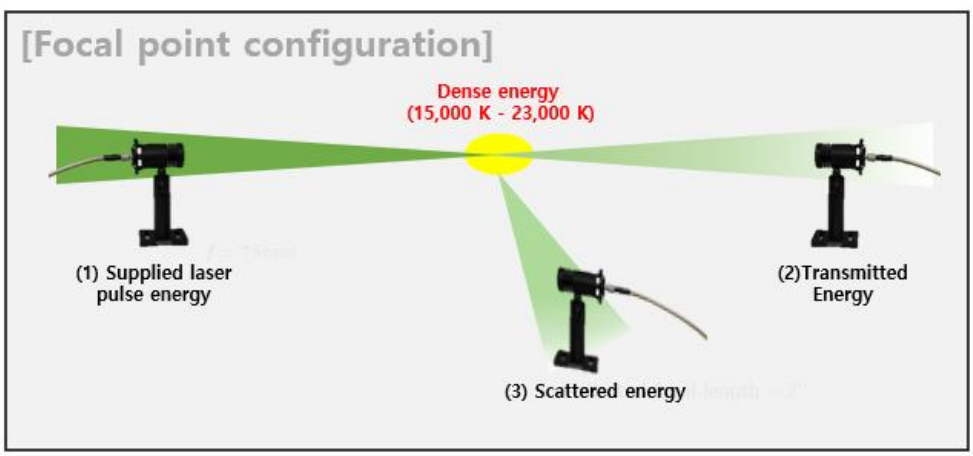

Figure 2.1 Schematic of laser beam flow and laser-induced plasma.

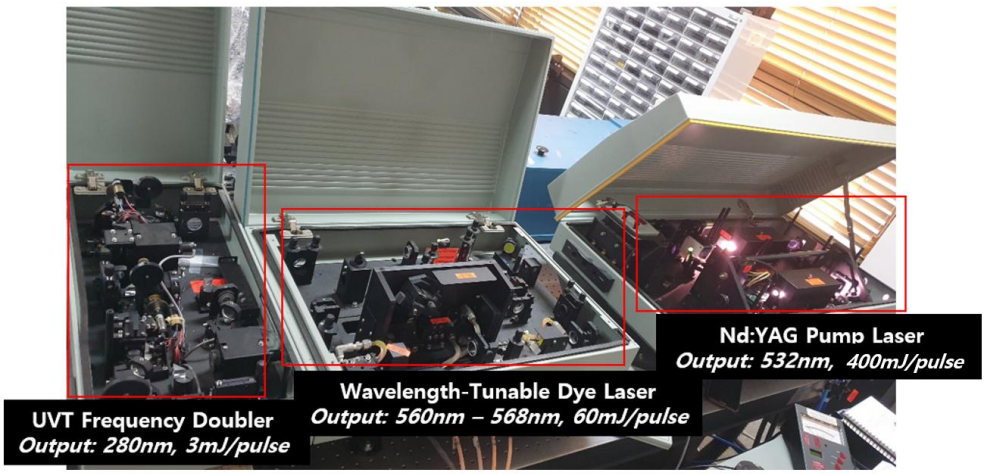

Figure 2.2 A photograph of pulsed Nd:YAG laser system.

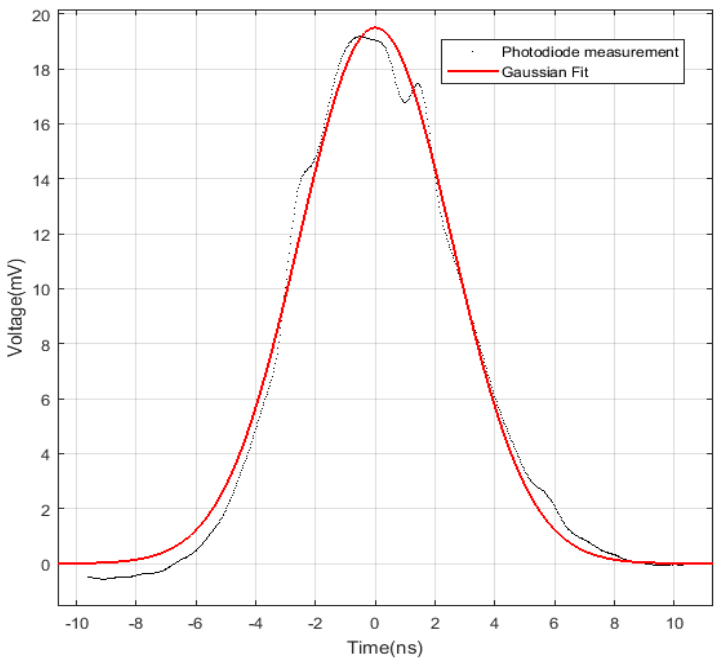

Figure 2.3 Time-averaged temporal profile of the 2nd harmonic (532 nm) Nd:YAG laser pulse.

Figure 2.4 illustrates the distribution of the laser energy around the laser-induced plasma. The supplied laser pulse energy is either transmitted, scattered, and absorbed by the plasma ($E_{laser} = E_{absorption} + E_{scattering} + E_{transmission}$). The calibration process of the photo-detector is conducted at 532 nm wavelength, providing a linear correlation of voltage vs. pulse energy (Fig. 2.5). The pulse-energy measurement eliminates the influence of the spatial pulse intensity distribution of the laser beam by using integrating spheres. The voltage is measured using an oscilloscope and correlated to the pulse energy obtained from a thermopile laser power meter. A detailed description of the plasma energy measurement is presented in Section 4.2.1. Figure 2.6 shows the quantitative measurement result of the laser energy partitioning as a function of E_{pulse}. The threshold pulse energy (E_{bd}) for air breakdown at ambient condition is approximately 8 mJ. The breakdown threshold energy is referenced to the fully-stable breakdown (100%). Below this level ($E < E_{bd}$, the breakdown becomes unstable (frequent misfiring or no breakdown).

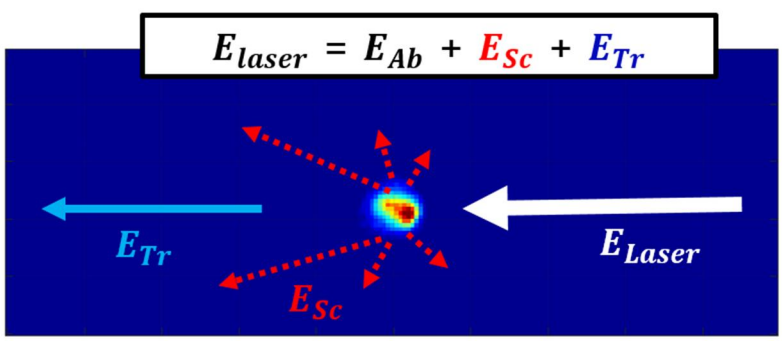

Figure 2.4 Schematic diagram of plasma energy partitioning.

In Fig. 2.6, the scattering fraction gradually increases with E_{pulse} from 16 to 20%, and the fraction of absorption that is just a few % at E_{bd} rises steeply with E_{pulse} (<50 mJ) and approaches 75% asymptotically. The scattering, caused by the breakdown and abrupt change of refractive index [54], would occur after t_{PAD} because a large number of high-energy electrons are needed for the generation of

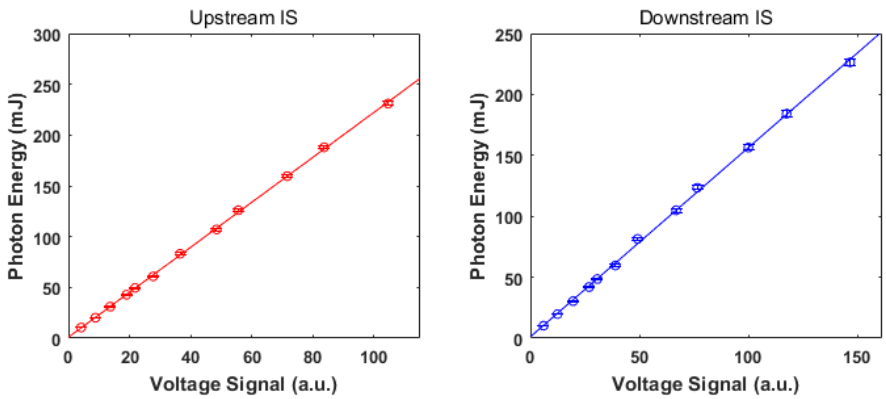

Figure 2.5 Photodiode calibration results at 532 nm wavelength.

plasma and the rapid gas heating that distorts the refractive index field. On the other hand, the transmitted energy that exceeds 80% of E_{pulse} near E_{bd} monotonically decreases with increasing E_{pulse} below 5% at 270 mJ, while the transmitted pulse energy stays nearly unchanged at approximately 12 mJ when E_{pulse} is above 20 mJ. The refractive index field distortion after the IB-induced gas heating would cause significant scattering [54]. As shown in Fig. 2.7, the angular scattering intensity field in the frontal direction (right-to-left in Fig. 2.7) is perfectly fitted to Gaussian distribution. Presumably, this implies that the plasma act as a virtual lens for the incident laser beam. It is also noteworthy that the fractional scattering increases with the input pulse energy (Fig. 2.6). The scattering phenomenon, however, is not directly affecting the transmitted beam because the transmitted beam passes through the focal point before the beam is scattered. Therefore, the detailed mechanism of the beam scattering is outside of the focus in this work. Nevertheless, it is conjectured that the possible causes of the increased scattering with the increment of pulse energy would be (1) earlier plasma formation (that is, inverse-Bremsstrahlung absorption) leading to earlier refractive index field distortion, and (2) faster and greater expansion of the plasma, forming a larger plasma surface area that scatters more laser photons.

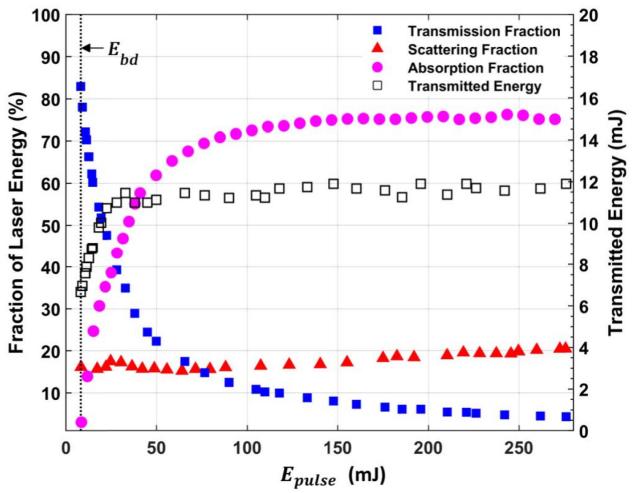

Figure 2.6 Absorbed, scattered, and transmitted fraction of incident laser pulse energy.

*Reprinted with permission from [1] ©**The Optical Society.***

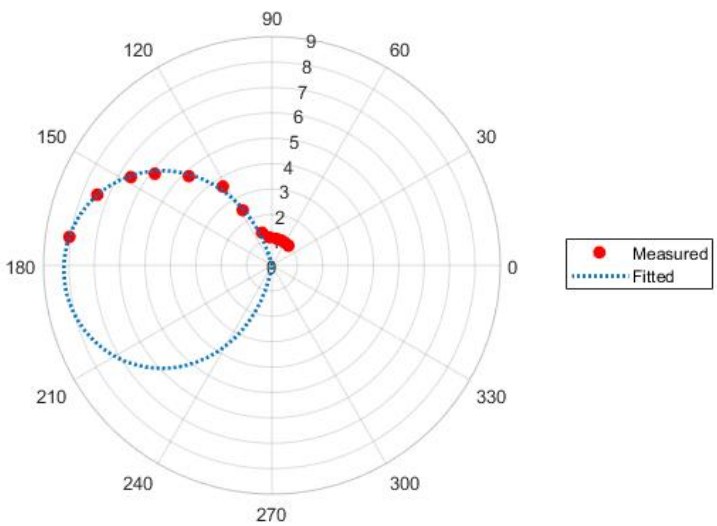

Figure 2.7 Angular scattering intensity distribution of laser light refracted by plasma.

As will be discussed in the following section, the rapid decrease of the laser transmission in Fig. 2.6 is attributed to the steep absorption rise. This fast photon absorption is due to the IBA requiring a sufficient number of electrons. Plasma excitation cross-section, or probability, directly depends on the number density of laser photons and molecules interacting within the focal volume: the laser photon number density in this case is proportional to the laser pulse energy. Higher excitation probability means faster excitation. Therefore, this implies that the time required for plasma excitation inducing strong radiation depends on the gas density and the laser pulse energy.

2.3 Experimental setup

A different optical setup is used for focusing laser pulses in a pressure cell (0.125 bar – 10 bar) to investigate the (1) pulse energy and (2) density dependences of the photon absorption behavior in the plasma. In Fig. 2.8, two plano-convex lenses, both having f = 75 mm, are placed in the configuration so that the transmitted beam is collimated. The laser pulse energy (E_{pulse}) is varied from 8 to 270 mJ rotating a half-wave plate before a polarizing beam splitter while the laser output stays unchanged at its maximum to keep a consistent beam profile [55]. Thermal energy/power meters (Ophir) and photodiodes (ThorLabs SM05PD2A, rise/fall time = 1ns) were used to measure laser beam energy. The downstream-photodiode (D-PD in Fig. 2.8) has a shorter rise/fall time less than 30ps (Electro-Optics Technology, EOT-4000F). Real-time temporal beam profiles were recorded using 1-GHz (Keysight Technology, MSO-X 3104A) and 8-GHz (Keysight Technology, DSO90804A) bandwidth oscilloscopes. The shortest measurable temporal span of an optical signal is confirmed to be <100 ps with the current experimental setup. Photographs of the optical pressure cell (OPC) and the visualized laser beam path in OPC are presented in Fig. 2.9 and Fig. 2.10, respectively.

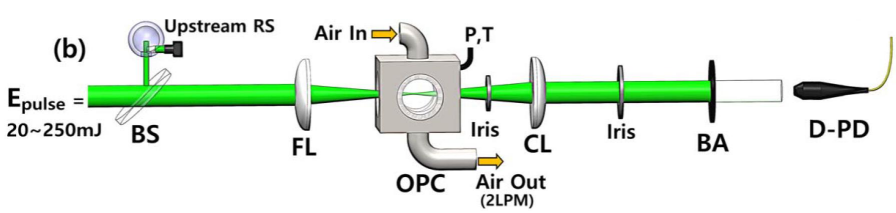

Figure 2.8 Schematic of the experimental setup for pulse-width control.

BA, beam attenuator; BS, beam splitter; BD, beam dump; CL, collimating lens; D-PD, downstream-photodiode; FL, focusing lens; OPC, optical pressure cell; RS, reflecting sphere.

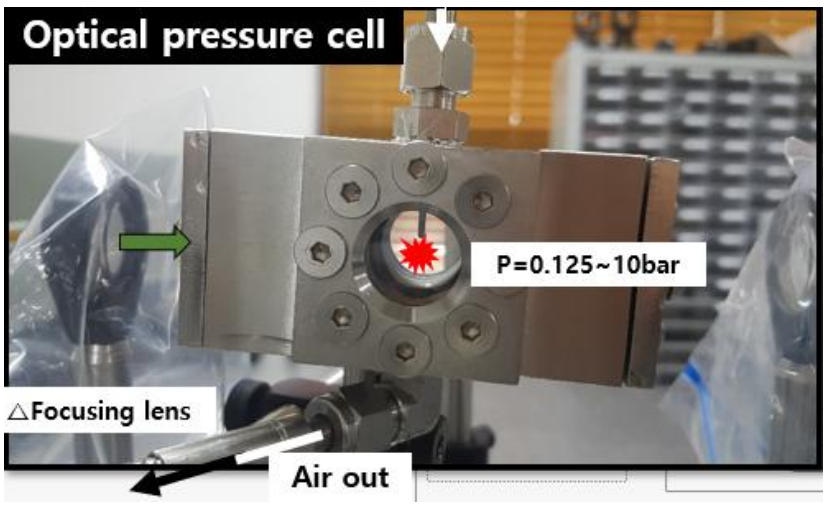

Figure 2.9 A photograph of optical pressure cell for pulse-width modulation.

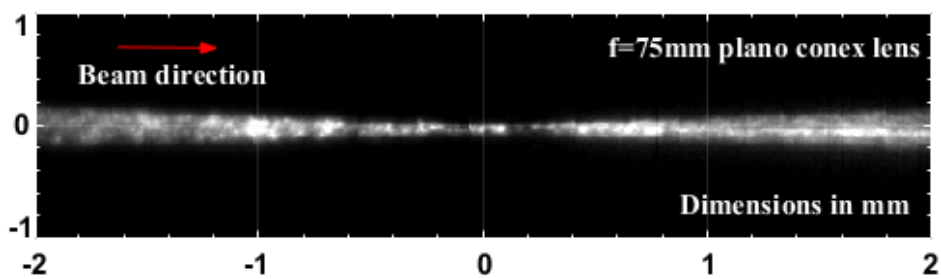

Figure 2.10 A visualized image of a focused laser beam (4 mm x 2 mm ROI).

2.4 Pulse-width modulation

2.4.1 Experimental result

The influence of the gas density on the excitation time is examined by tracing the temporal laser beam intensity variation downstream of the plasma (i.e., a transmitted laser beam). A sudden drop of the transmitted beam intensity is observed which corresponds to the sudden rise of electron number density and plasma excitation to induce strong photon absorption.

Figure 2.11 shows the temporal intensity profiles of the transmitted beam normalized by the peak laser intensity; each waveform is averaged over 150 individual laser shots at E_{pulse} = 47 mJ, 112 mJ, and 250 mJ, respectively. It is clear that the air at the focus is transparent to the laser beam when $t < t_{PAD}$; however, later, the transmission drops and the scattering rises simultaneously, which is due to the IBA. Interestingly, the t_{PAD} gets shorter as the E_{pulse} increases. Therefore, the fraction of transmitted energy decreases, because the laser radiation intensity reaches the IBA earlier with higher E_{pulse}. This is evident considering that the temporal profile of the laser radiation intensity normalized by the peak (Fig. 2.11, No breakdown) remains unchanged while the E_{pulse} is varied using the optical setup employed in this study. For this reason, the t_{PAD}. asymptotically approaches a value above zero as the E_{pulse} increases (Fig. 2.12), and the transmitted energy is nearly constant at ~12 mJ when $E_{pulse} > 20$ mJ at ambient conditions.

Thus, the rapid decrease of the laser transmission shown in Fig. 2.6 is attributed to the steep absorption rise. Attaining $n_{e,f}$ at the focus initially from neutral gas requires minimum radiation intensity (IBA) and electron accumulation with continuous photon energy supply, which takes time (t_{PAD}).

The red dotted curve in Fig. 2.11 illustrates the forward scattering intensity profile captured from 45° incident direction at E_{pulse} = 47 mJ, and the black dotted curve (No breakdown) is the incident temporal beam profile. The neutral species

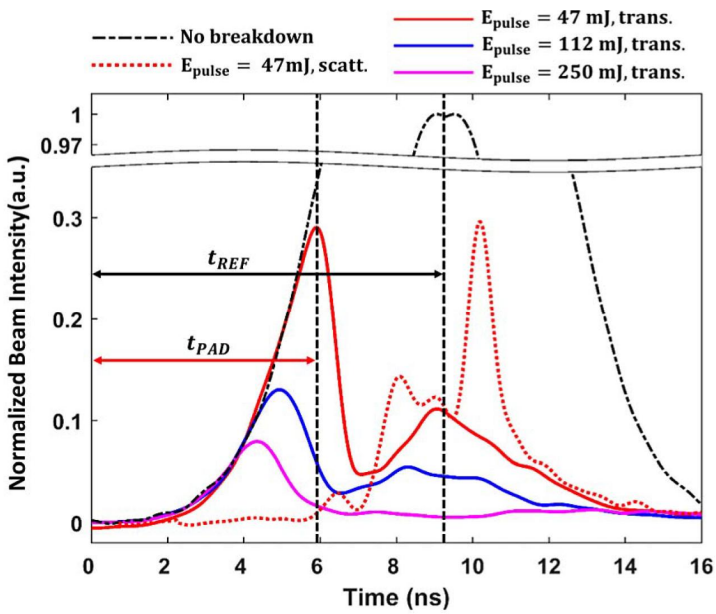

Figure 2.11 Transmitted laser beam intensity profile at E_{pulse} = 47 mJ (red solid), 112 mJ (blue solid), and 250 mJ (magenta solid).

Reprinted with permission from [1] ©The Optical Society.

number density (N) also directly impacts the early electron production process of MPI as expressed in Eqn. 2.1. Figure 2.12 shows t_{PAD} versus E_{pulse} at P_{cell} of 0.125 bar and 1.07 bar; the error bars (standard deviation) are relatively large because the laser used in this study is not injection-seeded. Each data point represents an average over 150 measurements. The t_{PAD} at P_{cell} = 0.125 bar is 1 – 3 ns longer than that at 1.07 bar; thus, the 'shutter closing' time or the occurrence of IBA is delayed by reducing the P_{cell}. The photon absorption delay (t_{PAD}) determining the pulse width of the transmitted beam is measured with varied pressure (P_{cell} = 0.125 – 10 bar) and pulse energy (20 – 250 mJ), and it is correlated with a nondimensional parameter, $(N/N_0) \cdot (E/E_0)^2$, as shown in Fig. 2.14, where N/N_0 and E/E_0 are normalized number density in the pressure cell (reference condition = 1 atm, 300 K) and E_{pulse} (mJ)/65 mJ, respectively. In general, the t_{PAD} decreases as the density (proportional to P_{cell} at a fixed temperature) and E_{pulse} increases, and all data points collapse onto a single

line ($R^2 = 0.974$) (Fig. 2.14). The exponents of the normalized density (N/N_0) and pulse energy (E/E_0), 1 and 2, respectively, are determined to attain the best-fit line of the maximum R^2. This experimental observation is consistent with a simplified theoretical analogy.

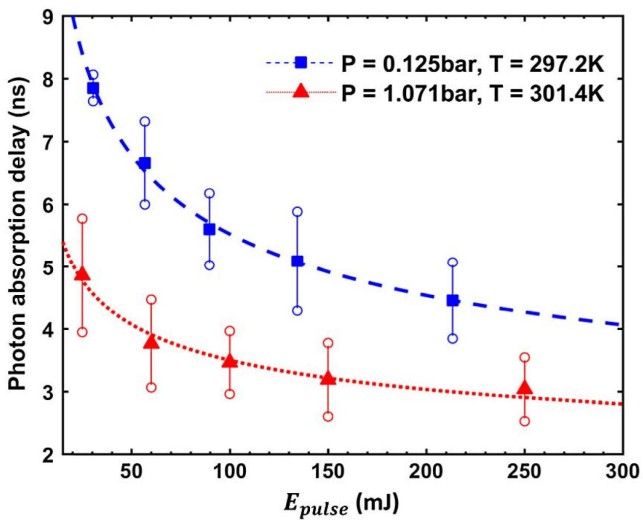

Figure 2.12 Onset of breakdown (PAD) at different pressure.

Reprinted with permission from [1] ©The Optical Society.

Equation 2.1 provides the electron production rate, and n_e is its time integration. The time-dependent laser pulse intensity, $I(t)$, is measured using a fast photodiode (30-ps rise/fall time). In order to trigger the IBA, which abruptly stops the laser beam transmission, the electron number density should reach a constant, $n_{e,f}$. For simplicity in the analogy, the laser radiation for the limited time duration of t_{PAD} is regarded as a square pulse of constant intensity, $\bar{I}_{sq} = \int_0^{t_{PAD}} I(t)\,dt/t_{PAD}$, as shown in the blue square pulse in Fig. 2.13. Considering that normalized temporal pulse profile (e.g., fitted curve in Fig. 2.3) is not changing with E_{pulse}, the $\bar{I}_{sq}$ (average radiation intensity during t_{PAD} from the beginning of the laser radiation) is proportional to E_{pulse} for a given t_{PAD}.

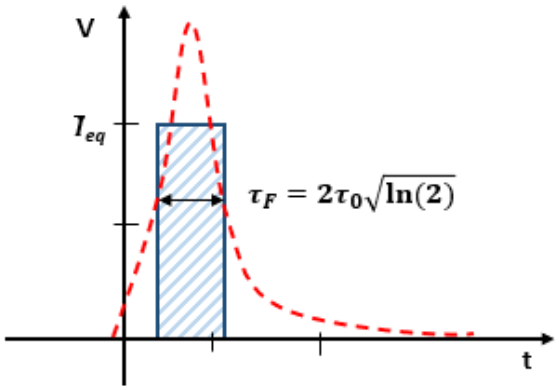

Figure 2.13 Diagram of the square pulse (blue-solid line) equivalent to the transmitted pulse (red-dotted line).

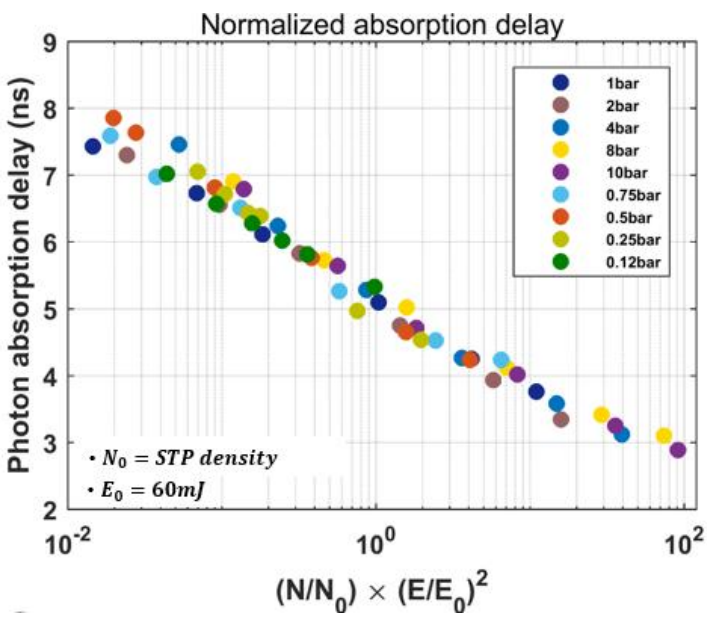

Figure 2.14 Photon absorption delay (t_{PAD}) versus $(N/N_0)\cdot(E/E_0)^2$.

N/N_0 = normalized number density and $E = E_{pulse}$ ($E_0 = 65mJ$)

*Reprinted with permission from [1] ©**The Optical Society.***

It is assumed that the initial electron number density ($n_{e,i}$) is immediately produced through MPI, and the collisional electron production ($v_{i,eff} = v_i - v_{irr}$) dominates for the rest of the period. Thus, based on Eqn. 2.1

$$\ln\left(\frac{n_{e,f}}{n_{e,i}}\right) = \int_{t\sim 0}^{t_{PAD}} v_{i,eff}(I, \mathrm{N})dt = constant \tag{2.3}$$

which is a typical way of modeling the breakdown phenomena [56].

It was previously shown that the ionization frequency($v_{i,eff}$) is proportional to N and I^k, where k is an exponent of radiation intensity that needs to be determined numerically or empirically [57, 58]. Presumably, the time period t_{PAD} is too short for gas heating-induced expansion; thus, the density (N) and I $(= \bar{I}_{sq})$ are constant for the duration, and consequently

$$v_{i,eff}(\bar{I}_{sq}, \mathrm{N}) \cdot \mathrm{t_{PAD}} = constant \tag{2.4}$$

Therefore,

$$\mathrm{t}_{PAD} \propto \frac{1}{\mathrm{N}}\left(\frac{1}{\bar{I}_{\mathrm{sq}}}\right)^k \propto \frac{1}{\mathrm{N/N_0}}\left(\frac{1}{\mathrm{E/E_0}}\right)^k \tag{2.5}$$

The exponent (k) for N_2, the dominant species in air, was numerically calculated [57, 58]; k is always > 1, and the best fit of the experimental data gives k ≈ 2. This correlation depends on the gas composition in the cell, and thus the 'shutter' performance would also be dependent on the constituents having different ionization potentials [23] and cross-sections. It is noteworthy that the initial electron number density (n_i) does not dominates for the rest of the period, which involved in the integration. The n_i is rather a critical pre-condition defining the initiation of a significant IB process. For example, the number of cascade-ionization species was

defined by n_i, which is the exponent of the electron number density ratio, i.e., the electron number density over the n_i. Then minimum n_i for breakdown or the significant IB process can be determined for a breakdown model.

The simplified breakdown model of Eqn. 2.3 is from the references [58], and reflects a typical and generic approach that has been used to model the gas breakdown phenomenon considering the collision-dominated plasma growth. In the current experiment, the inverse-Bremsstrahlung process is found to be the major photon-energy absorption mechanism with gas pressure 0.1 to 10 bar [59]. Therefore, the electron avalanche, or cascade electron growth, is expected to be primarily caused by the IB process after the production of initial seed electrons by multiphoton ionization (MPI).

The cascade-ionization-dominated gas breakdown condition can be derived by integrating Eqn. 2.1 over time assuming that the breakdown occurs when the electron number density or the number of cascade ionization exceeds a certain threshold. In the simplified model, the time-integration is until the end of photon-absorption delay (t_{PAD}, Fig. 2.11) assuming that the critical electron number density is reached at the time instance. Here, the initial seed electron number density is much smaller than the density at the end of PAD, therefore, the time required for the seed electron production is assumed to be negligible. Again, the assumptions used in the breakdown model are reasonable according to the numerical predictions presented in [58].

2.4.2 Performance

In the range of P_{cell} (up to 10 bar in Fig. 2.15), the shortest achievable pulse width is approximately 600 ps, which can be further shortened while increasing the output pulse energy by curtailing the leading edge of the laser pulse prior to being focused in the pressure cell, e.g., using a saturable absorber (SA). The red curve in Fig. 2.15 shows the temporal intensity profile of a 3-mJ transmitted laser pulse normalized by the peak intensity for comparison with the incident laser profile (blue). This transmitted beam (at P_{cell} = 10 bar) has approximately 600 ps FWHM (full width at half maximum).

Figure 2.16 shows the trends of pulse width and pulse energy of the transmitted beam vs. P_{cell} at E_{pulse} = 62 mJ/pulse. Both the output pulse width and energy are decreased by increasing P_{cell}, mainly attributed to the dependency of PAD on the number density (N, See Eqn. 2.5). In short, the output pulse width is controllable by tuning the onset of the gas breakdown.

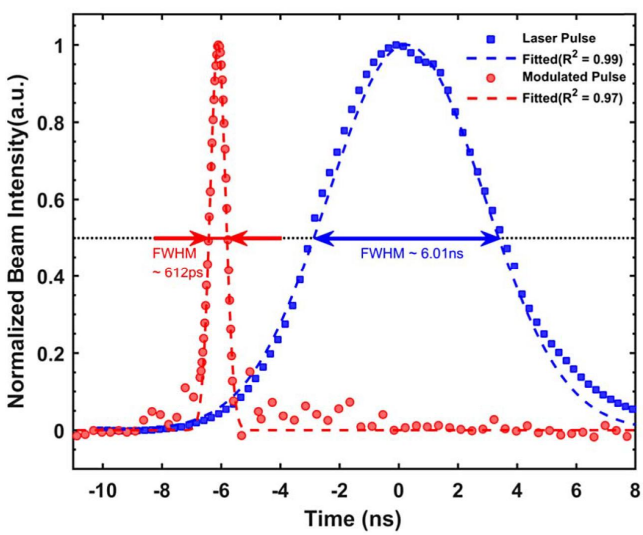

Figure 2.15 Laser pulse profiles normalized by the peak intensity.

Reprinted with permission from [1] ©The Optical Society.

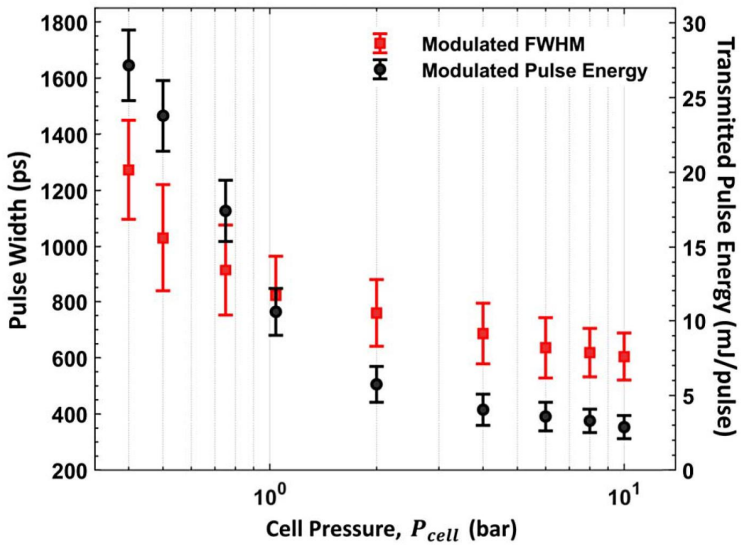

Figure 2.16 Pulse width and pulse energy of the transmitted beam vs. cell pressure.

Reprinted with permission from [1] ©The Optical Society.

Stimulated Brillouin scattering (SBS) can also be used to shorten the ns pulse width. This method has better controllability and requires a simpler modulator setup compared to other pulse width modulation techniques based on Pockels effect and Stimulated Brillouin Scattering (SBS) phenomenon. Pulse-energy conversion efficiency of the SBS pulse-shortening (50 - 75 % [60]) is much higher than the proposed method (5 - 12 % [1]) since the SBS compresses the pulse while the proposed method merely cuts off the trailing part via the abrupt IB photon absorption process. For the same reason, however, the chopped pulses are cleaner and more stable in general than the SBS-compressed pulses. The pulse stability in temporal intensity profile and energy of the chopped pulses can even be further improved with injection-seeding and/or installation of a non-linear saturable absorber (before the high-pressure cell) as shown in [1]. Recall that the pulse width fluctuation is primarily from the pulse-to-pulse variation of the unseeded-pumping source.

Another critical benefit of the proposed method is convenient pulse width control by adjusting the cell pressure, whereas, the length of the compression tube (water tubes of a few meters (typically 1 – 3 m) in length) should be varied or the tube should be replaced to alter the pulse width of the compressed pulses. Moreover, the operation range of the SBS pulse compression device is strictly limited by various non-linear optical processes such as the optical breakdown, diffuse Brillouin scattering, and Raman scattering, as reported in [61, 62].

In Fig. 2.15, a frequency-doubled Nd:YAG laser (532nm) was used simply because it is a commonly used high-power laser source. Different lasers (e.g., CO_2 laser) can also be used for the proposed pulse-chopping method. Since the longer wavelength is more effective in gas heating through the laser energy absorption from IB, CO_2 lasers could provide better controllability in pulse-width modulation. It has been reported that the breakdown threshold in air is lower with IR-lasers in terms of the irradiance (W/cm^2) at the focus in comparison with typical visible-wavelength lasers (Eqn. 2.2a).

In order to confirm the possible application of longer-wavelength laser sources, additional experiments were conducted, and the experimental result with longer wavelength (1064 nm) pulses is presented in Fig 2.18. The figure clearly shows the effect of the SA. The blue square dots represent the original laser intensity profile at 1064nm (FWHM = 9.8 ns). This laser beam is expanded by a Galilean beam expander (M=0.25X; a combination of 400mm and -100 mm plano-convex lenses) then enters an SA (Cr^{4+}: YAG, Tr = 54 %). The SA can sharply cut the leading edge (Fig. 2.18, SA), utilizing the non-linear photon absorption characteristics of the carefully chosen SA material [63]. With the steeper leading-edge, shorter pulse width: FWHM = 520 ps and higher pulse energy = 8.1 mJ of the transmitted beam (Fig. 2.18, SA + IBA) can be obtained at P_{cell} = 1 atm and E_{pulse} = 65 mJ. In short, using the combination of an SA for cutting the leading edge and a pressure cell chopping the trailing edge, the laser pulse width and temporal pulse profile can be modulated as needed. The pulse area entering the SA, material composition of the SA, number

of SA in use, laser wavelength, E_{pulse}, P_{cell}, and gas composition in the pressure cell can be varied for tuning the pulse profile. In addition, the use of an SA could improve the stability of the output pulse ($\mathrm{FWHM} = 520 \pm 20\mathrm{ps}$), suppressing the intensity fluctuations often observed with unseeded laser pulses.

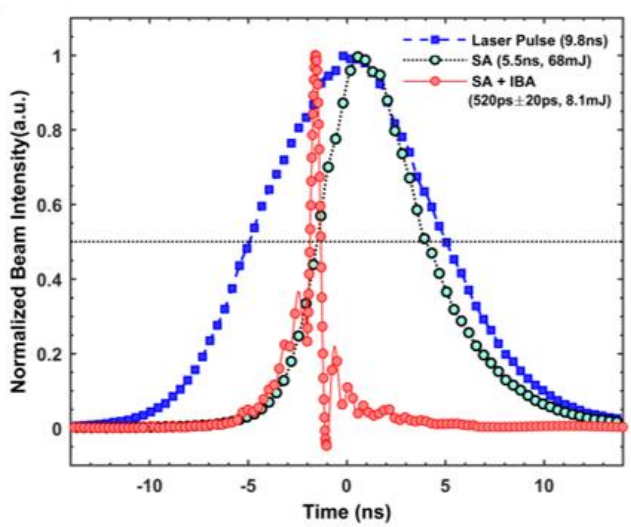

Figure 2.17 Normalized pulse intensity profiles at 1064 nm (FWHM=9.8ns) with (green) and without (blue) a saturable absorber (SA), and transmitted through an SA and a breakdown plasma at P=1atm (red).

*Reprinted with permission from [1] ©**The Optical Society.***

The proposed pulse-width modulation technique and the SBS method are compared and summarized in Table 2.1 [60, 61] (RSD: Relative standard deviation). Since the proposed method simply chops a part of the laser pulse in the time domain via the abrupt IB photon absorption process, the conversion efficiency is lower than that of the pulse compression via SBS; however, the pulse profile is cleaner in general with the proposed chopping method for the same reason.

In fact, the pulse width variation and the pulse energy stability of the proposed technique shown in the table above can be significantly improved. Recall that the

ns-laser source used in this study was unseeded; therefore, the pulse width fluctuation is primarily from the pulse-to-pulse pumping source variation (and it is believed that improved stability will be realized with an injection-seeded laser). In addition, a Saturable absorber (SA) can be used to reduce the pulse rise time, and therefore activate the IB process quicker (i.e., faster shutter closing), which also improved both the conversion efficiency and the pulse width variation.

Table 2.1 Comparison of the pulse control techniques.

Factor	IB chopping	Stimulated Brillion Scattering
Conversion efficiency	5 %	70 %
Pulse width	600 ± 40 ps	600 ± 50 ps
Pulse energy stability	7 % RSD	5 – 10 % RSD

Chapter 3 Light emission from plasma

3.1 Theory of plasma emission

Focused laser pulse of several MW/cm^2 irradiance can dissociate and ionize gas molecules and consequently forms an energetic plasma. The temperature of the plasma exceeds over 100,000 K on the onset of breakdown and relaxes thereafter by equilibrating with the cool surrounding. The excited plasma goes through a rapid energy relaxation process in form of radiation.

In general, atomic and electron emissions, as well as molecular emission, are the typical components of plasma radiation. Even for the same species, the emission characteristics differ tremendously depending on the thermodynamical state of plasma. The type of plasma (e.g., hot or cold) can be classified by electron density and temperature, which can be referred to in Fig. 3.1.

The emission from a high-energy-density plasma primarily consists of ionic & atomic features. It is noteworthy that the molecular emission is relatively difficult to detect due to the intense gas-heating caused by the inverse-Bremsstrahlung photon absorption process while the continuum radiation obscures the weak molecular emissions. On the other hand, the atomic emission arises from transitions between discrete energy levels of excited species, and the continuum radiation is generated in (1) the recombination process of ions and electrons (recombination continuum) and (2) the interactions of free electrons with the ion electrical fields or neutral particle (Bremsstrahlung). The emission coefficient (ε), which is the energy of radiation emitted per unit time, for the lines (ε_l) and continuum (ε_c) can be expressed as in Eqn. 3.1 and Eqn. 3.2, respectively.

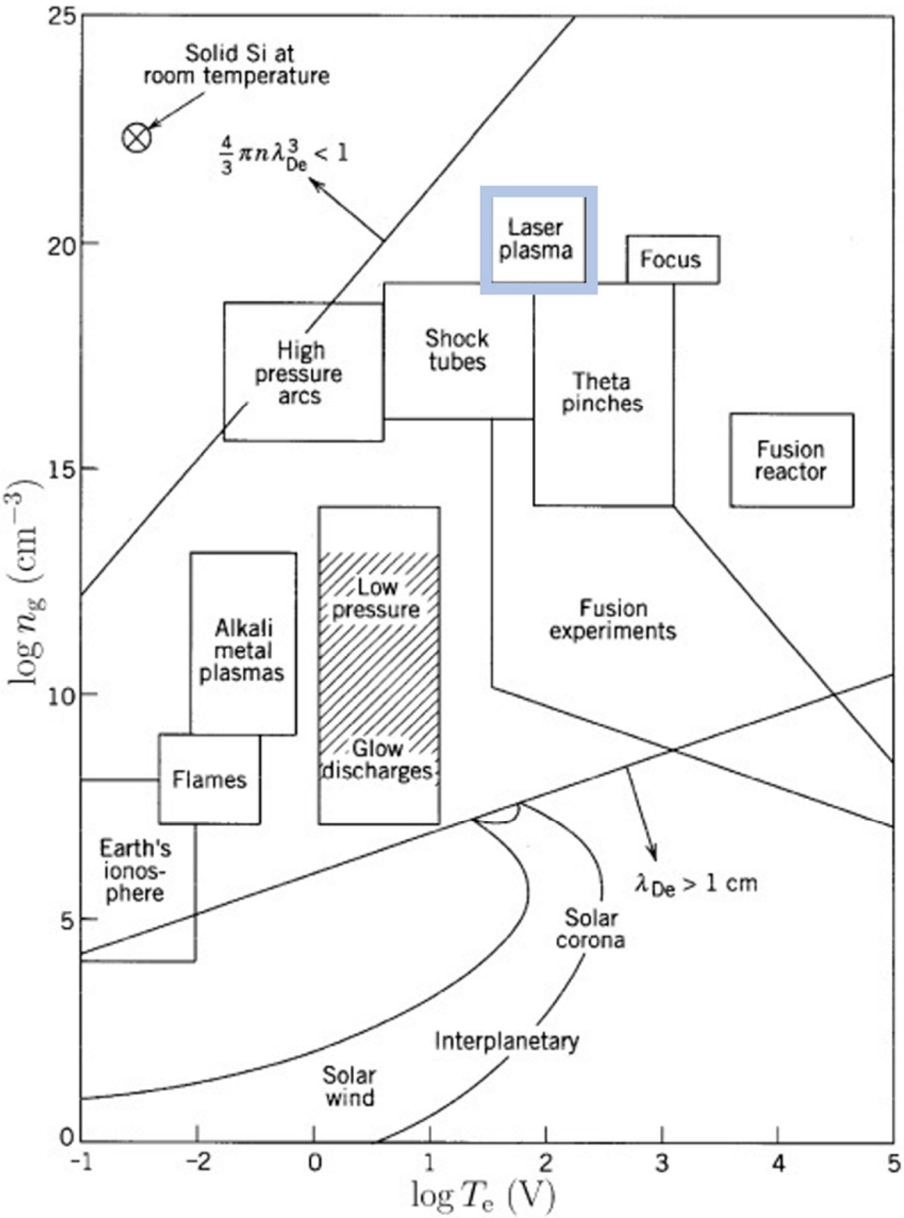

Figure 3.1 Classification of plasma type according to electron number (n_e) and temperature (T_e).

$$\varepsilon_l(v) = \frac{hv}{4\pi} A_{21} \frac{g_2}{2U_i} \frac{h^3}{(2\pi mk)^{\frac{3}{2}}} n_e n_i T_e^{-\frac{3}{2}} \left[\exp\left(\frac{E_i - E_2 - \Delta E_i}{kT_e}\right)\right] \quad (3.1)$$

$$\varepsilon_c(v) = \left(\frac{16\pi e^6}{3c^3(6\pi m^3 k)^{\frac{1}{2}}}\right) \frac{n_e n_i}{T_e^{\frac{1}{2}}} \left[\xi\left(1 - \exp\frac{-hv}{kT_e}\right) + G exp\frac{-hv}{kT_e}\right] \quad (3.2)$$

where A_{21}, c, e, E_2, E_i, ΔE_i, G, g_2, h, k, m, n_e, n_i, T_e, U_i, v, and ξ are the Einstein transition probability of spontaneous emission between levels 2 and 1, speed of light, charge of an electron, energy of atom level 2, ionization potential, lowering of the ionization potential, free-free Gaunt factor, degeneracy of level 2, Planck constant, Boltzmann constant, mass of an electron, electron number density, ion number density, electron temperature, partition function of the ions, frequency, and free-bound continuum correction factor, respectively. The appropriate unit for Eqn. 3.1 is J s^{-1} m^{-3}, and J s^{-1} m^{-3} Hz^{-1} for Eqn. 3.2. As shown in Eqn. 3.1, the emission line strength or the emission coefficient (ε_l) is determined by species-specific parameters, such as the discrete internal energy levels and ionization potential, and the plasma properties, including the temperature and number density of electrons and ions. In contrast, the continuum radiation depends only on the plasma properties (T_e and n_e).

3.2 Visualization

To enhance the understanding of physical plasma behavior, numerous works for visualizing plasma structure with direct imaging or schlieren were attempted [53, 64-66]. The plasma visualization during the laser-plasma interaction and post-breakdown periods are presented in this section. The imaging was conducted from the beginning of the pulse arrival unlike the typical [53] plasma photography.

Figure 3.2 shows that experimental setup capturing plasma self-emission and density disturbance. The continuum Nd:YAG laser introduced in Chapter 2 is used, and a laser pulse energy control unit (LPEC) is installed for controlling laser pulse energy stably at 200 mJ. In addition, an apparatus for the laser pulse width control (LPWC) is installed. The LPWC system includes the LPEC. The laser beam with ns-pulse width is focused using a plano-convex lens having f = 75 mm focal length, while f = 50 mm is used for a beam with ps-pulse-width. Broadband emission from plasma is captured using ICCD (Princeton Instrument, PI-MAX II) camera. The actual imaging wavelength is conditioned by the neutral density (Thorlabs, NE0X) filter, as well as the wavelength selectivity of the photocathode, phosphor, and CCD chip. In the filtered measurements, the self-emission is captured with a 532 nm linear polarizer (PL, Thorlabs). The PL is set at the in-phase angle with the polarized laser light such that the signal intensity is maximized. Density perturbation is detected using the schlieren system with Toepler's geometry. The detailed setup for schlieren photography used in this study is well described in Han et al. [64]. In the schlieren measurement, a low-power HeNe laser (633 nm, 10 mW) is utilized for the illumination source. The beam passes the plasma center (Fig. 3.3) to record the density perturbation induced by the gas breakdown. An off-axis mirror (MR) is used to guide the beam to a ground-glass (GS) imaging screen.

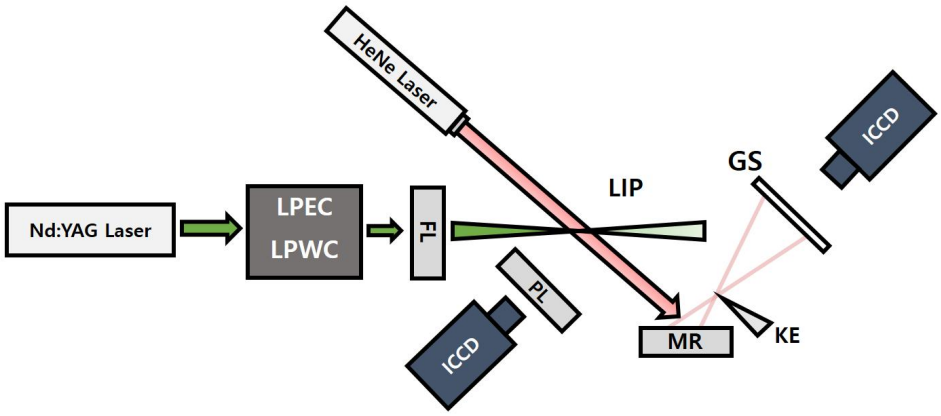

Figure 3.2 Experimental setup capturing plasma emission.

FL, focusing lens; PL, polarizer; GS, ground glass screen; MR, mirror; KE, knife-edge; LIP, laser-induced plasma; LPEC, laser pulse energy controller; LPWC, laser pulse width controller.

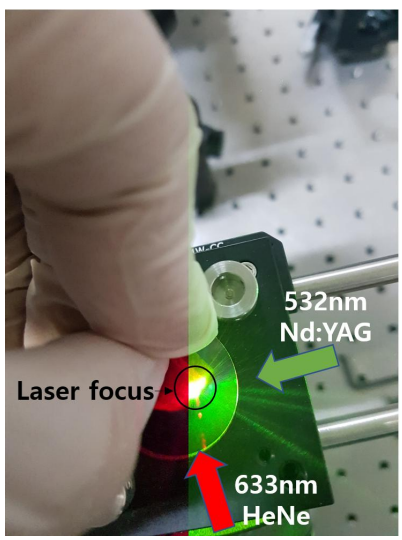

Figure 3.3 Laser alignment of 532 nm Nd:YAG and 633 nm HeNe laser beams.

3.2.1 Laser irradiation period

By adjusting the camera acquisition delay during the laser irradiation period, the temporally-resolved morphological plasma growth is visualized. Figure 3.4 shows the instantaneous plasma images captured using an intensified CCD camera with a magnification lens (Nikkor f = 80mm) and multiple extension tubes.

In Fig. 3.4, the laser arrives at the focus at 0 ns, and the inverse-Bremsstrahlung absorption is effectively visualized from 2 ns to 15 ns after the gas breakdown. Note that the effective absorption period is observed till $t_d = 15$ ns after the initial breakdown, whereas the pulse width (τ_p) measured in full-width at half maximum is 6 ns. The plasma growth is bi-directional in the laser beam direction, indicating the significant absorption at the two dominant cores. During this period, the plasma temperature is elevated up to 100,000 K [67] due to the intense IB heating. After t_d > 17 ns, Bremsstrahlung continuum emission can be observed when the plasma expands and the thermal energy is dissipated.

The propagation speeds of the plasma front were calculated to confirm the plasma growth mechanism, for two different incident laser pulse energy (25.4 mJ and 101.7 mJ). In Fig. 3.4, the instantaneous propagation velocity is estimated in the range of 50~190 km/s. In addition, the ratio of average growth speed is close to 2 for two cases (a) and (b) in Fig 3.4. The range of values corresponds to the prediction of the detonation growth model [68]. In the detonation model, the wave propagation speed is given by Eqn. 3.3 (G = 10 ~ 200 GW/cm^2).

$$\mathrm{D} = \left[2(\gamma^2 - 1)\frac{\mathrm{G}}{\rho_0}\right]^{1/3} \tag{3.3}$$

where γ is the specific heat ratio of the medium, and ρ_0 is the local gas density in kg/m^3. Considering the plasma absorption fraction (presented in Fig. 2.6) for the incident laser pulse energy in Fig. 3.4, the ratio of actual absorption energy (G) was estimated at 7.2. Substituting this value in Eqn. 3.3, the relative speed (D) ratio is

estimated to be 1.92. The result suggests that the plasma generation is detonation-dominated.

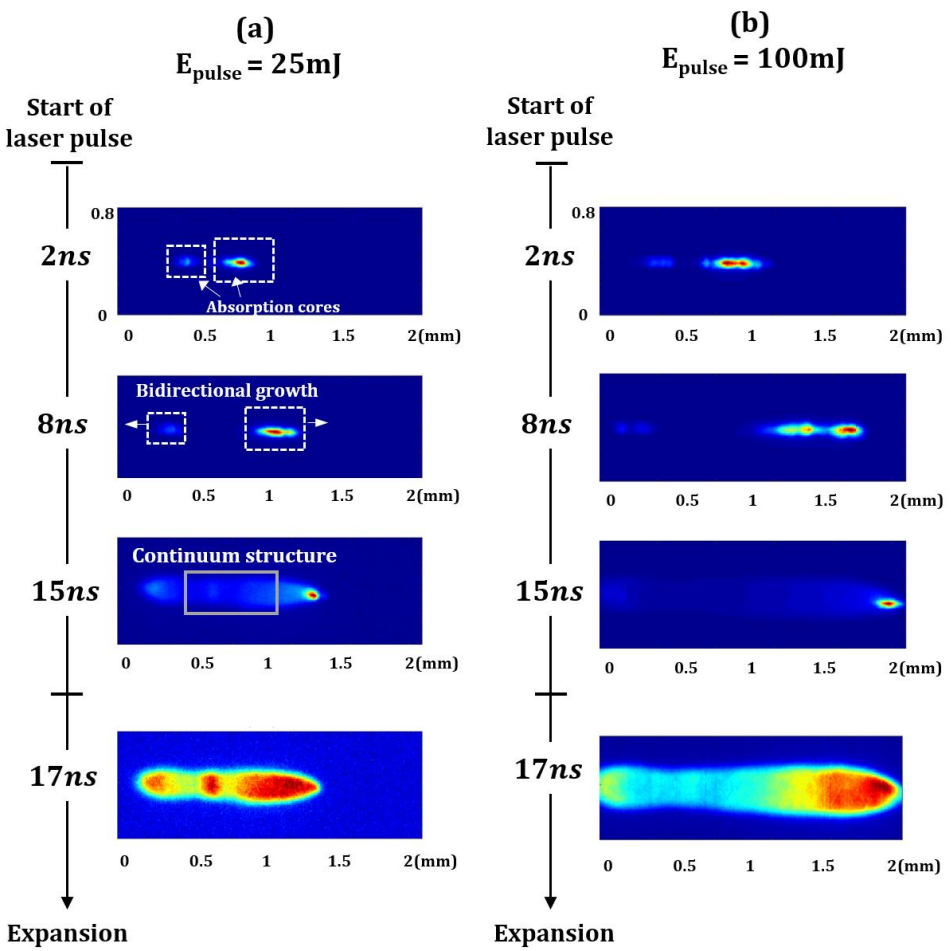

Figure 3.4 Time-dependent plasma growth for two different incident laser pulse energy, (a) E_{pulse} = 25 mJ and (b) E_{pulse} = 100 mJ.

Figure 3.5 show the plasma emission structure at the end of two different laser pulse width, (a) τ_p = 600 ps with E_{pulse} = 3 mJ, and (b) τ_p = 6 ns with E_{pulse} = 120 mJ. From Fig 3.5(a), the initial core size of the ps-plasma is approximately 0.15 mm in diameter. The expansion of the plasma after the end of the pulse duration has been reported in [35], which can be fairly assumed to become roughly 2 times the initial core size. Therefore, the spatial resolution of the ps-plasma for LIBS measurement is estimated to be at most (the factor of 2 is obtained with much stronger laser pulses of 180 mJ/pulse) 300 μm. The diameter of the cylinder-shaped plasma with the ns-LIBS in the figure is roughly 0.5 mm, thus, the spatial resolution of the ns-plasma would be approximately 1mm. The plasma volume is also dependent on gas density. The density dependence will be further provided in section 5.4.

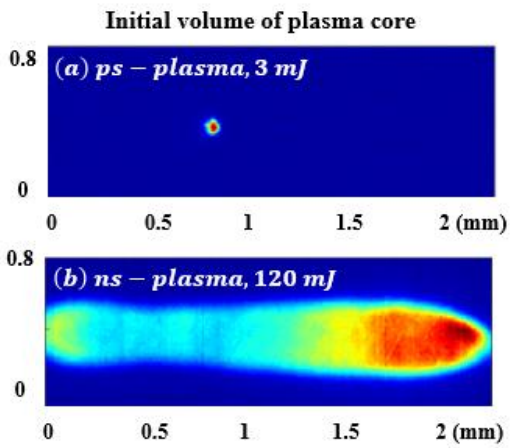

Figure 3.5 Plasma self-emission captured at the end of two laser pulses.

3.2.2 Post-breakdown period

After the laser radiation is terminated, the plasma expands and equilibrate with the cold surrounding. Since the density perturbation is significant during the plasma expansion period, the schlieren photography is effectively applied to capture the post-breakdown morphological behavior of laser-induced plasma. The temporally-resolved schlieren result is presented in Fig. 3.6 for the gate delay (t_d) from 60 ns to 900 ns at a fixed input laser pulse energy E_{pulse} = 60 mJ. The hydrodynamic expansion can be modeled by Sedov-Taylor blast wave theory [68], where the estimated leading-edge pressure of the shock wave is 130 atm at t_d = 60 ns, with the range of the hypersonic expansion speed of 1 ~ 5 km/s.

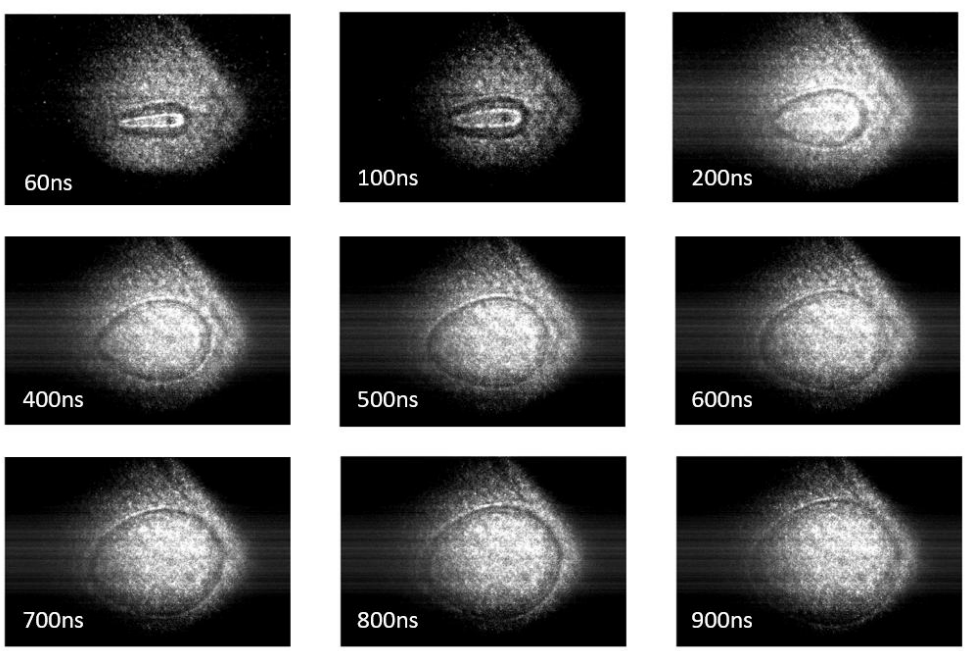

Figure 3.6 Time-dependent growth of plasma shock waves captured using schlieren photography.

3.3 Spectral analysis

The laser-induced plasma radiates spectrally distinguishable self-emission which is informative to the chemical composition of target parent species. This aspect has been gaining great interest from chemical diagnostics, so-called laser-induced breakdown spectroscopy (LIBS).

The usefulness of plasma emission is that it can be utilized to measure (1) plasma parameters and (2) gas property of the breakdown target. This is because plasma emission property is dependent on its physical dynamics and environmental target condition.

3.3.1 Air plasma spectrum

Figure 3.7 shows the typical plasma spectrum in the air from 700 to 850 nm, measured using a USB spectrometer (Ocean Insight, USB 2000). As seen from the figure, the species-specific atomic lines are discernable, which bases the optical concentration measurement using peak intensity ratios, or PIR (e.g., N/O peaks) extracted from the emission spectra. In general, the intensity of a single peak monotonically grows with the corresponding species concentration, and the growth rate can be fitted to a linear correlation that has been reported in previous works [5, 24, 25].

The simple theoretical expression for photon emission intensity of an atomic line can be described below

$$I_{ji} = \mathrm{n}_j A_{ji} h\nu_{ji} \tag{3.4}$$

where I_{ji} is photon emission intensity, n_j is j-state number density, A_{ji} is Einstein coefficient for state j → i transition, h is Plank constant, and ν_{ji} is the

frequency of the photon emitted. In particular, the upper-state number density n_j can be theoretically modeled from the quantum mechanical distribution under local thermodynamic equilibrium (LTE) assumption, i.e.

$$\mathrm{n}_j = \frac{\mathrm{n}_0 g_j e^{-\frac{\mathrm{E}_k}{kT}}}{Z(T)} \tag{3.5}$$

Thus, the line intensity expression is simply proportional to the atomic concentration (n_0) and also upper state concentration (n_j) at a certain plasma temperature T.

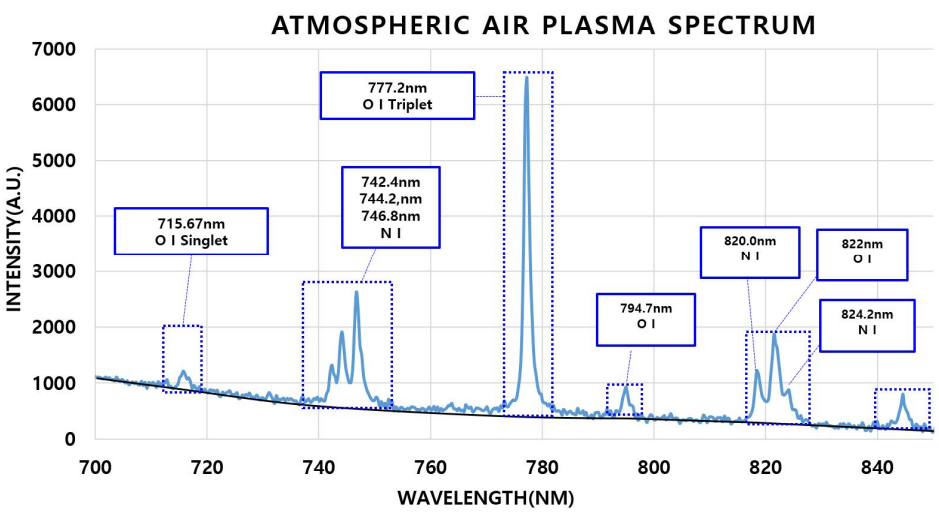

Figure 3.7 Typical air plasma spectrum captured in 700 – 840 nm.

3.3.2 Plasma temperature

Plasma temperature, one of the most important plasma parameters that impact plasma dynamics, can be estimated using optical analysis in conjunction with LTE assumption. In LTE assumption, the rapid collisional (1) excitation, (2) de-excitation, (3) ionization, (4) and recombination processes are assumed to dominate the re-population of the excited state compared with the slow radiative decay of the upper-state. The most popular necessary condition for LTE assumption in laser-induced plasma is the McWhirter criterion, where the electron number density should be greater than a critical value that depends on plasma temperature [69, 70]. While the criterion is the pre-requisite and doesn't necessarily hold the complete condition of LTE, many researchers have simply assumed LTE to about 4000 microseconds after the plasma formation. Here, the convention is followed within the aforementioned temporal regimes (200 – 3000 ns), species (air), wavelength (715 nm, 777 nm), and environmental conditions (1 atm, 25 ℃) [71, 72].

Using Eqn. 3.5, the plasma temperature can be expressed using two specific line intensity of a single atom/ion.

$$\frac{I_1}{I_2} = \frac{g_1 A_1}{g_2 A_2}\frac{\lambda_1}{\lambda_2}\exp\left(-\frac{E_1 - E_2}{kT_{exc}}\right) \tag{3.6}$$

In Eqn. 3.6, the temperature on the right-hand side can be assumed to be the same as the electron temperature. This implies that the temperature used for the electron energy distribution function (EEDF) is the same as the temperature in the atomic state distribution function (ASDF).

The detail of the experimental procedure for the calculation of plasma temperature is well-described in [72]. In the current experiment, two atomic oxygen lines at 715 nm and 777 nm are used, and the camera gate delay time from 200 ns to 3000 ns and variable gate width from 10 ns to 100 ns are chosen. Figure 3.8 shows the plasma temperature decaying from a time delay of 0.2 to 3000 microseconds.

The calculation of temperature earlier than 200 ns is not attempted due to the strong broadband plasma emission that obscures line emission features. On the other hand, the LTE assumption is not valid for the time delay longer than 3000 ns due to the decreased collisional rate of an electron with heavy particles.

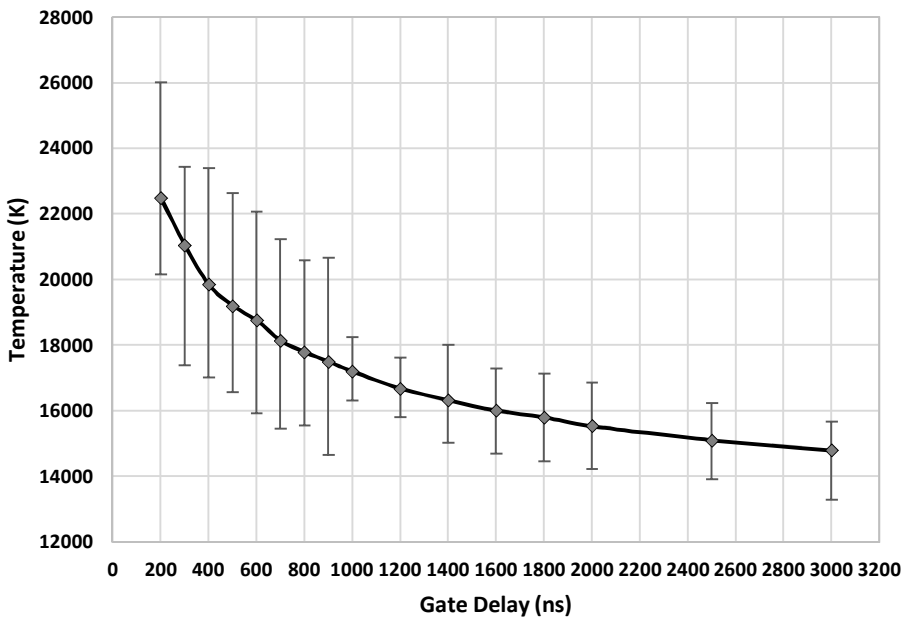

Figure 3.8 Time-dependent zero-dimensional plasma temperature measured in 200 – 3000 ns.

The line to continuum ratio, $\varepsilon_l / \varepsilon_c$, can be measured using the emission spectrum, and it is only a function of electron temperature (T_e) and constants [73]. The T_e calculated using the measured ratio ($\varepsilon_l/\varepsilon_c$), some assumptions, and Eqn. 3.2 can then provide the electron number density (n_e). Alternatively, when a captured spectrum contains multiple emission lines of a species, the ratio of the lines (e.g., the ratio of two lines corresponding to an i-to-j transition and a k-to-l transition (i.e., $\varepsilon_{l\ i-j}/\varepsilon_{l\ k-l}$)) is only a function of the T_e and known constants (Eqn. 3.1); thus,

the T_e can be determined as well. In addition, the emission line width is a widely used indicator of n_e, particularly when a hydrogen line appears in the emission spectra [74, 75]. The hydrogen emission line width is a function of T_e and n_e, as tabulated in ref. [76]; thus, the n_e can be estimated using the measured line width and the calculated T_e. Once the n_e and T_e are estimated as explained above, the atomic emission line intensity can then be used as an accurate indicator of the number density of the atomic species. The measurement result of the line-to-continuum ratio at 777 nm of oxygen line is presented in Fig. 3.9. The plasma emission was sampled at the multiple plasma locations (LOC 0 ~ LOC 4) by fine-tuning the lens position with 0.1mm resolution. The distance of each location in plasma is 0.5mm. It is noteworthy that the temporal temperature profile varies with the sampling position, but the line-to-continuum ratio can be plotted against the single plasma parameter.

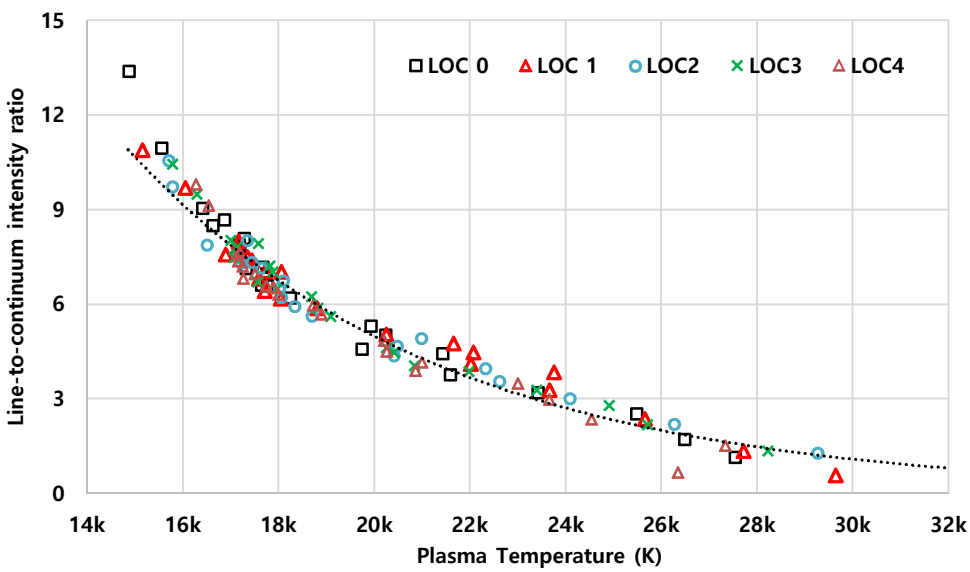

Figure 3.9 Line-to-continuum intensity ratio extracted from plasma emission spectra at the multiple plasma locations (denoted as LOC X).

Chapter 4 Development of non-intrusive LIBS

4.1 Overview of LIBS measurement

In thermofluidic systems, fast detection of flow properties is essential to systematically control the fluid motion and reaction rate. A sensor-based conventional measurement system is, however, slow (~ms), vulnerable to corrosion, and highly intrusive that can seriously perturb the original flow. The problem is exacerbated, in particular, when the target flow is confined, reacting, and/or pressurized. For instance, the temperature ranges of a shock wave or flame easily exceed the melting point of widely-available thermocouples. Alternatively, non-intrusive in-situ optical measurement methods have been proposed and developed that minimally perturb and interact with the target flow. In order to induce the photon-matter interactions forming the virtual measurement probing volume, the optical techniques generally require external photon sources that have different power levels: low power (mW) for absorption spectroscopy and high power (MW) for laser-induced fluorescence, Raman scattering, Rayleigh scattering, and laser-plasma spectroscopy.

Laser-induced breakdown spectroscopy (LIBS) is a quantitative optical measurement method that provides composition and density information extracted from plasma emission spectra. In order to induce plasmas of sufficient photon emission, high-power nanosecond-to-femtosecond laser beams are focused, causing dissociation and photo-ionization in the target (Fig. 4.1). The high-temperature plasma emits a broadband light, which is collected by a spectrometer to provide instantaneous emission spectra. Compared to other laser-based techniques (e.g. spontaneous Raman scattering [4]), LIBS requires a simpler optical setup, single optical access point (e.g., a single window), and lower input laser energy, but provides a higher signal-to-noise ratio (SNR). Therefore, this optical measurement

has enabled real-time composition and density monitoring. For example, the local equivalent fuel-air (F/A) ratio was monitored in flames and combustion products [11-14], power-plant combustors [15, 16], and propulsion systems [17-20].

Various peak intensity correlations (e.g., [11]) of different atomic/ionic species have been used for LIBS engineering applications. For general LIBS calibration, the strongest atomic peak is selected among neighboring spectral peaks to normalize with its maximum intensity (to provide better SNR and precision of the measurement). The time-delay and gate-width are the choices of the researcher, and the optimal choice would strongly depend on the specific experimental conditions/constraints and properties of the measurement target medium. Thus, particularly for measurement purposes, the information of time-delay and gate-width should be also provided to compare the performance levels LIBS, and the choice need not be the same.

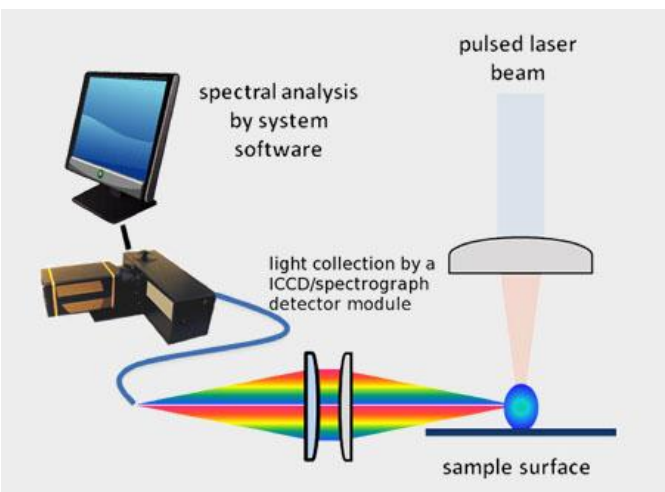

Figure 4.1 Schematic diagram of a typical LIBS measurement setup.

4.2 Experimental setup

4.2.1 Absorption measurement setup

In this section, a detailed description of accurately measuring plasma absorption energy (APE) will be presented. An optical setup measuring the APE in laser-induced plasmas is illustrated in Fig. 4.2. Two integrating spheres (IS) placed are used for monitoring the incident and transmitted pulse energy. The laser beam is focused at the center of another integrating sphere (C-IS) to induce a breakdown plasma. The reflector cap (RC) blocks the outlet of the C-IS when measuring the sum of transmitted and scattered pulse energy (TSE). With the RC on, the integrating sphere (C-IS) has only a single hole for taking the converging laser beam in, and thus little light escapes (the inlet area is much smaller than the entire internal surface area). The APE in the plasma at the center of the C-IS will be dissipated and used to heat the gas. On the other hand, the laser photons scattered on and transmitted through the plasma will be subsequently scattered and uniformly distributed by the IS. These photons will be detected by the photodiode attached to the surface, and the output signal intensity corresponds to the TSE.

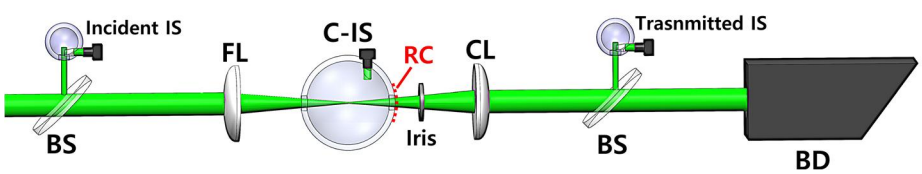

Figure 4.2 Schematic of the experimental setup measuring plasma absorption energy (APE).

BS, beam splitter; BD, beam dump; CL, collimating lens; FL, focusing lens; IS, integrating sphere; RC, reflector cap.

Plasma emission is found to be negligible in comparison with the TSE. The APE is evaluated by subtracting the TSE from the incident pulse energy (IPE). The transmitted pulse energy can be measured individually as well with the RC off and using the downstream IS.

4.2.2 Spectrum measurement setup

As the fraction of APE increases with the IB process activated, the measurement target species will significantly be heated, eventually causing remarkable fluid disturbances, chemical reformation and reactions. In flammable mixtures, the IB-induced gas heating can initiate combustion chain reactions [24]. It was reported that a high-temperature (4,000 K - 10,000 K) region persisted up to 20 μs after the gas breakdown induced by ns-laser pulses [35], which is more than sufficient for combustion ignition. Nevertheless, for non-intrusive LIBS measurements, particularly in flammable mixtures, the IB process should be limited; thus, the laser pulse width needs to be reduced below a certain value.

A schematic experimental setup used for the LIBS measurements in flammable mixtures is shown in Fig. 4.3. Linearly polarized, 2nd harmonic (λ = 532nm) ns-laser pulses are generated by a Q-switched Nd:YAG laser (Continuum, PL 8000) operating at 10 Hz repetition rate. The laser output is set to the maximum value (approximately 400 mJ/pulse), to guarantee the optimum lasing stability and constant pulse width (6 ns FWHM). Pulse-to-pulse energy fluctuation is estimated to be $\pm$ 4 % (relative standard deviation, RSD) with $\pm$ 0.5 ns timing jitter. A thermopile (Ophir) power meter is used for measuring time-averaged pulse energy. The laser pulse energy is controlled using a motorized rotating half-wave plate and a polarizing beam splitter (the energy attenuation optics in Fig. 4.3). The laser beam leaving the attenuation optics is then focused into an optically accessible (fused-silica windows on 4 sides) stainless-steel pressure chamber by an f = 75 mm plano-convex lens (FL1). The chamber is pressurized with dry air at P_{cell} = 0.1 – 10 bar and

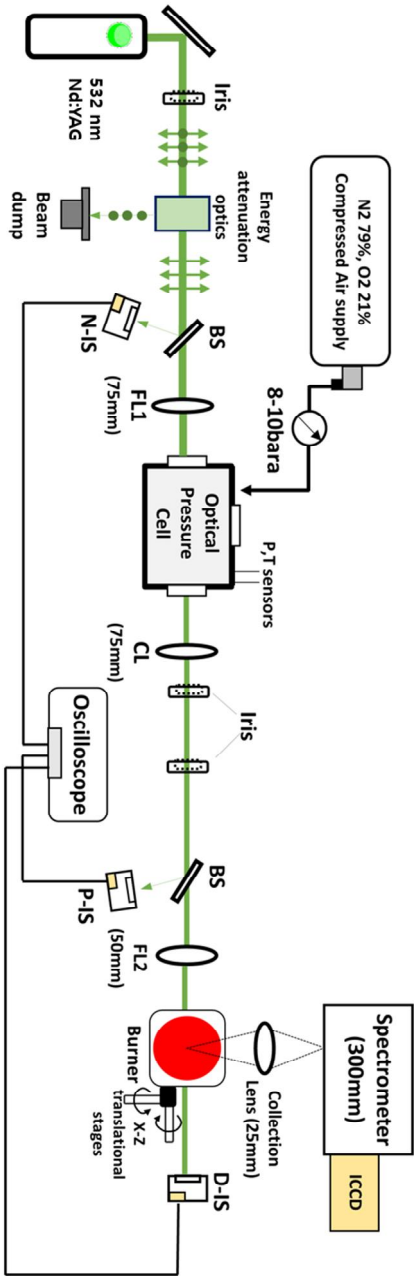

Figure 4.3 Schematic diagram of LIBS setup with a pulse-chopping pressure cell.

Reprinted with permission from [2] ©Elsevier.

continuously ventilated by an air stream through the cell to avoid influences of preceding laser pulses. The minimum chamber pressure causing IB-dominating optical breakdown is estimated to be approximately 0.02 bar; i.e., the laser beam passes through the cell nearly unaffected when $P_{cell} < 0.02$ bar. Otherwise, at higher pressure, intense air breakdown is observed inside the chamber with reasonably high pulse energy.

In the presence of the breakdown plasma at the focus, the laser pulse energy will be partly absorbed, scattered, and transmitted [20]. The scattered beam from the plasma is effectively blocked by multiple irises placed downstream of the cell, and the transmitted beam is collimated using another plano-convex lens (CL1), also having a focal length f = 75 mm. The collimation lens (CL1) is placed to keep the original beam size (12 mm in diameter) after the beam is delivered at the laser focus. The pulse characteristics (e.g., pulse width and pulse energy) of the transmitted beam are recorded using a 12.5 GHz fast-photodiode (EOT, EOT-4000F); the laser beam is sampled before and after the pressure cell (using an uncoated window as a beam-splitter) and then after the target burner. In each case the sampled beam is directed to an integrating sphere with an attached photodiode (Thorlabs, SM05PD2A, 500-MHz bandwidth); photodiode waveforms are then recorded using a 1-GHz bandwidth oscilloscope (Keysight, MSO-X 3104A). The collimated beam is then re-focused by another plano-convex lens (FL2, f = 50 mm) above a custom-built premixed burner. The distance between the first (in the pressure cell) and the second (at the target location) foci is 1.2m; therefore, the time separation of the two consecutive breakdowns is approximately 4 ns. Figure 4.4 shows the photograph of the experimental setup. Two laser focal points of gas breakdown are enlarged and displayed in the red squares. The first breakdown plasma is occurring in the optical pressure cell for laser pulse chopping, and the consecutive breakdown plasma is used for LIBS measurement in a flammable burner. The plasma emission from the secondary focus is collected by an f = 25 mm bi-convex lens to be focused onto a vertical entrance slit (20 μm) of a spectrometer with 300-grooves/mm diffraction

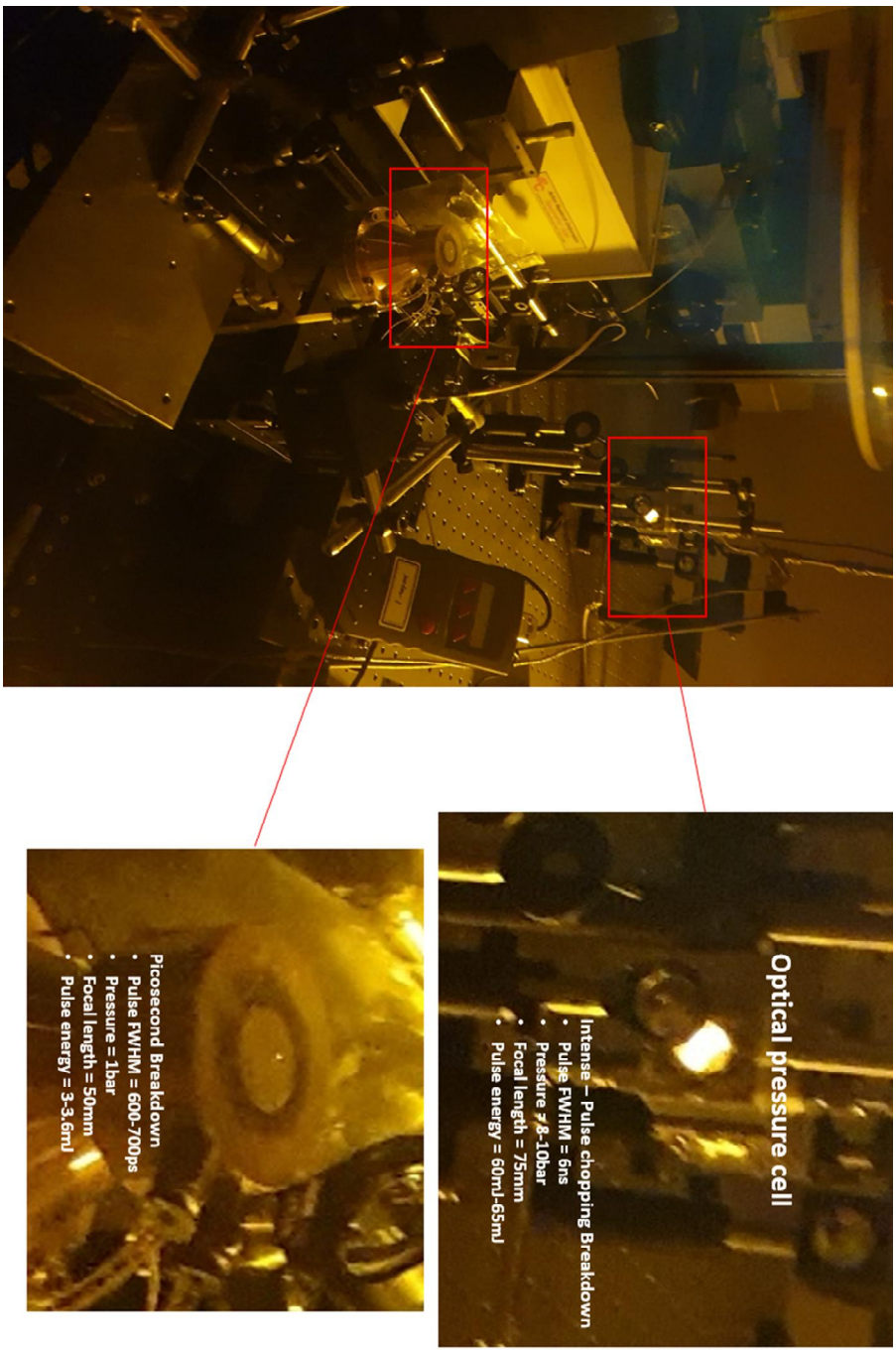

Figure 4.4 A photograph of optics alignment in the LIBS setup.

grating blazed at 500 nm (Acton Research, SpectraPro 300i). An ICCD camera (Princeton Instruments, PI-MAX with Gen II intensifier, 512 x 512-pixel array) is placed at the spectrometer exit plane to capture the instantaneous plasma emission spectrum at 0.5 nm/pixel resolution. The gate delay (t_d) from the arrival of the laser photon at the focus and gate width (t_w) to capture the short-lived emission signal is 20 ns and 60 ns, respectively, unless otherwise noted.

In order to capture the plasma emission at a desired time delay after the plasma breakdown, experimental devices are synchronized with the pulsed laser beam inducing the optical breakdown. Figure 4.5 shows the schematic of the signal diagram including a pulsed laser system (Continuum, PL 8000), a delay generator (Stanford Research Systems, DG535), an ICCD camera (Princeton Instruments, PI-MAX II), and an oscilloscope (Keysight, MSO-X 3401A). The master signal of the experiment is generated from the laser system, referred to as the Q-switch advanced signal. This electrical signal is internally triggered at 10 Hz repetition rate. The yellow signal in Fig. 4.6 is adjustable and preceded by 180 ns of the actual beam arrival at the focus (green signal in Fig. 4.6). After the master signal generation, all the equipment is electrically synced prior to the laser beam delivery. The electrical signal generated from the laser is firstly transferred to externally trigger DG535. The 4-channel programmable delay generator is primarily used for adjusting the time delay capturing the plasma emission. Multiple signals generated from DG535 are in turn propagated to control the gating of the ICCD camera and the oscilloscope data acquisition. The insertion delay of individual equipment and electricity propagation in BNC cables are simultaneously added to match the resultant gate delay (Fig. 4.7) for spectrum acquisition. Characteristics of electrical pulses (e.g. timing and amplitude) are detailed in the chronographic diagram in Fig. 4.7.

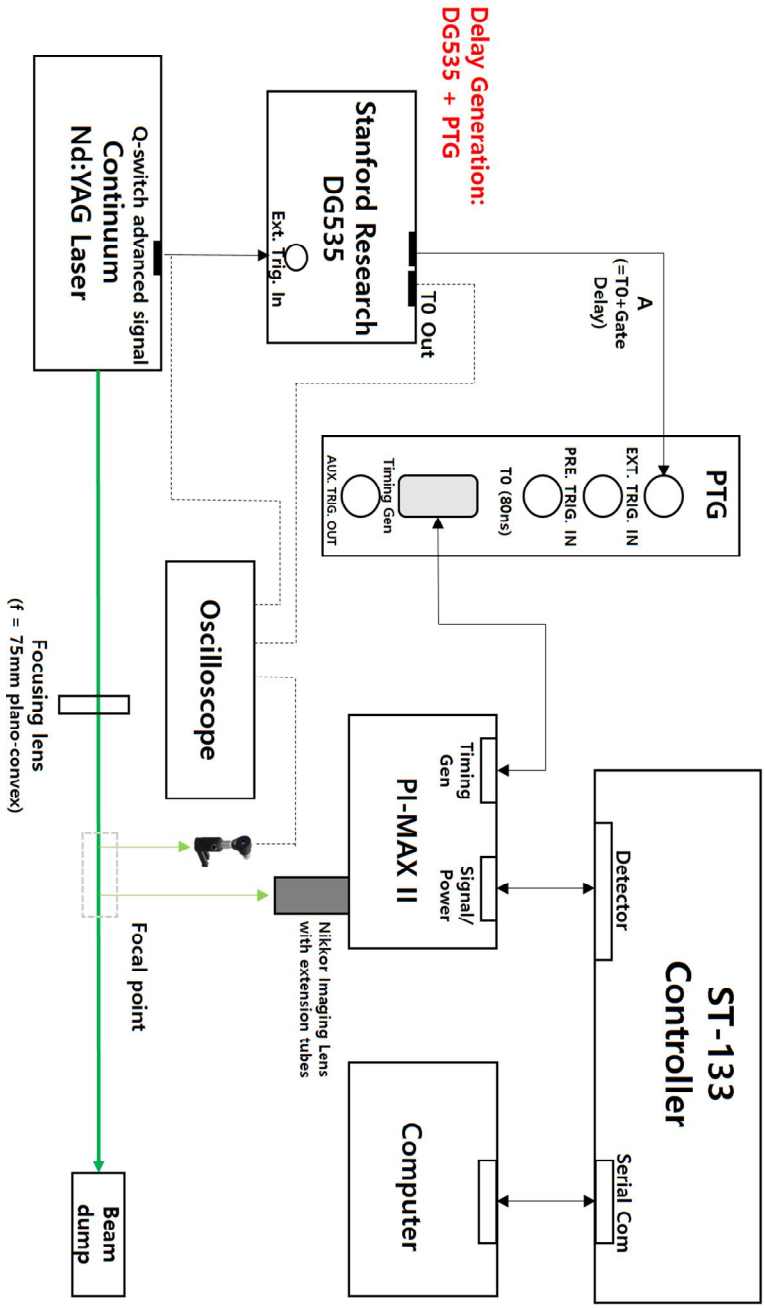

Figure 4.5 Signal flow diagram of LIBS measurement.

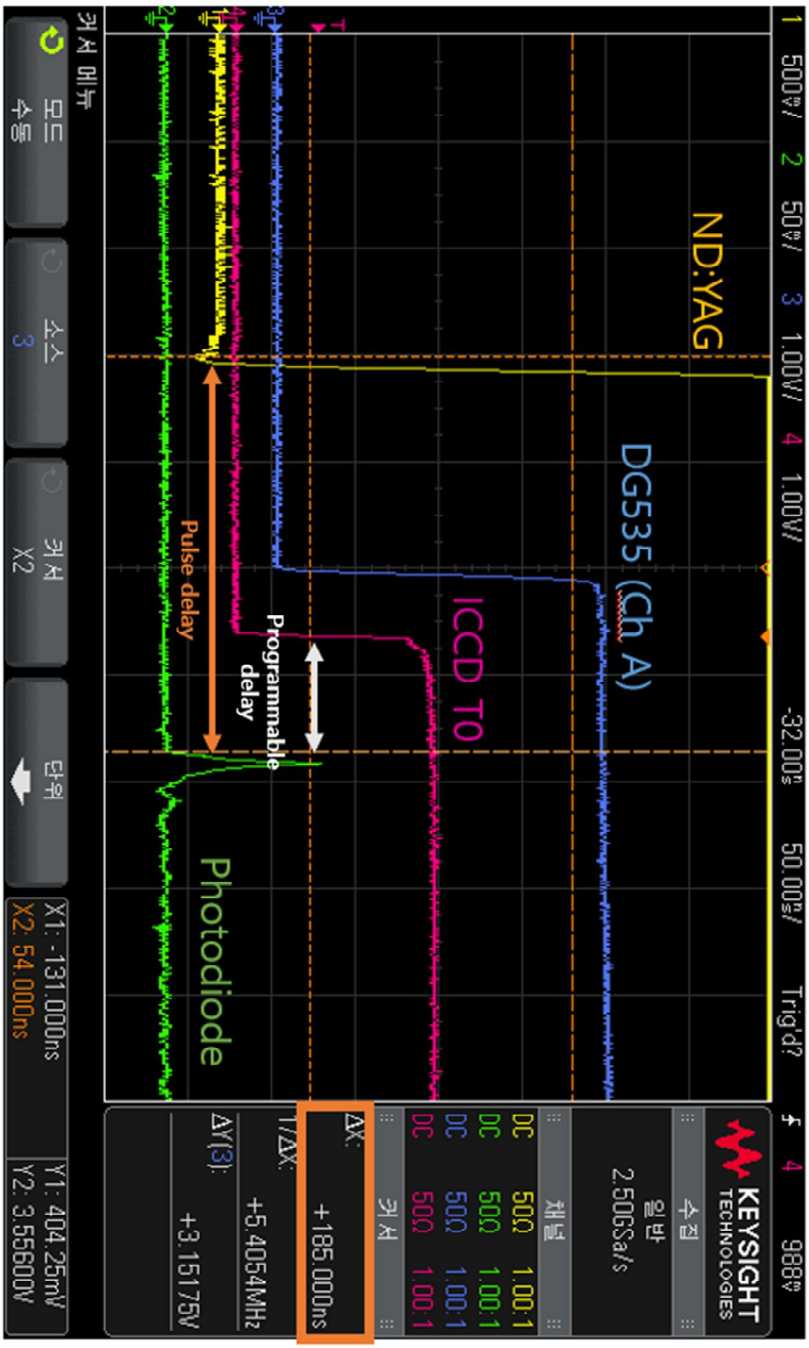

Figure 4.6 An oscilloscope image showing the hardware and light signals.

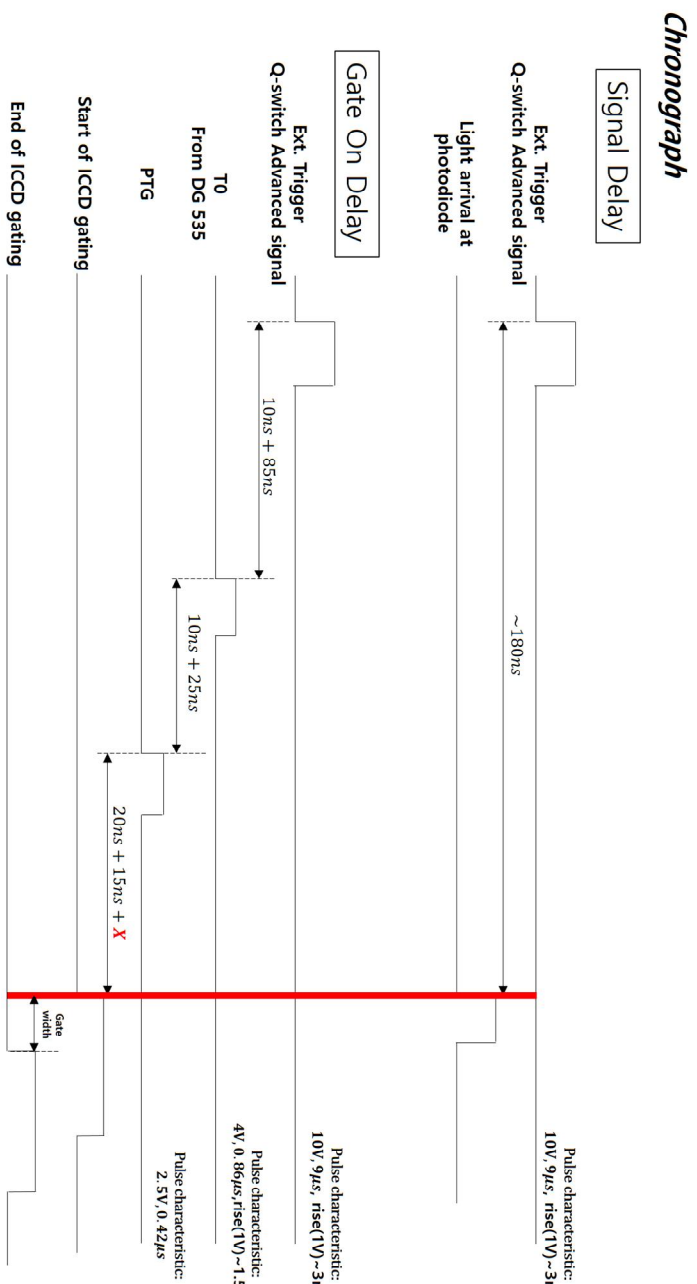

Figure 4.7 Experimental timing diagram (chronograph) of LIBS measurement.

4.3 No-ignition by plasma

In general, short-duration and high-power-density laser pulses are necessary for generating low-temperature plasmas of strong photon emission intensity via mitigation of the IB photon absorption process. Noack [33] showed that the APE in water differs with varying pulse width, which alters the dominating photon absorption mechanism. In another recent study utilizing fs-laser pulses for combustion diagnostics [34], it was reported that an extremely small fraction of the laser pulse energy (<1 %) was deposited in the plasma filamentation volume, while over 80% of pulse energy was absorbed in ns-laser-induced plasmas [24, 26, 31]. In this study, a newly devised pulse chopping technique is employed to provide sub-ns pulses of proper pulse width for generating such plasmas using a typical ns-laser source.

An ns-laser pulse (e.g., black dotted curve in Fig 2.11) is focused into a pressure cell to induce gas breakdown. The breakdown, however, does not occur instantaneously since the leading edge of the Gaussian pulse is below the breakdown threshold intensity and the electron number density in the focal volume is insufficient for IB-dominating photon absorption during the time delay. Prior to optical breakdown, air in the cell is almost perfectly transparent to the laser beam. Nevertheless, the intense IB photon absorption after the breakdown suddenly makes the medium opaque, acting as a virtual shutter and blocking the beam transmission through the cell. As discussed in Chapter 2, the shutter closing time is controllable primarily by cell pressure. As the cell pressure increases, the number of molecules in the focal volume increases to raise the photon-molecule collision rate and, therefore, to accelerate the initial multi-photon ionization and electron accumulation resulting in earlier IB-dominating breakdown (i.e., faster shutter closing). Similarly, by increasing the number of photons passing through the focal volume—raising the pulse energy while keeping the normalized temporal pulse profile unchanged using

the aforementioned energy attenuation optic—the breakdown delay can be reduced to close the virtual shutter earlier.

In order to avoid the combustion initiation in the presence of the laser-induced plasmas in a flammable mixture, the laser pulse energy absorbed by the plasma (APE) should be below minimum ignition energy (MIE). This is because the APE will ultimately be used to excite and heat the gas molecules and to induce chemical reactions. The MIE depends on the local equivalence ratio, flow conditions, and the manner of energy deposition, e.g., laser wavelength, pulse width/power, and volume of plasma, particularly, for laser ignition. For the test burner, equivalence ratio and flow conditions are fixed, but the pulse width and power of the focused laser beam are varied to find an appropriate pulse profile for stably generating plasmas without initiating combustion. To measure the APE in air with the variation of the laser pulse profile, an extra optical setup is used (Fig. 4.2). Figure 4.8 shows the APE as a function of IPE (incident pulse energy) with ns and ps pulses. Three different plasma modes are observed, depending on the IPE and pulse width, which are 1) stable breakdown with ns excitation (continuous periodic breakdown), 2) unstable breakdown with ns excitation, (irregular sporadic breakdown), and 3) stable breakdown with ps excitation. Breakdown with ns excitation is stable when the pulse energy is higher than 8mJ but is otherwise unstable; the breakdown probability of ~ 25 % is observed at 6.4 mJ/pulse. With ns excitation, the lowest APE is around 2.2 mJ, and it asymptotically approaches the 100 % absorption line as the IPE increases. The error bar indicates the standard deviation. On the other hand, the APE drops steeply in the unstable ns-breakdown regime of low breakdown probability (25% – 50%) revealing the significantly increased fluctuation of APE. However, the true APE of a successful breakdown plasma in the regime is two to four times greater than the measured APE (time-averaged) corresponding to 50%-to-25% breakdown probability. Therefore, even in the unstable regime with ns excitation, the APE of the ns-pulses exceeds the MIE $\approx$ 1mJ [77] of stoichiometric methane-air mixtures, which is indicated by a blue dotted horizontal line in Fig. 4.8. This is confirmed with

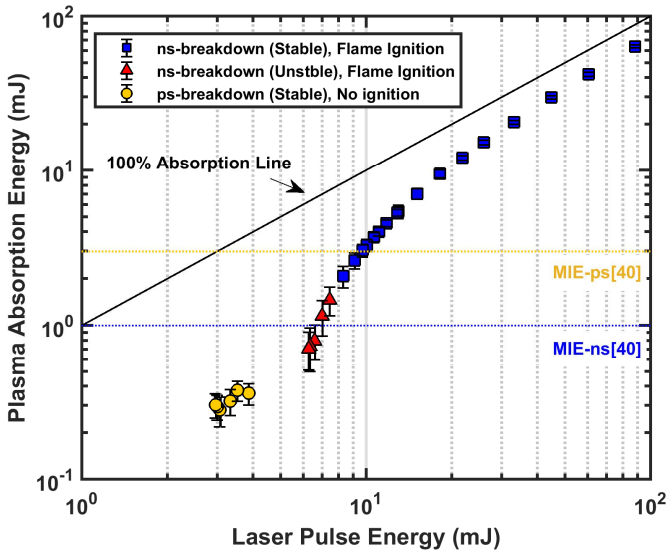

Figure 4.8 Absorbed pulse energy (APE) of laser-induced plasma generated by different laser pulse-width (ns, ps).

*Reprinted with permission from [2] ©**Elsevier.***

the minimum ns pulse energy of 6.4 mJ/pulse focused into a stoichiometric methane-air flow: ignition results whenever breakdown occurs. The APE in the stoichiometric fuel-air mixture would be different from that in air due to the addition of methane; however, the difference would be insignificant because the fuel mole fraction is below 10%. According to the report of Lim et al. [78], MIE for a stoichiometric methane-air mixture measured using a focused 532 nm laser beam increases from 1 mJ to 3 mJ as the pulse width decreases from 10 ns to 30 ps, primarily due to the reduced spark kernel size. In the stable ps-breakdown regime (in the current work), the pulse energy (IPE) is varied in a narrow range of 3 – 4 mJ. The pulse width and corresponding pulse energy are controlled by varying the cell pressure (8 – 10 bar). The APE is much lower in the ps excitation regime, down to 0.3 – 0.4 mJ, which is only one-tenth of the IPE; additionally, the breakdown probability is 100%. It is evident that stably generating plasmas of such low APE is impossible with ns-pulses.

Additionally, breakdown plasmas with ps excitation do not initiate combustion for the same stoichiometric mixture. The RSD of the ps-pulse absorption is found to be typically 5 – 8 %, which comes primarily from the pulse-to-pulse variation of the laser source. This fluctuation might be reduced by employing an injection-seeded laser, but in any event, the recent work has shown that a saturable absorber is effective for reducing the fluctuation in APE [1].

4.4 Plasma spectrum

4.4.1 Experimental result

Plasma emission with ps excitation is captured in a spectral range of 550 – 670 nm by a spectrometer. Atomic emission lines of N II (567nm) and H (656nm) are chosen in the spectral range to represent the population of air and fuel molecules, respectively. The peak intensity ratio (PIR) of the two selected lines, i.e. H/N PIR, is correlated to the equivalence ratio (∅).

Emission spectra with ps excitation (3 mJ/pulse, 600 ps FWHM) in air are shown in Fig. 4.9. These spectra are acquired with a 10 ns time interval ($t_d = 10 - 80\ ns$) and a fixed gate width ($t_w = 10\ ns$); the laser arrives at the focus at $t_d = 0$ ns. The strong continuum (Bremsstrahlung) emission grows until t_d = 20 ns and

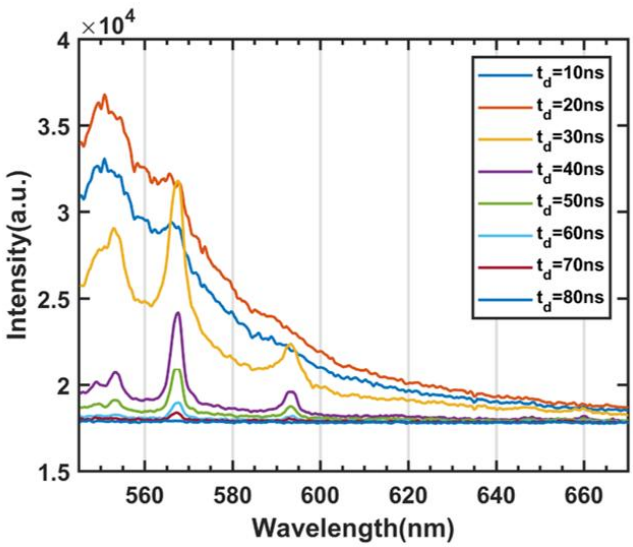

Figure 4.9 Time-averaged sequence of ps-LIBS emission spectra with 10 ns measurement time interval.

Reprinted with permission from [2] ©Elsevier.

gets weaker quickly afterward such that atomic emission lines are evident at this point. The increase of the continuum emission observed during $t_d = 10 - 20\ ns$ indicates collision-dominated electron growth in the plasma [30]. To extract clearly distinguished atomic emission lines with sufficiently high strength and SNR, the camera exposure is chosen to be $t_d = 20 - 80\ ns$ ($t_w = 60\ ns$); the plasma emission signal completely disappears at $t_d >$ 80 ns. The emission spectra with ps excitation in methane-air mixtures of various equivalence ratios are presented in Fig. 4.10. Each emission spectrum is a baseline-subtracted average of 100 instantaneous spectra that are normalized by the peak intensity of N II line centered at 568 nm. In all normalized spectra, both the height and line width of the atomic/ionic N peaks at 555 nm, 568 nm, and 595 nm are almost identical. This indicates that their time-evolution is not remarkably affected by the addition of the fuel (CH_4) under the fixed pressure and temperature flow condition. More importantly, it is apparently shown that the H peak intensity at 656 nm relative to the N II peak intensity monotonically increases as $\emptyset$ increases; therefore, the H/N PIR can be used as an indicator of $\emptyset$.

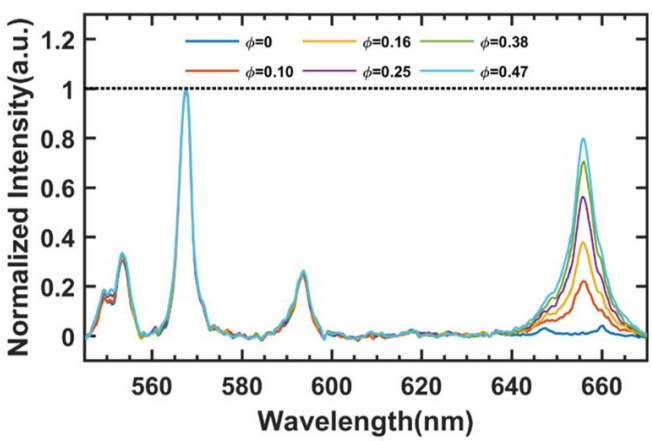

Figure 4.10 Normalized ps-LIBS spectra with varying fuel concentration (Ø).

Reprinted with permission from [2] ©Elsevier.

Note that the flame is not ignited over the entire range of $\emptyset$ including the highly flammable regime of $\emptyset$ = 0.5 – 1.5 in the presence of the laser-induced plasmas; thus, non-intrusive LIBS measurements in flammable reactant mixtures using a typical ns-laser source are enabled.

As mentioned in the previous study [27], in general, the broadband emission caused by the stochastic electron avalanche is stronger with the ns-LIBS in comparison with that of ps-LIBS. However, the SNR was estimated after the baseline was subtracted from the raw spectrum. Recall that the subtraction of the baseline does not reduce the signal fluctuation amplitude or uncertainty of the line strength quantification. The broadband emission intensity profile is relatively stable, particularly more stable in ns-laser induced plasmas, considering the strong atomic emission line intensities that are chosen for the PIR quantification. Here, Signal Intensity $/\sigma_{noise}$ is defined as the SNR, where σ_{noise} is the standard deviation of the broadband emission near the emission line. The baseline that was subtracted from the raw spectra is in practice the average of the broadband emission.

The high signal-to-noise ratio (SNR) of the ps-LIBS in comparison with other non-intrusive techniques (e.g., Raman and Rayleigh scattering) is a critical benefit of the method. Due to the high SNR, the pulse energy used for this ps-LIBS is a small fraction (i.e., 1 – 5 %) of that used with Raman and Rayleigh scattering. The SNR is evaluated using the ratio of line intensity(I_{peak}) to the average noise of the signal (σ_{noise}), i.e. $\frac{I_{peak}}{\sigma_{noise}}$. In Fig. 4.10, the single-shot SNR of the N-line (568 nm), which is selected for the spectrum normalization, is estimated to be 250, and the SNR of the H-line (656 nm) is approximately 30 at the minimum equivalence ratio of $\emptyset = 0.1$, and greater than 800 at $\emptyset = 1.5$. The minimum quantification limit (SNR $\approx$ 10) of the fuel concentration measurement is estimated to be $\emptyset = 0.03$ at the standard condition (P = 1atm, T= 25℃).

The calibration results, i.e. H/N PIR (peak intensity ratio of H at 656 nm and N II at 568 nm) versus $\emptyset$, are presented in Fig. 4.11 and Fig 4.12 for 6 ns pulses and

600 ps pulses, respectively. The ns -pulses ignite the mixture when the equivalence ratio at the focus is in flammable range. Then, the plasma emission spectrum, e.g., strength and profile, is remarkably affected by the significant decrease of gas density, which has been observed in previous studies [20]. Figure 4.11 shows the H/N PIR versus $\emptyset$ with ns-duration pulse energy of 50mJ and 120mJ. The effect of ignition on the ns-excitation plasma emission spectrum, captured at $t_d = 200ns$ for a 10-ns gate width $(t_w = 10\ ns)$ is shown in Fig. 4.11.

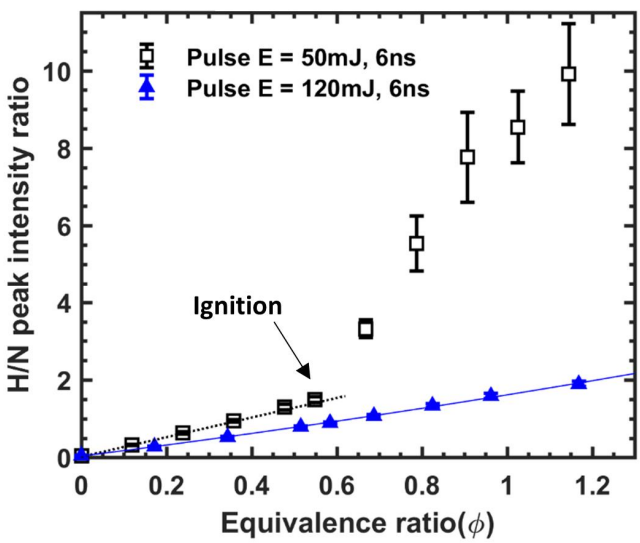

Figure 4.11 Hydrogen (656 nm) / Nitrogen (567 nm) atomic line emission PIR vs. $\emptyset$ for ns-pulse-induced plasmas with burner ignition at $\emptyset = 0.5$.

Reprinted with permission from [2] ©Elsevier.

The slope of H/N PIR abruptly increases at $\emptyset$ = 0.53 when the burner flow is ignited by the 50 mJ pulse. Recall that the first ns-laser pulse (of the set of 100) is sufficient for ignition, and therefore, the plasma generated by the following laser pulses is in high-temperature combustion products. After the ignition, the overall

plasma emission strength gets weaker due to the reduced gas density, and in particular the 568 nm N-line intensity is significantly weaker, causing the sudden rise of the H/N PIR, as shown in Fig. 4.11 when the pulse energy is 50 mJ (black). The collapse of the N-line is even more remarkable at higher $\emptyset$; therefore, the uncertainty of the H/N PIR abruptly increases in the high-$\emptyset$ range (as indicated by the larger error bars). This behavior may be due to insufficient pulse energy absorption of product gases, resulting in the reduction of plasma volume and faster quenching of the excited N II ion. Interestingly, the ignition does not affect the linear correlation of the H/N PIR versus $\emptyset$ when the pulse energy is 120 mJ, as shown in Fig. 4.11(blue), perhaps due to the increased photon energy absorption (which decelerates quenching N II ion); consequently, the influence of the ambient condition becomes negligible. It is evident that the plasma generation in the flammable mixture significantly alters the measurement target condition via ignition, and the increased pulse energy raises the risk of damaging the optics and optical access windows when the target mixture is confined.

The case of ps pulses (600 ps FWHM) is presented in Fig. 4.12. The pulse energy used for breakdown is only 3 mJ. A monotonic correlation of the H/N PIR versus $\emptyset$ is shown in a wide range of $\emptyset$ = 0 – 1.8; the 'ignition-free' data points are well-fitted (R^2 = 99 %) to a single line. The calibration function can be used for measuring the $\emptyset$ of methane-air mixtures at atmospheric conditions. In this case, the plasma emission is captured between $t_d = 20 - 80\ ns$ ($t_w = 60ns$); recall that the emission disappears after 80 ns delay. Consistent with the previous work [24], therefore, the measurement becomes independent of flow velocity at the measurement location in general, considering the extremely short signal generation ($\tau_{pulse} = 600\text{ps}$) and acquisition ($t_d = 20 - 80ns$) time scales.

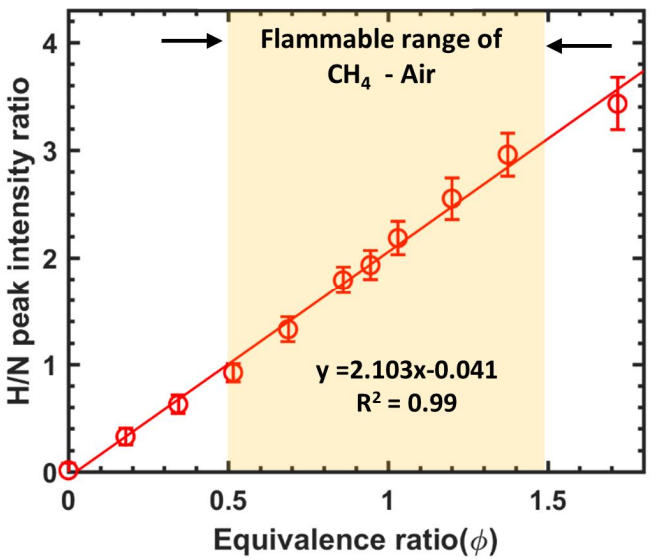

Figure 4.12 Hydrogen (656 nm) / Nitrogen (567 nm) atomic line emission PIR vs. Ø for ps-pulse-induced plasmas without burner ignition.

Reprinted with permission from [2] ©Elsevier.

4.4.2 Performance

In Fig. 4.13, the transmitted laser pulse intensity profiles are presented to be compared with the original ns pulse shape. The pulse energy of the ns-laser beam is kept at 65 mJ/pulse prior to being focused into the pressure cell. The red curve of 605 ± 40 ps FWHM is the pulse profile after the beam exits the cell when the pressure is maintained at 10 bar. The pulse energy of this ps-pulse is measured to be $3.1 \pm 0.2\ mJ$ (7.1 % RSD). The pulse-to-pulse variation is mainly attributed to the breakdown instability caused by the intensity fluctuation of the original ns-pulses to cause earlier or delayed IB activation at the focus in the pressure cell.

The power of the transmitted pulse is estimated to be 3.1 mJ/605 ps = 5.1 MW. This is equivalent to 30 mJ pulse energy of an ns-duration pulse having a 6-ns FWHM. Stable breakdown plasmas (100% breakdown probability) and strong

photon emission spectra are observed with the two different laser pulses of the same power (30 mJ/6 ns (ns-pulse) and 3 mJ/600 ps (ps-pulse)) when focused by an identical lens of f = 75 mm ambient condition. However, only the ns pulses initiate combustion chain reactions when focused in a flammable mixture, while the ps pulses do not. This is because of the reduced time duration of the IB process within the ps-pulse-induced plasmas, which limits the accompanying rapid temperature rise within the breakdown region. It is also noteworthy that the breakdown threshold pulse energy, i.e., the minimum pulse energy to stably induce plasmas (all the focused pulses cause breakdown without misfiring), of the ns pulses (6 ns FWHM) is 8 mJ at ambient conditions, which is well above the pulse energy of the ps pulses (3 mJ/pulse, 605 ps FWHM) that are capable of stably generating plasmas. Additionally, it should be emphasized that the 3mJ ps-pulse does not induce the gas breakdown in flames at the current experimental condition.

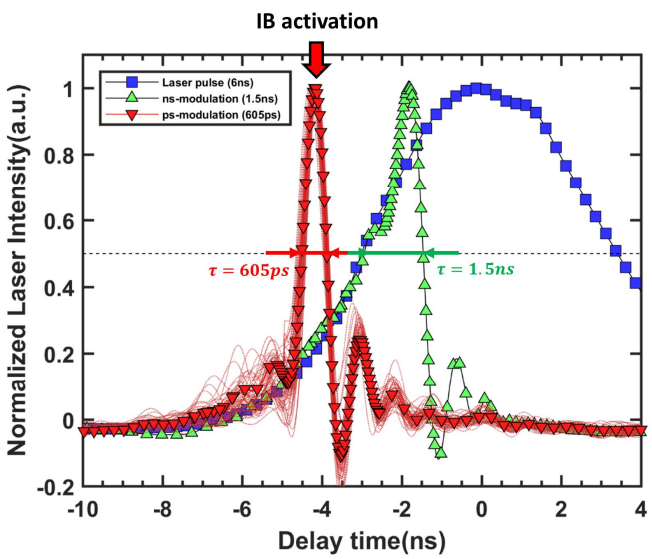

Figure 4.13 Time-trace of shortened laser pulse used for plasma generation in ps-LIBS.

Reprinted with permission from [2] ©Elsevier.

Stimulated Brillouin scattering (SBS) can also be used to shorten the ns pulse width. The pulse-energy conversion efficiency of the SBS pulse-shortening (50 - 75 % [60]) is much higher than the proposed method (5 - 12 % [1]) since the SBS compresses the pulse while the proposed method merely cuts off the trailing part via the abrupt IB photon absorption process. For the same reason, however, the chopped pulses are cleaner and more stable in general than the SBS-compressed pulses. The pulse stability in temporal intensity profile and energy of the chopped pulses can even be further improved with injection-seeding and/or installation of a non-linear saturable absorber (before the high-pressure cell) as shown in the previous work [1]. Recall that the pulse width fluctuation in this study is primarily from the pulse-to-pulse variation of the unseeded-pumping source. Another benefit of the proposed method is convenient pulse width control by adjusting the cell pressure, whereas, the length of the compression tube (water tubes of a few meters (typically 1 – 3 m) in length) should be varied or the tube should be replaced to alter the pulse width of the compressed pulses. Moreover, the operation range of the SBS pulse compression device is strictly limited by various different non-linear optical processes such as the optical breakdown, diffuse Brillouin scattering, and Raman scattering, as reported in [61, 62].

The measurement accuracy was estimated by evaluating and combining the component-level uncertainties. In addition, all possible uncertainty sources potentially affecting the measurement accuracy and precision are identified and reported, e.g., noise from ICCD and microchannel plate (MCP), the uncertainty of measurement target property, baseline correction, and pulse-to-pulse variations of the laser pulse energy and its temporal profile. The uncertainty of the measurement target property disturbed by the focused laser pulses in the target medium is considered negligible since the average flow speed was set to be around 35-40 cm/s in this study, which is fast enough for the plasma-influenced gaseous medium to be convected downstream far away before the next pulse arrives at 100 ms later. The minimum quantification limit of the proposed ps-LIBS is determined by the lowest

SNR limit (= 10) that is set for accurate emission line intensity measurements from the emission spectra.

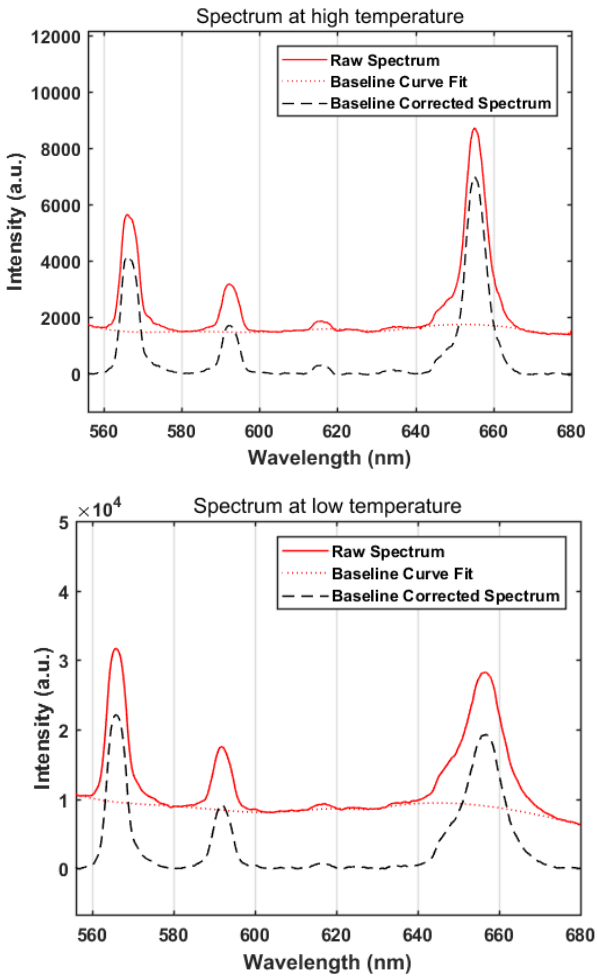

Figure 4.14 Broadband curve fit in signal post-processing (upper: high-temperature plasma, lower: low-temperature plasma).

The typical baseline fluctuation uncertainty was estimated to be around 1.5% of the emission line intensity, which implies that the baseline is quite repeatable in some sense. However, this is strongly dependent on the choice of the time-delay and

gate-width. In this study, baseline curve fittings are obtained using the spline function provided in Matlab. The baseline fitting curve is interpolated from selected points in the spectrum where emission lines are not affecting the intensity at the location. Some examples of baseline fitting are shown in Fig. 4.14.

The baseline continuum emission profile can be physically interpreted as the Bremsstrahlung emission generated by decelerating electrons in a plasma. The strength of the continuum emission highly depends on the electron temperature[79]. In general, the strength of continuum emission is, therefore, weaker when the target gas density is low (or temperature is higher at a fixed pressure) due to the reduced excitation (from lower electron number density) and faster quenching of the plasma. In the two cases shown in Fig. 4.14, it is clear that the continuum emission (or the baseline level) is weaker at a higher temperature. For example, the ratios of continuum-to-line intensity at 567 nm are approximately 0.45 and 0.35 at lower and higher temperature conditions, respectively.

The uncertainty associated with the baseline correction is estimated based on the fluctuation of the emission line strength measured from the baseline-subtracted (or corrected) spectra. For example, Fig. 4.15 shows single-shot baseline fitting curves obtained in 100 repeated measurements, and the baseline-subtracted spectra are shown in the graph on the right-hand side. In Fig. 4.15, the standard deviations of the baseline intensity at 567 nm and 656 nm, where the N and H peaks are located, respectively, are 130 and 150 in the arbitrary unit of the photon detector. Thus, the fluctuation of the PIR due to the baseline correction error can be evaluated:

$$\Delta\ (\mathrm{PIR}) = \mathrm{Max}\left\{\frac{\bar{I}_{H,656\ nm}\pm 2\sigma_H}{\bar{I}_{N,567\ nm}\pm 2\sigma_N}\right\} \approx \frac{21000\pm 300}{23000\pm 260} \tag{4.1}$$

which result in $\pm$ 1 % of PIR fluctuation. In general, the baseline correction error is estimated to be $\pm$ 1 - 3 % of PIR.

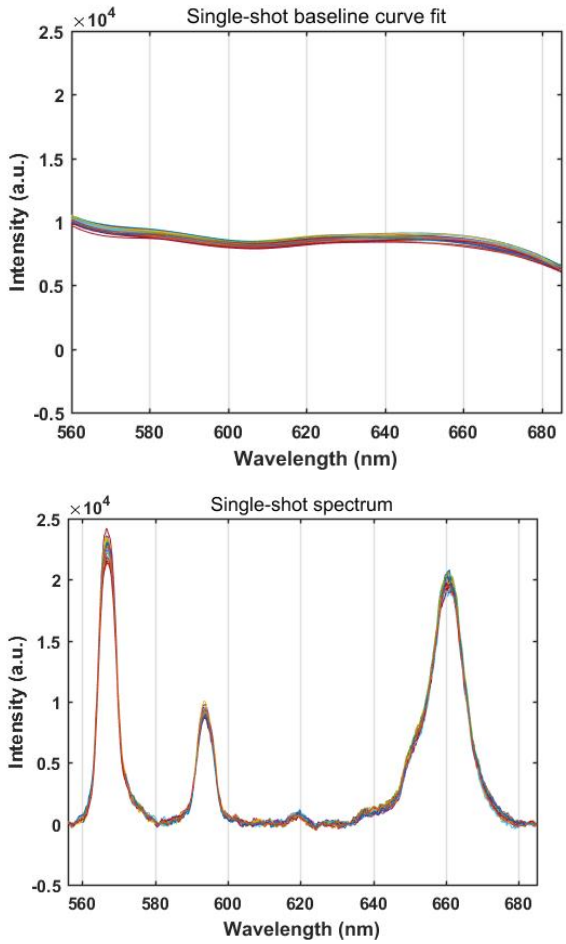

Figure 4.15 Evaluation for curve fitting result with 100 consecutive plasma shots.

The fluctuations in the ps-LIBS measurement results are estimated for comparing with the results of ns-LIBS (± 2.8 – 4.5 %). Among the uncertainty sources listed here, the pulse-to-pulse variations of the ns-pulse energy (± 7.2 %) and its pulse-width (± 6.6 %) would be the primary reason of the increased uncertainty of the ps-LIBS, although the ps-measurement stability is expected to be improved by limiting the stochastic electron avalanche process [55]. Therefore, minimizing the pulse-to-pulse fluctuation of the ns-laser is essential for improving the stability and precision of the ps-LIBS developed in this study; this can be

accomplished with the use of injection seeding (for the Nd:YAG laser) [20] or a saturable absorber (SA) [1]. In addition, the detector shot noise is another source of the random error that contributes approximately ± 1 % of the PIR. Instrumental accuracy of $\emptyset$-measurement using electro-mechanical mass flow controllers (MFCs) is approximately $\pm$ 2.5 % according to the calibration uncertainty provided by the MFC manufacturer. The $\emptyset$ fluctuation during the measurements, however, is assumed negligible considering the 10 Hz pulse repetition (no influence from the previous pulse) and the fully premixed steady flows above a flat-flame burner employed for the calibration purpose. The baseline curve that is subtracted from the emission spectrum is an interpolated spline curve obtained from each individual single-shot spectrum, which typically fluctuates $\pm$ 2 %. The uncertainty range of the PIR associated with the baseline correction is estimated to be $\pm$ 1 - 3.0 %, which is introduced by both the interpolation algorithm and randomness in Bremsstrahlung emission. The composite uncertainty (i.e., precision) of the ps-LIBS utilizing the modulated laser pulses is measured to be approximately ± 6.5 % (± 5.4 – 7.6 single-shot RSD in %) in the range of $\emptyset$ investigated in this study, which is somewhat larger than the uncertainty of ns-LIBS (± 2.8 – 4.5 %). The measurement accuracy (= measured – true concentration value) of the LIBS instrument is evaluated based on the measured averaged concentration and inaccuracy of $\emptyset$ (accuracy of the calibration (≈ 2 %) and the measurement uncertainty of the MFCs that provide the true concentration value (≈ 2.5 %) are considered altogether), which is estimated to be approximately ± 4.5 % with the current calibration setup.

The size of the laser-induced plasma will determine the spatial resolution of LIBS measurements, and it is clear that the plasma becomes much smaller with ps-pulses in comparison with that of ns-pulses. To estimate the size of the plasma, instantaneous plasma images were taken using an intensified CCD camera with a magnification lens and multiple extension tubes. The plasma images presented in section 3.2.1 clearly show the difference in size at the end of the laser pulses. The spatial resolution of the LIBS measurement is estimated to be less than 300 μm in

comparison with the ns-LIBS resolution typically around 1 – 2.5 mm. This improved spatial resolution of the ps-LIBS is due to the limited IB effects to minimize the influences of collisional heating and volumetric growth of the plasma. For comparison, the spatial resolution of Raman and Rayleigh scattering measurements are reported to be 250 μm [80] and 50 μm [81], respectively.

Chapter 5 Demonstration of non-intrusive LIBS

5.1 Development of a flat-flame burner

A custom-built flat flame burner is developed to provide steady flows of flammable stoichiometric methane-air mixtures. As illustrated in Fig 5.1(a), the burner exit plane is made of a 5-mm-thick sintered brass plate surrounded by a cooling water circulation passage (See Fig 5.2). The temperatures of the coolant and the brass burner body are monitored using K-type thermocouples to be kept constant at 25 ± 1 °C with feedback-controlled water cooling and electric heating (See Fig 5.3). The flow speed at the burner exit is set to be 2 – 3% higher than the calculated flame propagation speed to sustain the flame 1mm above the water-cooled burner surface; the burner exit velocity $(U_{exit}) = 38.5 \pm 0.2$ cm/s and the laminar flame speed at the condition $(S_L) = 37.6$ cm/s. A decrease in flame speed due to radiation heat loss is neglected in adjusting the experimental flame speed. The 1-D flame speed and adiabatic flame temperature were calculated theoretically using Chemkin-Pro 19.2 with detailed GRI 3.0 reaction mechanisms. Figure 5.4 shows the flame speed variation for different fuel concentrations at two inlet gas temperatures T_{in} = 5 ℃ (red circle) and T_{in} = 25 ℃ (blue circle). Note that the flame speed (cm/s) varies with the inlet gas temperature; the flame speed varies more than 10 % when the gas temperature is increased by 20 ℃ in the premixed stream (See Fig. 5.5). Figure 5.7 shows images of the stable flat flame operating at equivalence ratio $\emptyset$ = 0.8 – 1.2.

The height of the probing location above the burner exit plane (HAB) is set to z = 2 mm, 5 mm, 10 mm, 20 mm, and 40 mm with ± 0.1 mm accuracy (Fig. 5.1(b)). The red-dotted square shows the measurement region (30 × 40 mm) in which the

LIBS probe is located at 126 different measurement points: 21 points at each HAB (one at the center and 10 points on both sides 1.5 ± 0.1 mm separated horizontally).

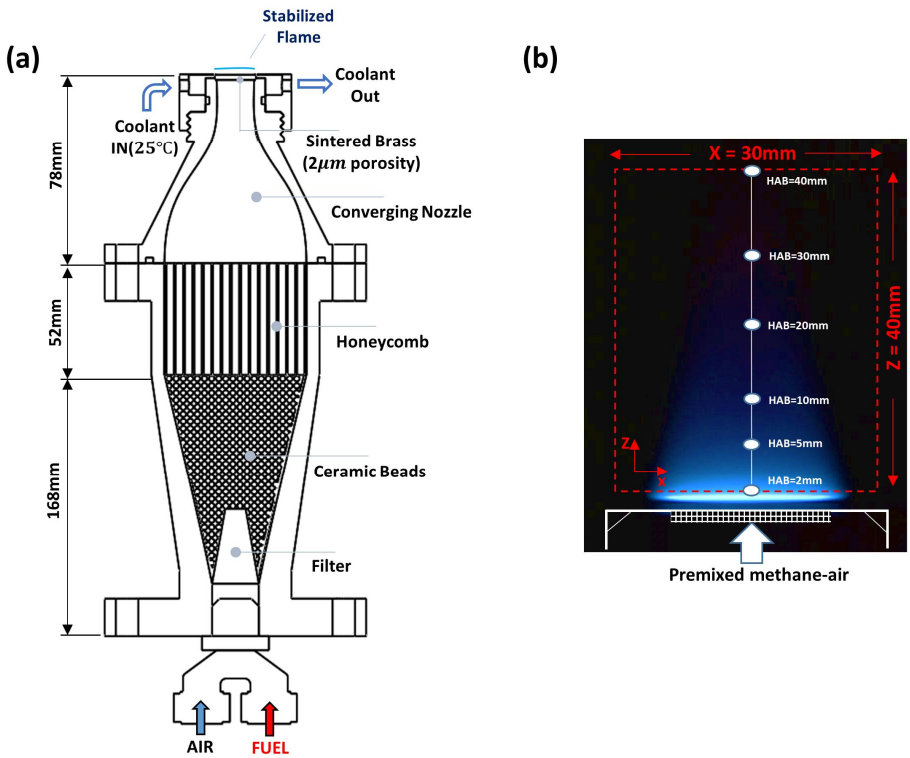

Figure 5.1 (a) A drawing of the custom-built laminar flat-flame burner, (b) a photograph of the steady-state flame in operation at $\emptyset = 1$.

Reprinted with permission from [2] ©Elsevier.

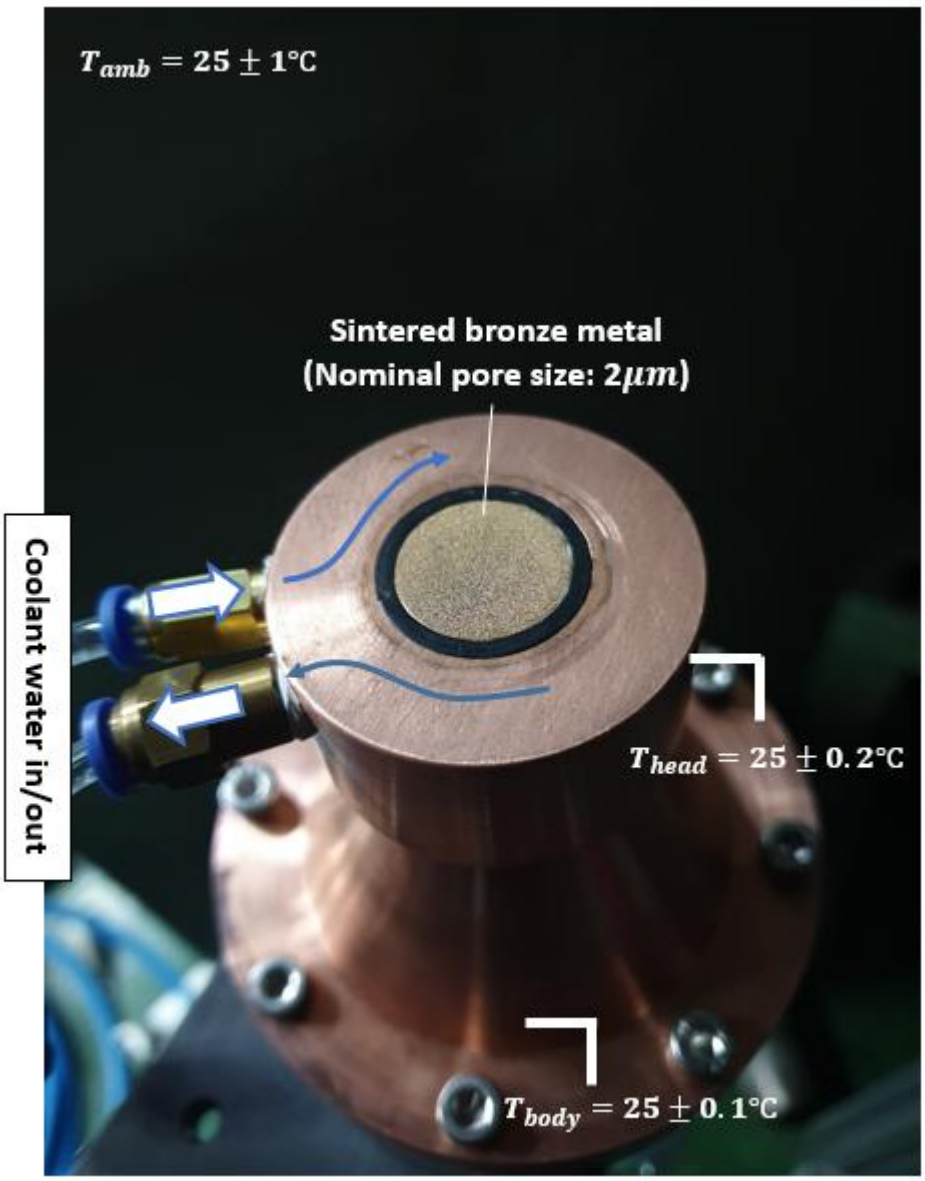

Figure 5.2 A close-up photograph of the burner head and sintered metal outlet.

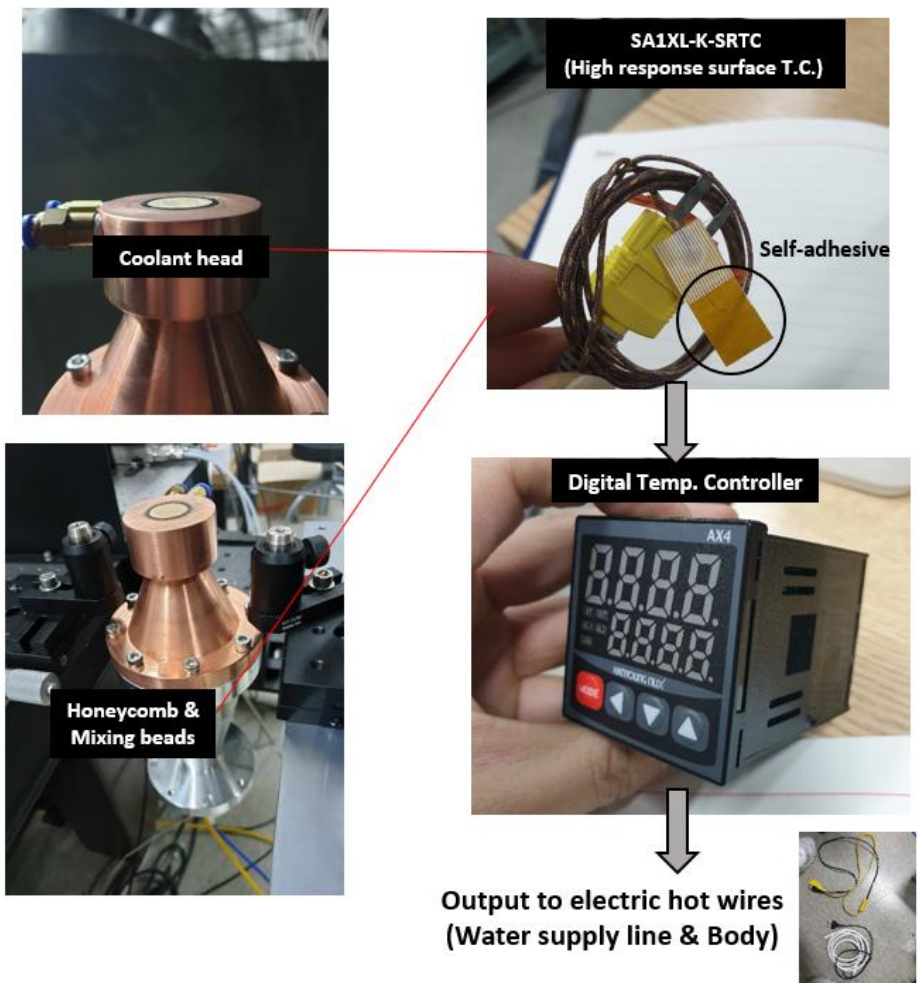

Figure 5.3 Photographs of experimental apparatus for feed-back loop control of burner temperature.

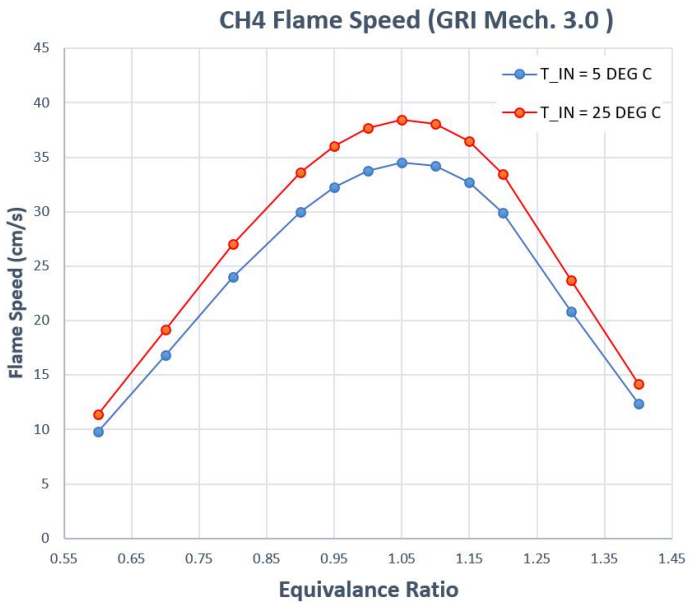

Figure 5.4 Theoretical flame speed vs. fuel concentration calculated using Chemkin Pro 19.2 numerical solver with GRI 3.0 reaction mechanism.

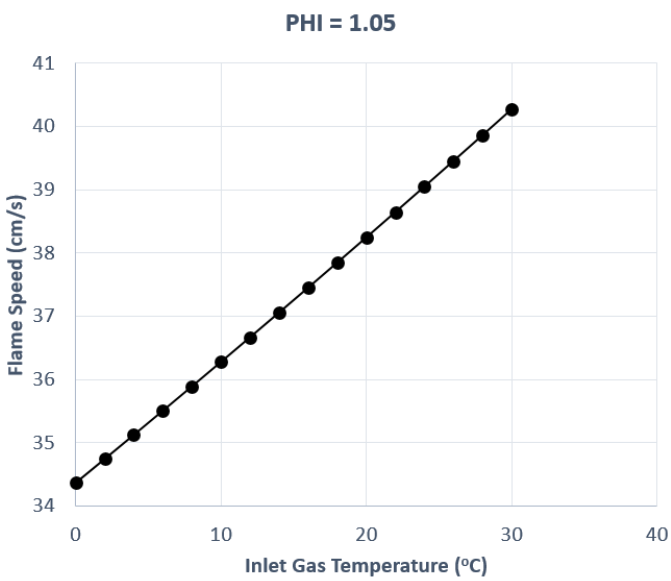

Figure 5.5 Theoretical flame speed calculated at different gas temperatures.

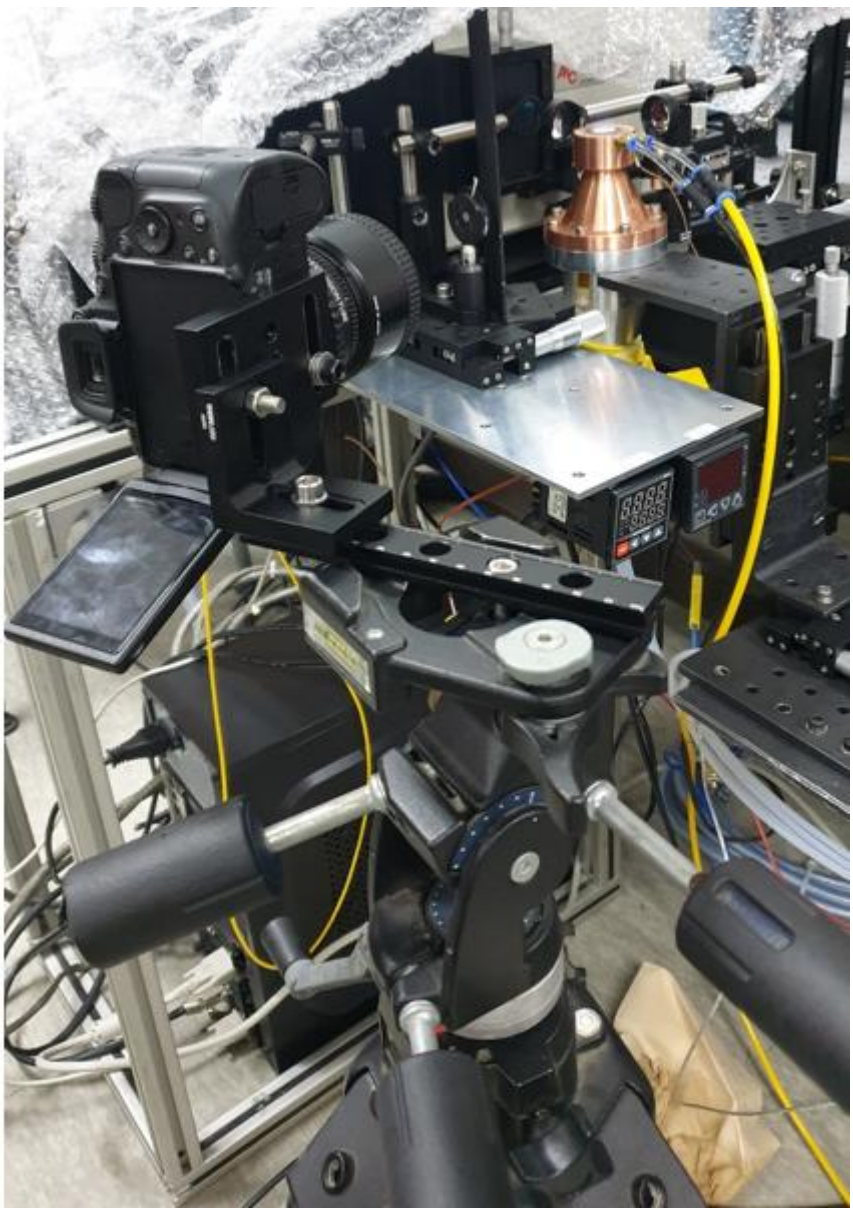

Figure 5.6 A photograph of experimental setup for flat-flame imaging.

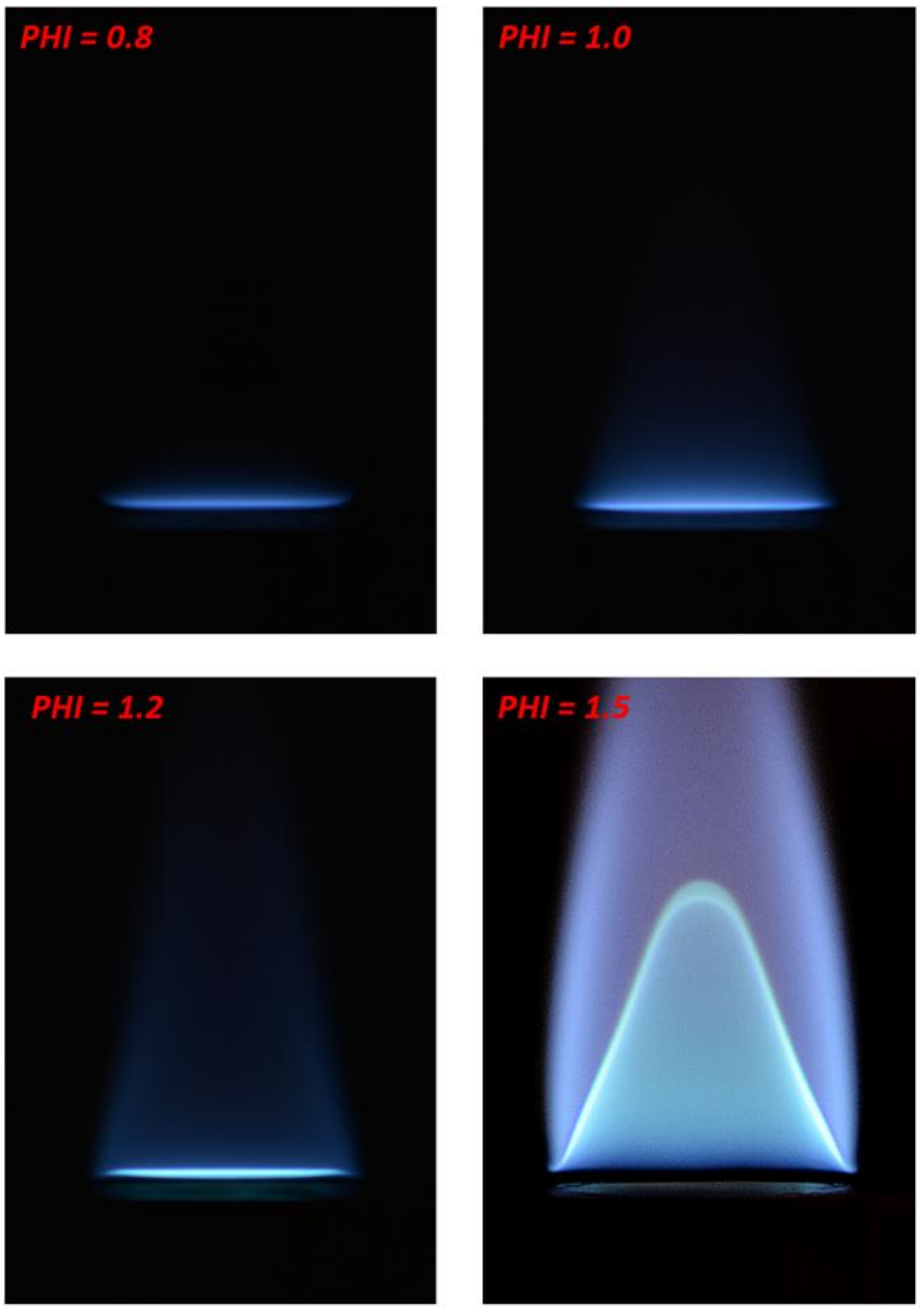

Figure 5.7 Photographs of the flat-flame operating at four different fuel concentrations ($\emptyset = 0.8, 1.0, 1.2, 1.5$).

5.2 Burner testing

5.2.1 Flame chemiluminescence

In order to verify the reliable burner operation in the premixed-mode, flame emission spectroscopy (FES) was employed to evaluate fuel concentration in the flat-flame burner. This method is highly simple and reliable, in that any external photon source is not required while keeping the measurement perfectly non-intrusive. Spectral band profiles of the intermediate molecules such as OH* (306.4 nm), CH* (431.5 nm), and C_2* (520 nm) are recorded and analyzed for various equivalence ratios ($0.72 < \emptyset < 1.25$). The importance of flame radiation, which is strong and reliable in the UV spectrum, is confirmed particularly for quantitative measurement purposes. (1) The theoretical principle and the application of flame radiation and (2) experimental results are introduced in the following sections.

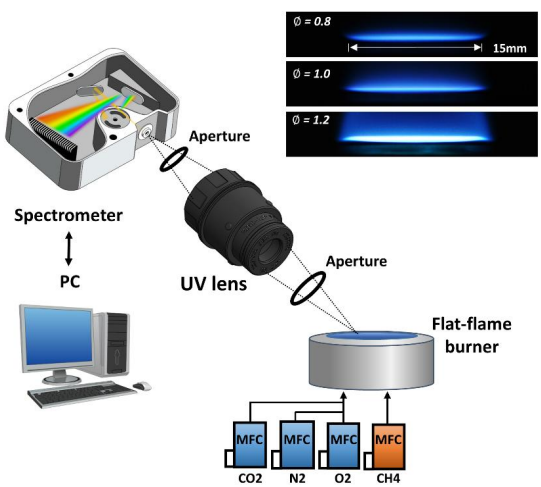

Figure 5.8 Schematic of the experimental setup for testing atmospheric flame chemiluminescence.

Reprinted with permission from [3] ©Elsevier.

When sufficient heat energy is released from the reaction zone, the flame radiation (chemiluminescence) is due to the spontaneous emission of excited intermediate and product species. For instance, electronically excited CH* emits photon energy at 387.2 and 431.5 nm, after collisional excitation and subsequent chemical reactions of $CH_2 + O \rightarrow CO + CH^*$ and $C_2H + O_2 \rightarrow CO_2 + CH^*$ [82]. In addition, quasi-continuum CO_2^* emission appears in a broad spectral range from ultra-violet (UV) to visible wavelengths [83, 84]. Therefore, the overall flame radiation is composed of both broadband CO_2^* emission and discretized molecular band spectra, where the position and strength of each line, band, and system are determined by the chemical kinetics associated with the hydrocarbon combustion reactions and interacting flow properties. This implies that the chemiluminescence contains useful information regarding the gas composition and flow properties such as density and temperature.

Figure 5.9 displays a typical chemiluminescence spectrum of the methane/air flat flame at $\emptyset = 1.1$, plotted in the wavelength range of 260 – 540 nm. The dark

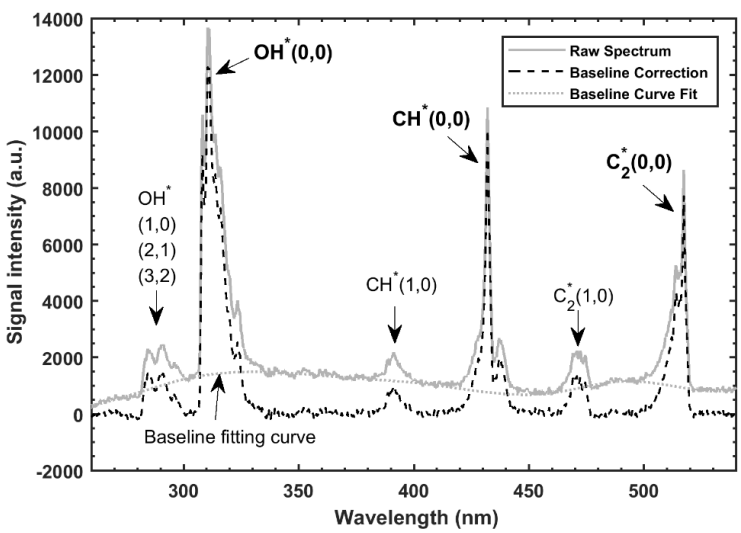

Figure 5.9 A typical flame chemiluminescence spectrum in 260 – 540 nm.

Reprinted with permission from [3] ©Elsevier.

noise is first subtracted, and then the underlying broadband continuum spectrum (dotted line) is additionally subtracted to obtain the baseline-corrected spectrum (dashed line). In Fig. 5.9, the radiation of the methane/air flame is characterized by several discernable molecular bands, with a relatively weak continuum contribution. The strong bands identified in the baseline-corrected spectrum are labeled with the quantum numbers describing the upper/lower state vibrational energy levels.

5.2.2 Operation at various fuel concentration

Figure 5.10 shows the time-averaged methane-air flame emission spectra at three different equivalence ratios (a) $\emptyset$ = 0.86 (adiabatic flame temperature T_{ad} = 2,080 K), (b) $\emptyset$ = 1.04 (T_{ad} = 2,230 K), and (c) $\emptyset$ = 1.20 (T_{ad} = 2,140 K). The uncertainty of $\emptyset$ from the instrumental uncertainty of the electro-mechanical flow controller used in this study is approximately ± 2.5 %, which corresponds to ± 15 K of the predicted flame temperature. The spectra in the wavelength range from 200 to 650 nm are recorded to monitor the influences of the $\emptyset$ variation. Each spectrum is normalized by the peak intensity of the OH* band near 310 nm, after the baseline correction. The $\emptyset$ at each condition is calculated based on the supply rates of methane (CH_4) and oxygen (O_2), which are accurately controlled by feedback-controlled MFCs.

The normalized spectral profile of the OH* band around 310 nm is not affected by the $\emptyset$ variation in this range, although measurements with higher spectral resolutions (e.g. 10 – 50 pm) could reveal subtle temperature effects [85]. On the contrary, significant changes of normalized CH* (432 nm) and C_2* (517 nm) emission bands are observed. It is found that the normalized emission band intensities of CH* and C_2* in the spectral range observed in this study (e.g., CH* bands at 387 and 432 nm, and C_2* bands at 472, 517, and 563 nm) are all monotonically increasing with the increase of $\emptyset$.

For the fuel-lean condition of $\emptyset = 0.86$, the CH* emission band at 432 nm can be seen, while the C_2* swan bands are not distinguishable. However, as $\emptyset$ increases above 1, the C2* bands grow significantly, and the CH* band becomes stronger as well. Thus, the CH* and C_2* bands dominate the spectra for the fuel-rich ($\emptyset > 1$) conditions. Based on this observation, it is evident that the normalized C_2* band intensity at 517 nm is the most sensitive to the $\emptyset$ variation in this spectral range.

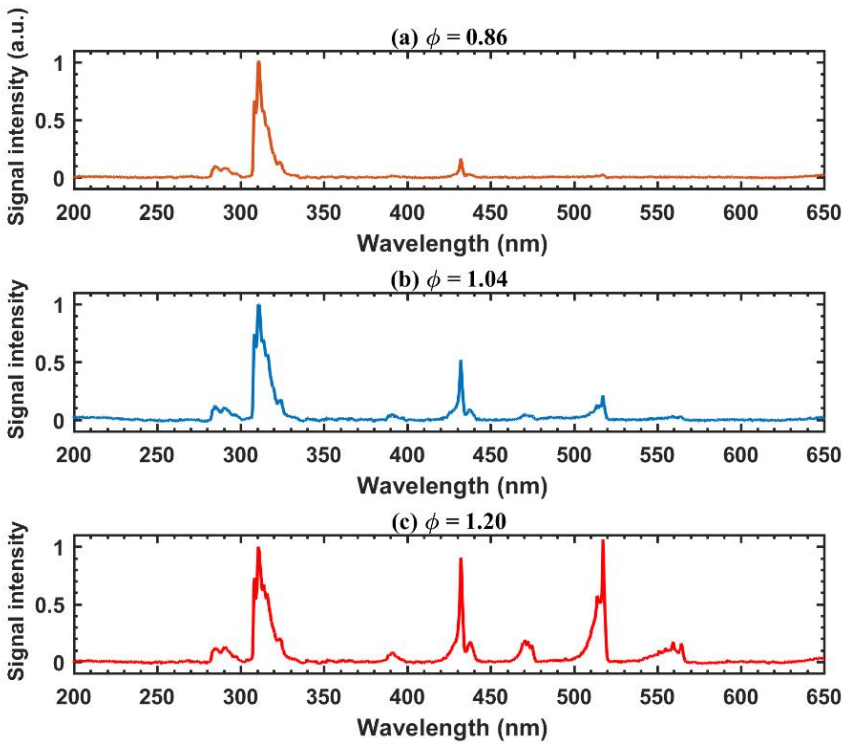

Figure 5.10 Normalized flat-flame chemiluminescence spectra with varying equivalence ratio ($\emptyset = 0.86, 1.04, 1.20$).

Reprinted with permission from [3] ©Elsevier.

It is noteworthy that the flame radiation in the UV wavelength range is strong, and therefore adequate for accurate quantification purposes. The UV emission bands of OH* have been witnessed in various previous studies [86, 87]. They are more reliable in comparison with some of the other bands selected in previous methane/air flame chemiluminescence research [85, 88]. The strong signal observed here is attributed to the high UV sensitivity of the photon collection system (> 70 % transmission at 220 – 400 nm) and UV optics used in this study.

The ratios of the emission band intensities of OH*, CH*, and C_2* are correlated with $\emptyset$. Either the band peak intensity or the integrated area under the band can be used to calculate the peak intensity ratio (PIR) and band intensity ratio (BIR), respectively. Figure 5.11(a) shows the PIR (square) and BIR (circle) of C_2* (517 nm) over CH* (432 nm), versus $\emptyset$ in the range of 0.78 (fuel-lean) to 1.23 (fuel-rich). Both the PIR and BIR show a similar trend, monotonically increasing with $\emptyset$. However, the BIR has some scatter which is likely due to integrated detector noise, and this increases the uncertainty of the calibration function. As observed previously in Fig. 5.10, the emission band intensities become more sensitive to $\emptyset$ at fuel-rich conditions ($\emptyset > 1$). In the range of $0.9 < \emptyset < 1.25$, the C_2*/CH* PIR is well fit to an exponential function of $\emptyset$ with $R^2 = 0.993$, which can be used as a high-sensitivity calibration curve in fuel-rich conditions while the C_2*/CH* PIR becomes nearly insensitive to $\emptyset$ in fuel-lean ($\emptyset < 1$) conditions. This is due to the fact that the signal-to-noise ratio (SNR) for the C_2* emission bands becomes small as $\emptyset$ is reduced for fuel-lean flames, as illustrated in Fig. 5.10(a).

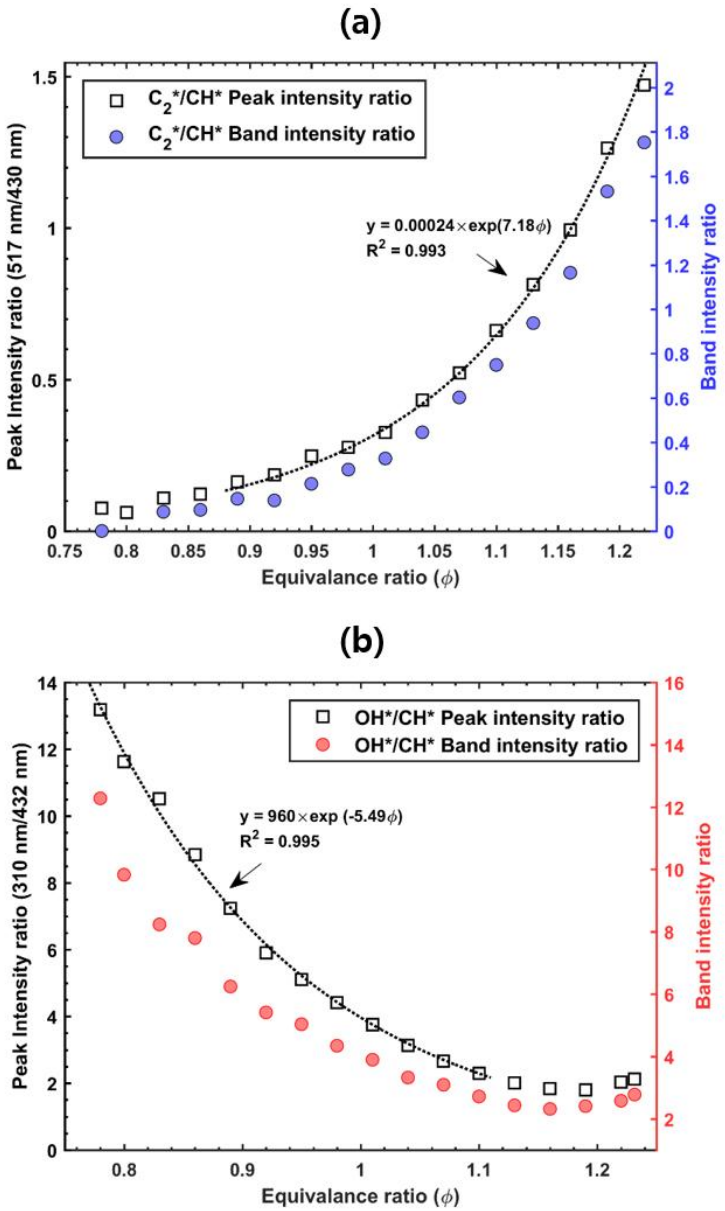

Figure 5.11 Molecular peak-intensity ratio (PIR) according to the fuel concentration.

Reprinted with permission from [3] ©Elsevier.

Figure 5.11(b) shows the correlation of the OH*/CH* PIR and BIR versus $\emptyset$, for the same experimental conditions as in Fig. 5.11(a). The strong OH* emission band located at 310 nm for the (0,0) $A^2\sum^+ - X^2\Pi$ system is used as the $\emptyset$ indicator, instead of the C_2* band. As opposed to the C_2*/CH* case, the OH*/CH* PIR and BIR decrease as $\emptyset$ increases, and the negative slope of the correlation is steeper for fuel-lean conditions. This implies that the OH*/CH* is a good indicator of $\emptyset$ when $\emptyset < 1$. However, this monotonic correlation breaks down at $\emptyset > 1.15$, and when $\emptyset < 0.75$ the CH* band (430 nm) emission intensity becomes too weak to be used as the denominator of the ratio. The correlation of the PIR versus $\emptyset$ in the range of $0.78 < \emptyset < 1.1$ is well-fitted to an exponential curve with a high determination coefficient of $R^2 = 0.995$.

Consequently, high-fidelity FES measurement of $\emptyset$ is enabled in the lean-to-rich flame conditions using the two PIRs of OH*/CH* at $0.75 < \emptyset < 1.1$ and C_2*/CH* at $0.9 < \emptyset < 1.25$, which covers most typical combustor operation conditions. Recall that the intense chemical reaction zones in non-premixed diffusion flames are always at near-stoichiometric conditions.

The effect of diluent concentration on the flame radiation is investigated with various N_2 concentrations in the oxidizer stream. Figure 5.12 shows the integrated intensities of the CH* band (432 nm) and the broadband (BB) emission, normalized by the OH* (310 nm) emission band integrated intensity, as functions of N_2 (or O_2) concentration in the oxidizer mixture (O_2 + N_2). The CH*/OH* BIR, which is essentially unaffected by the N_2 concentration, is multiplied by 25. The diluent mole fraction (X_{N2}) in the oxidizer stream is varied from 0.65 to 0.81, where $X_{N2} = 0.79$ is the reference condition of ambient air. The ratio of oxygen to fuel is unchanged ($\emptyset = 1$) at all data points shown in the figure. One of the major roles of diluent gas in flames is to store thermal energy while not actively participating in the chemical energy conversion process, i.e., the combustion chain reaction. Therefore, the flame temperature decreases as X_{N2} increases, and the flame propagation speed will decrease as well. In the range of $X_{N2} = 0.65 – 0.81$, kinetic simulations using GRI

3.0 mechanism yield flame temperature variation from T_{ad} = 2,640 K at X_{N2} = 0.65, down to T_{ad} = 2,070 K at X_{N2} = 0.81. Consequently, as X_{N2} increases while $\emptyset$ is kept constant at unity, the flame temperature and the concentrations (mole fractions) of fuel and oxygen in the reactant mixture decrease. This decelerates the production of intermediate species such as CH* and OH*.

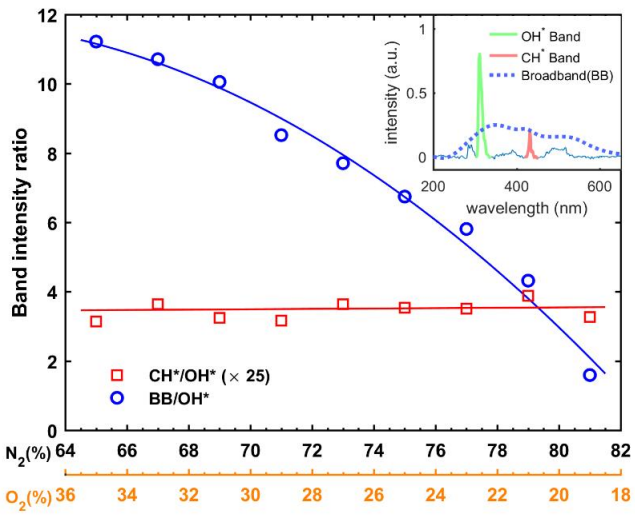

Figure 5.12 Broadband intensity correlation verifying stable control of diluent concentration.

Reprinted with permission from [3] ©Elsevier.

It is observed that the emission band intensities of CH* and OH* decrease as X_{N2} increases. The emission band intensities of the intermediate species can be expressed as the species concentration multiplied by the probability of spontaneous photon emission, i.e., $I_X^* = A_{21}[X^*]$, where the coefficient A_{21} is independent of temperature [82, 89, 90]. In general, the concentrations of the intermediate radical species (including CH* and OH*) in flames are assumed to be in a quasi-steady state. This is due to their slow production rate compared to the fast collisional quenching rate [82, 89]. Therefore, their concentrations are primarily determined by their

production rates. Since deceleration of the radical production lowers the radical concentration in a quasi-steady state, the emission strength would be weakened.

Interestingly, the CH*/OH* BIR is unaffected by the variation of X_{N2} in the range of 0.65 – 0.81, as shown in Fig. 5.12. Presumably, the production rates and concentration of CH* and OH* decrease simultaneously by the same amount with X_{N2}, such that the impact of X_{N2} is cancelled. This implies that the CH*/OH* BIR can potentially be used as a $\emptyset$ indicator, independent of the N_2 diluent concentration. In contrast, the BB/OH* BIR decreases significantly with diluent gas concentration. As previously mentioned, the BB emission mostly comes from CO_2* that is generated via

$$CO + O (+ M) \rightarrow CO_2^* (+ M) \qquad (5.1)\ [84, 91]$$

and photons are emitted by

$$CO_2^* \rightarrow CO_2 + h\nu \qquad (5.2)\ [83, 84]$$

where h and ν are the Planck constant and photon frequency, respectively, and M stands for the third-body collider molecule in flame. Lower X_{N2}, therefore, results in higher flame temperature, which would raise the concentration of radicals (e.g., H, O, and CO) in a steady-state. This in turn results in the acceleration of CO_2* formation, which enhances the BB emission intensity. This indicates that the BB emission intensity or the BB/OH* BIR can be correlated directly with the diluent concentration at a fixed $\emptyset$. Since the flame temperature is a function of $\emptyset$, the BB emission is also dependent on $\emptyset$.

In short, both $\emptyset$ and X_{N2} can be simultaneously measured by FES employing CH*/OH* BIR, an indicator of $\emptyset$ independent of X_{N2}, and BB/OH* BIR, an indicator of X_{N2} dependent on $\emptyset$.

5.3 Result & Discussion

5.3.1 Experimental result

To confirm the feasibility of the ps-LIBS technique developed in this study, quantitative fuel concentration measurements are conducted above an atmospheric flat-flame burner (Fig. 5.13) using the calibration result presented in Fig. 4.12. The custom-built burner could provide well-characterized, premixed, and laminar methane-air flows [92, 93] as described in section 5.1. The supply rates of high-purity dry air and methane are fixed at 2.875 ± 0.01 and 0.302 ± 0.003 SLPM, respectively, being accurately controlled by MFCs (Tylan, FC-280SAV) to minimize the uncertainty of the measurement target.

The steady-state concentration field above the burner is measured by the ps-LIBS (which does not initiate combustion) and compared to the ns-LIBS measurements (which initiates combustion with the first pulse of the entire measurement set). This is an exemplary experimental setup for the calibration purpose providing a steady, stable, and slow flow environment with known fuel concentration particularly near the center of the burner exit plane. The measurement result along the vertical axis of the burner is plotted against HAB (z) in Fig. 5.14; note that the y-axis is 'equivalent H-ratio ($\emptyset_{eq}$).

$$\emptyset_{eq}(x,z) = \frac{(\mathrm{H/N})_{x,z}}{(\mathrm{H/N})_{\emptyset=1}} \tag{5.3}$$

The H-ratio is defined as the ratio of the number of H atom to the number of N atom in the focal volume at the probing location, and the equivalent H-ratio ($\emptyset_{eq}$) is the H-ratio at the focus divided by the H-ratio at a stoichiometric methane-air condition.

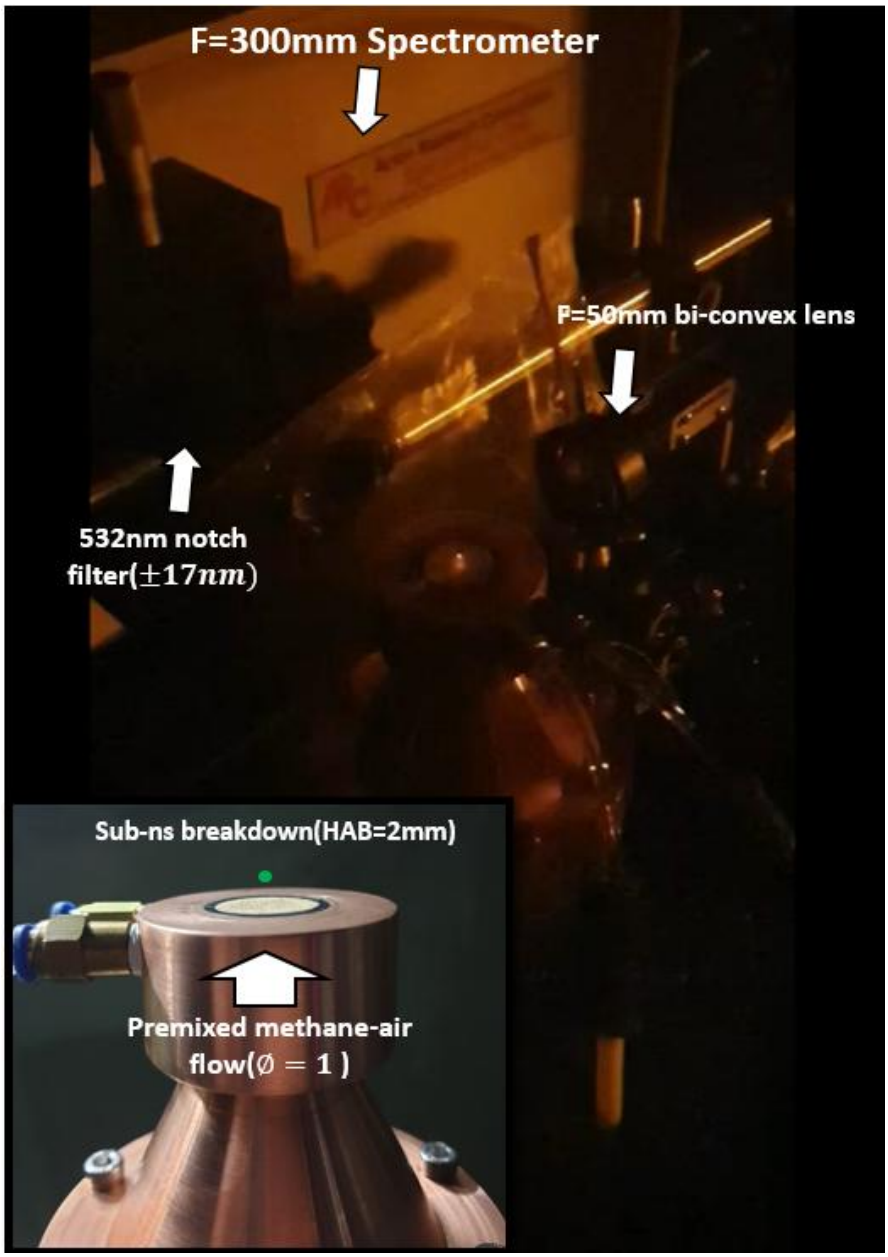

Figure 5.13 A photograph of the ps-LIBS setup. Inset illustrates the close-up image around the burner outlet.

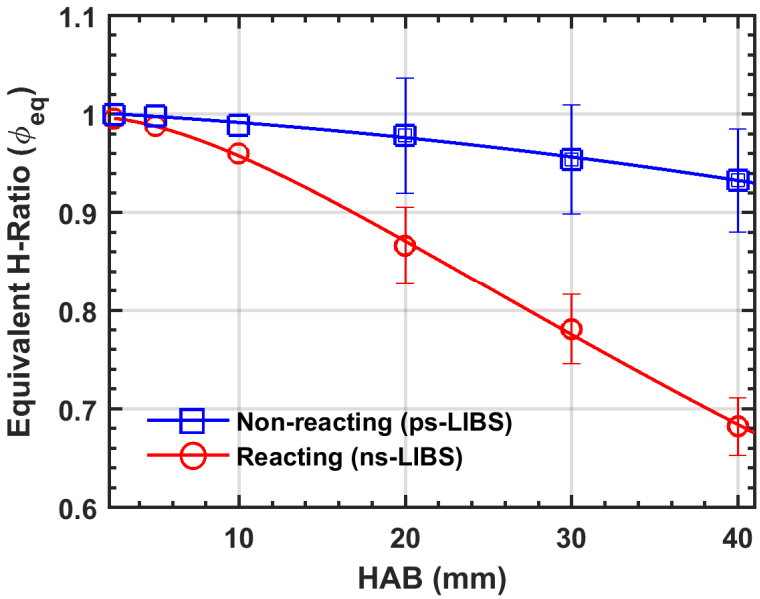

Figure 5.14 Axial fuel concentration distribution along the burner centerline.

Reprinted with permission from [2] ©Elsevier.

Thus, the $\emptyset_{eq}$ is same as the equivalence ratio ($\emptyset$) in unburned reactant mixtures; in combustion products, it is identical to the equivalence ratio of the reactant mixture to be burned to generate the combustion product. This $\emptyset_{eq}$ does not change with combustion reactions since the numbers of atoms do not change with chemical reactions. Ideally, for complete combustion of stoichiometric fuel-dry-air mixtures, H_2O is the only carrier of H atoms in combustion products, CH_4 is the only H containing species in reactants, and N_2, the sole carrier of N atom except for minor species, does not participate in combustion reactions. The blue curve in Fig. 8 shows the distribution of fuel concentration ($\emptyset_{eq}$) along the vertical axis measured using ps-LIBS (non-reacting flow), while the red curve shows the equivalent result at identical measurement locations but with ns excitation in the reacting flow ignited by the focused ns-pulses. In Fig. 5.14, the $\emptyset_{eq}$ decays much slower in comparison with the $\emptyset_{eq}$ with the flame. For example, the $\emptyset_{eq}$ at z = 40 mm is approximately

0.93 without a flame; with the flame, the $\emptyset_{eq}$ at the same location is about 0.68. The radial distribution of the fuel concentration measured using ps-LIBS is presented in Fig. 5.15.

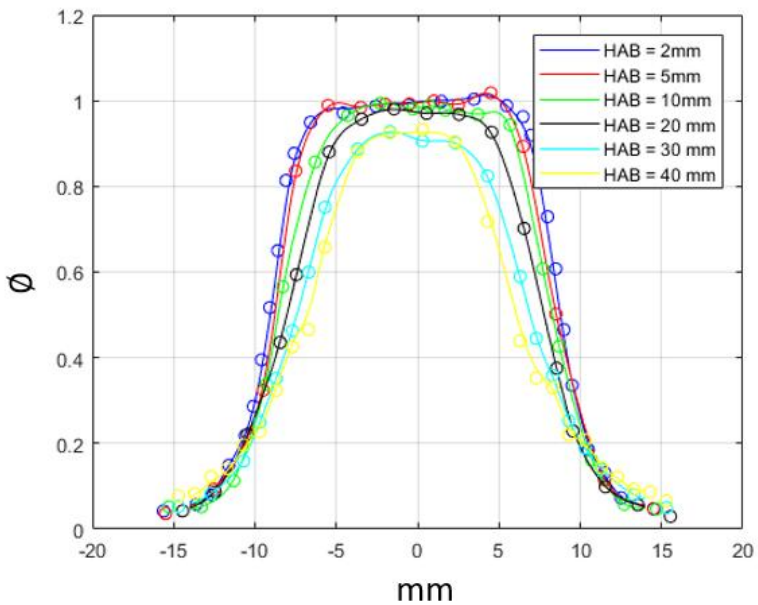

Figure 5.15 Radial fuel concentration distribution at different HAB.

Based on the multi-point (126 points) LIBS measurements above the flat-flame burner, time-averaged 2D fuel concentration ($\emptyset_{eq}$) fields are reconstructed without (ps-LIBS, Fig. 5.16(a)) and with (ns-LIBS, Fig. 5.16(b)) a flat flame stabilized at z = 1 mm. The color code in Fig. 5.16 indicates $\emptyset_{eq}$ in reactants (Fig. 5.16(a)) and combustion products (Fig. 5.16(b)); the H/N PIR extracted at each measurement location is converted to $\emptyset_{eq}$ using the calibration functions obtained in Fig. 7. In both the cases, the burner exit (z = 0 mm) velocity (U_{exit}) is fixed at 38.5 cm/s, and an identical premixed stoichiometric methane-air mixture is supplied. The differences between the two cases are evident in the $\emptyset_{eq}$ distributions (Fig. 5.16),

which primarily comes from the increased flow rate with the flat-flame present. The horizontal $\emptyset_{eq}$ distribution at z = 40 mm without a flame shown at the top of Fig. 5.16(a) is higher than that with the flat-flame (top of Fig. 5.16(b)) at all locations due to the air entrainment enhanced by the flame.

It should be emphasized that ns excitation ignites flammable mixtures and thus that ns-LIBS cannot characterize cold non-reacting flows of flammable mixtures, except with the first laser pulse (which is the only one with unreacted gas). Ps excitation, on the other hand, does not initiate combustion, and cold flammable flow fields can be probed as shown in Fig. 5.16(a). Fig. 5.16(a) confirms that there is a broad area of uniform fuel concentration ($\emptyset_{eq}$ =1) near the center of the burner exit plane. This implies that the fuel concentration in the center area is known, which can be determined by the upstream supply rates of the fuel and air; therefore, the burner is proper for calibration experiments of the ps-LIBS. The red-dashed line in Fig. 5.16(a) ($\emptyset_{eq} =$ 0.6 contour) delineates the ignition boundary for which a single ns-pulse will instantaneously ignite a flame to quickly switch the flow to be reacting as shown in Fig. 5.16(b).

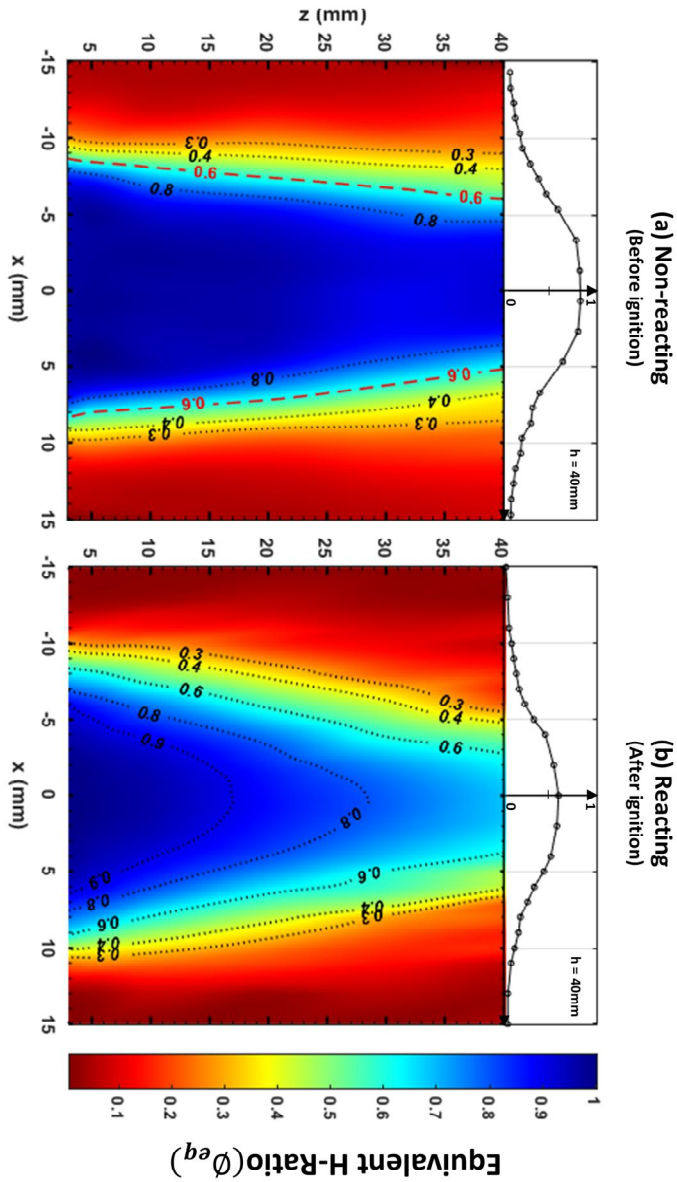

Figure 5.16 2-D Fuel concentration ($\emptyset$) distribution above the flat-flame burner measured by (a) ps-LIBS (no flame) and (b) ns-LIBS (flat-flame at z = 1 mm).

*Reprinted with permission from [2] ©**Elsevier.***

5.3.2 Comparison to conventional LIBS

Previously, there has not been a single study reporting successful LIBS measurements of equivalence ratio in flammable mixtures (reactants) without ignition using ns-pulses. As shown in section 4.3, flammable mixtures were always ignited with the ns-pulses (6-ns pulse-width from the standard, commercial Q-switched laser) when the pulse energy is above the breakdown threshold, which is the minimum pulse energy generating plasmas. In other words, this is the first study wherein cold flammable reactants were characterized using LIBS with an ns-laser source, which was enabled by a novel pulse modulation setup.

The LIBS diagnostic using focused ns-laser pulses cannot be used to measure the properties of flammable reactants. In this study, a novel methodology of laser-induced breakdown spectroscopy (LIBS) in flammable mixtures was proposed and demonstrated. LIBS requires the generation of laser-induced plasmas that often cause significant perturbations in the measurement target medium, e.g., chemical reactions, pressure waves, and rapid temperature rise. These perturbations are mostly induced by rapid photon energy absorption occurring in the plasma, referred to as the inverse-Bremsstrahlung (IB) process. In flammable mixtures, this gas heating may ignite the mixture, and in this respect the LIBS measurement is intrusive. Nevertheless, LIBS also requires strong plasma emission for quantitative measurements of mixture components. While the IB process can effectively raise the emission signal, it was shown that the IB process can be limited by reducing the laser pulse width. In this study, a variable air-pressure optical cell was used to chop the ns-duration laser pulses (from a typical Q-switched Nd:YAG ns-laser source) by first focusing the ns-pulse in the cell to create a breakdown. The pulse width of the laser beam transmitted through the cell is dependent on the cell pressure, and for this work, a pulse duration of approximately 600 ps was produced (with the cell at a pressure of 10 bar) and then employed for LIBS measurements. This chopped laser pulse created breakdown plasmas with sufficient emission signal (to enable concentration

measurements) but did not ignite flammable methane-air mixtures. The potential for cold-gas probing was then demonstrated with minimally intrusive measurements (i.e., not causing ignition) of equivalence ratio in a highly flammable methane-air flow.

Simply comparing the baseline intensity levels or the σ_{noise} in the ps-LIBS and ns-LIBS is difficult since they are more dependent on the time-delay and gate-width (exposure time) set to capture the emission spectra. For example, the baseline intensity level or the broadband emission strength of the ns-plasma is quite strong when the time-delay is short e.g., <100 ns; however, that becomes almost negligible if one sets the delay longer than several hundred ns. In other words, the broadband emission of the early stage ps-plasma could be even stronger than that of ns-plasma seen at a longer delay. The time-delay and gate-width are actually the choices of a researcher, and the optimal choice would strongly depend on the specific experimental conditions/constraints and properties of the measurement target medium. Therefore, particularly for measurement purposes, comparing the uncertainty levels of ns-LIBS and ps-LIBS without mentioning the choice of time-delay and gate-width would be difficult, and the choice does not need to be the same in both the cases, e.g., longer delay for ns-LIBS and shorter delay for ps-LIBS depending on the experimental conditions or longer gate-width for ps-LIBS.

The SNR of the N II 568 nm line and the H 656 nm line in a single-shot ps-LIBS spectrum are estimated to be approximately 250 and 30 – 800, respectively, in the range of the investigated equivalence ratio ($\emptyset = 0.1 - 1.5$). Employing the same definition of SNR, the SNR of an emission line in a single-shot ns-LIBS spectrum typically varies within 100 – 1200, which is mainly due to the stronger emission line intensity compared to that of ps-plasma.

The signal-to-noise ratio (SNR) of the N II peak centered at 567 nm and the H peak centered at 656 nm are evaluated, which were used for the quantification of the PIR throughout this study. Recall that the SNR is strongly dependent on the camera gate-delay and width, and the target gas conditions; in general, longer gate-width

provided better SNR in the current setup within the range tested in this study, and lower gas density reduced the SNR. Table 5.1 summarizes the measurement SNR at three different conditions and varied gate-width. To improve the SNR of the ps-LIBS, the gate width is elongated.

Table 5.1 Summary of LIBS performance (SNR) at different pulse conditions.

Laser Pulse	Gate width	SNR at $\emptyset = 0$ (567 nm N)	SNR at $\emptyset = 1$ (567 nm N)	SNR at $\emptyset = 1$ (656 nm H)
6 ns, 50 mJ	10 ns	550	15	100
6 ns, 120 mJ	10 ns	730	150	220
600 ps, 3 mJ	60 ns	250	250	470

5.3.3 Comparison to different laser diagnostics

Spontaneous Raman [44] and Rayleigh scattering [45, 46] can be alternatively used for non-reacting fuel concentration measurements. However, the major disadvantage of the two techniques, as compared with LIBS measurement, is the weak (~1/1000 of typical LIBS signals) output signal primarily due to the small scattering cross-sections. Thus, the optical signals can be obscured by unintended laser-induced fluorescence and even by flame chemiluminescence (which is well-depicted in Fig 5.9). Moreover, both techniques typically require high input laser pulse energy which often necessitates (1) spatial and (2) temporal beam shaping to prevent optical damage for beam delivery into the target flow. Furthermore, while Rayleigh scattering cross-sections are significantly higher than spontaneous Raman

scattering cross-sections, Rayleigh scattering is highly susceptible to stray scattering interferences from particles and surfaces, which can make its application challenging except to clean, dust-free, and idealized environments. One of the primary advantages of LIBS over Raman spectroscopy is the high SNR, which is particularly important in the presence of strong background combustion emission. The fluorescence from molecules in reactants such as CH_4 and H_2 in non-reacting conditions as well as the chemiluminescence from flames in reacting conditions can interfere with or obscure the output signal. To compensate for the low SNR, Raman scattering typically requires high laser pulse energy (300 - 2000 mJ). Therefore, when the measurement target is confined, optical access windows allowing the laser pulse injection into the measurement target medium can be damaged by the high-power laser pulses, and the measurement near the window (or wall) is quite difficult.

The experimental investigation in [45] reported fuel concentration measurements in a diesel spray using planar Rayleigh scattering. It was shown that the unwanted interference signals from Mie scattering and stray background are typically one or two orders of magnitude (x 10-100) stronger than the output signal. In addition, the influences of the reflection/absorption by optical access windows, and uncertainties from laser pulse energy variation and beam path steering are all non-negligible due to the weak output signal intensity. Filtered Rayleigh scattering (FRS) utilizing a high-power pulse laser source and an iodine filter was employed for fuel concentration measurements when the difference between the scattering cross-sections of the target fuel species and air is insignificant, e.g., in methane-air mixtures [48]. Mie scattering sand reflected/stray laser scatter are absorbed/blocked by the filter, and therefore the interfering background signal can be remarkably reduced. However, even when limiting its application to a zero-dimensional quantitative concentration measurement, FRS still has a much weaker output signal intensity in comparison with that of LIBS; therefore, the measurement uncertainty with FRS is inherently higher. Moreover, sophisticated controls over the laser source, which should be injection-seeded, and the iodine filter are essential in FRS (e.g., the

spectral width of the laser pulse and the wavelength range in where the filter blocks transmission should be precisely controlled within an extremely narrow range of several pico-meters). Preventing optical breakdown and window damages while keeping sufficiently high output signal strength is again another critical issue in implementing the FRS.

Alternatively, the ps-LIBS developed in this study requires only an optical pressure cell and a typical ns-pulsed laser, not an iodine filter nor an injection seeder. The ps-pulses of much lower pulse energy of approximately 3 mJ modulated by the pressure cell generates strong output emission signals of high SNR to be used for quantitative fuel concentration measurements. Due to the significantly reduced pulse energy requirement of the ps-LIBS compared to the Raman and Rayleigh methods, damage to optical access windows becomes much less probable. In addition, the fuel concentration measurements in both the reacting and non-reacting conditions are possible using the same setup, simply by switching the cell pressure. Recall that the atom concentration will be unchanged by the combustion reactions; however, the scattering cross-sections of molecular species change with chemical reactions. The single optical-access requirement is another important advantage of LIBS: the plasma emission signal can be collected through the optical access port used for the laser beam transmission. Finally, the shortest possible temporal resolution of the ps-LIBS is estimated to be 80 ns, and the smallest possible spatial resolution of the measurement is estimated to be 0.3 mm, which is comparable to the previously explored optical measurement methods. The high signal-to-noise ratio (SNR) of the ps-LIBS in comparison with other non-intrusive techniques is another critical benefit of the developed method. Due to the high SNR, the pulse energy used for this ps-LIBS is a small fraction (i.e., 1 – 5 %) of that used with Raman and Rayleigh scattering. The typical single-shot SNR is estimated to be 30 - 250. The minimum quantification limit (SNR $\approx$ 10) of the fuel concentration measurement is estimated to be $\emptyset = 0.03$ at the standard condition (P = 1 atm, T = 25 ℃).

5.4 Pressure effect on plasma dynamic

A schematic of the experimental setup is shown in Fig. 5.17. Linearly polarized 532nm Nd:YAG laser beam ($\tau = 6\ ns$) is focused using a plano-convex lens (f = 75 mm). The plasma is generated inside a stainless-steel pressure cell with four optically-accessible viewports. The cell pressure is stabilized between 1 – 10 bar being continuously vented with compressed air. Laser pulse energy is fixed at 65 mJ with 6 ns pulse width. A thermo-electrically cooled ICCD is gated at 2 ns for detecting morphological plasma emission structures.

To investigate the plasma behavior at high pressure, plasma continuum emission is imaged under a stabilized cell condition ranging from 1 to 10 bar at constant room temperature.

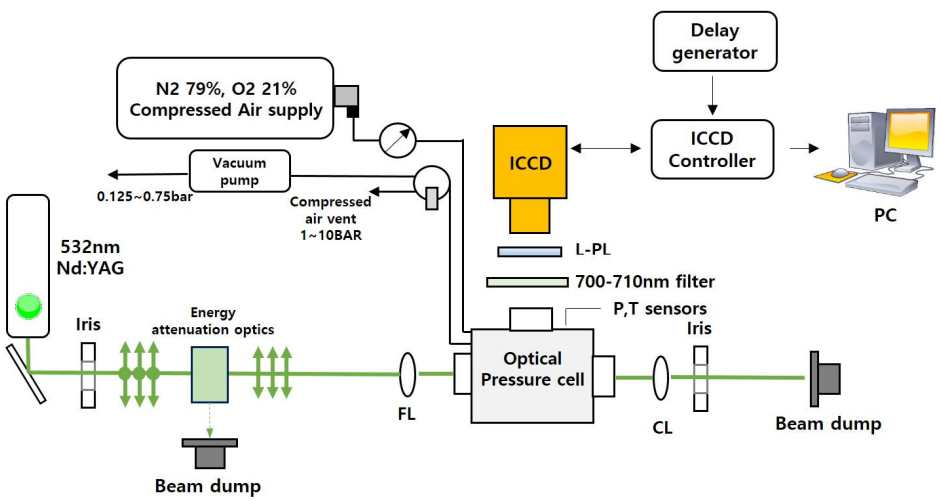

Figure 5.17 Experimental setup for capturing plasma emission at varied pressure.
CL, collimating lens; FL, focusing lens; PL: Polarizer

The images in Fig. 5.18 are taken with 2 ns gate width at 20 ns after the breakdown, ensemble-averaged over 50 individual shots. To avoid CCD damage, the plasma self-emission is spectrally filtered in 700 – 710 nm using a tunable bandpass filter located between the plasma and the camera lens. In the images, the laser beam is from the right to left and all spatial dimensions are given in mm.

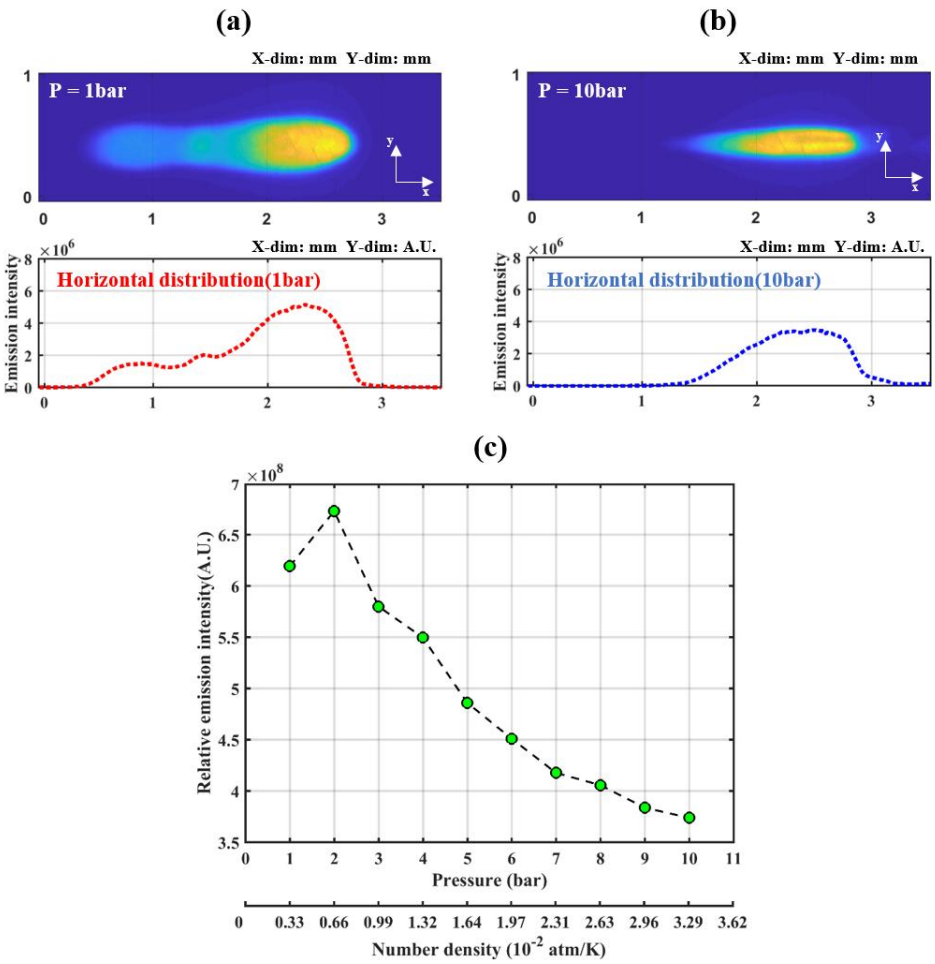

Figure 5.18 (a,b) Continuum emission structure at P = 1, 10 bar, (c) average radiation power profile with pressure variation.

In Figs. 5.18(a) and (b), the continuum emission structures at two different air pressures of 1 and 10 bar are shown. The graph underneath each image shows the emission intensity distribution along the horizontal direction (x) binned vertically. As illustrated in the figures, the plasma morphological structure depends strongly on pressure or density. The plasma at 1 bar in Fig. 5.18(a) is diffusely distributed in 0.5 – 2.8 mm horizontally on the x-axis with multiple peaks merged. On the other hand, the single-peak plasma emission at 10 bar is rather narrowly concentrated vertically and horizontally within 1.4 – 2.9 mm (Fig 5.18(b)). It is noteworthy that the plasma grows only toward upstream (from left to the right in the images) from the geometrical beam focus at elevated pressure conditions above 2 bar. Interestingly, the plasma at atmospheric pressure evolves with bi-directional core growth, i.e., expansion from the initial ignition spot to both the horizontal directions: stronger upstream and weaker downstream peaks appear in Fig. 5.18(a). (This aspect is referred to in section 3.2.1.) At sub-atmospheric pressure (0.1 – 1 bar) conditions, a previous study [53] reported a stronger downstream emission peak at lower pressure due to the decrease in plasma energy conversion rate. This implies that more of the laser pulse energy would be consumed upstream as the pressure or density increases.

The total emission intensity as a function of the ambient pressures is shown in Figure 5.18(c). The plasma radiation intensity decreases in general as the pressure increases above 2 bar while the radiation is stronger at 2 bar than that of 1 bar. This plasma radiation consists of photons from various excited species. In the spectrum of the radiation, pressure-broadened emission lines and persistent ion peaks are seen at elevated pressure conditions. Further analyses on the emission spectra reveal that the laser photon energy is more effectively deposited into the confined volume of plasma at higher pressure to get higher electron number density upstream where electrons absorb photon energy faster. Therefore, the decrease in total emission intensity at higher pressure does not mean less laser photon energy absorption. Presumably, the plasma emission at higher pressure is blocked via self-absorption within a highly heated and denser plasma core of smaller volume.

Chapter 6 Conclusion

Laser-induced plasmas emit photons containing useful information about the target gas property. Therefore, the plasmas have been widely utilized for measurement purposes, i.e., laser-induced breakdown spectroscopy (LIBS). The plasma generation by laser, referred to as the optical breakdown, requires sufficiently strong photon density at the laser focus. Due to the intense inverse-Bremsstrahlung (IB) photon absorption and gas heating, however, the dramatic increase of temperature and electron number density in breakdown plasma causes flow disturbances, e.g., shockwave. This implies that the LIBS will disturb and change the properties of the measurement medium. Therefore, the IB process should be limited for non-intrusive measurements using the laser-induced plasmas.

For the purpose of actively controlling laser pulse width impacting the strength of the IB process, high-power nanosecond laser pulses transmitted through focused-laser-induced plasmas were characterized. Nanosecond laser pulses (FWHM = 6ns at 532nm) were focused in a variable-pressure cell and chopped by the breakdown plasma to become shorter pulses. This is enabled by Inverse-Bremsstrahlung-dominant photon absorption (IBA), where electrons in the plasma quickly absorb and scatter the majority of the laser photons, whereas the gaseous medium at the focus is transparent before the IBA initiated. Therefore, the plasmas can be used as a 'virtual shutter', blocking or allowing the laser beam transmission.

The shutter 'closing time' determines the temporal width of the transmitted beam, and it was experimentally correlated with the gas density and laser pulse energy. This suggests that the FWHM of the transmitted pulses can be controlled by adjusting the cell pressure and pulse energy. In addition, it was found that saturable absorbers (SA) employed in conjunction with the pulse-chopping technique can further reduce the pulse width.

The temporal intensity profile of a typical ns-laser pulse (from a typical Q-switched Nd:YAG ns-laser source) was conveniently reshaped using the proposed method, and for this work, a pulse duration of approximately 600 ps was produced. The characteristics of laser-induced plasma were then controlled by focusing the modified laser pulses, and non-intrusive LIBS was enabled by selectively limiting the IB process depending on the target gas condition. In addition, the controlled plasma breakdown offered improved resolutions for the non-intrusive measurement in comparison to those of conventional LIBS measurement.

The novel methodology of laser-induced breakdown spectroscopy was demonstrated in flammable mixtures. While the IB process can effectively raise the emission signal, it was shown that the IB process can be limited by reducing the laser pulse width. This chopped laser pulse created breakdown plasmas with sufficient emission signal (to enable concentration measurements) but did not ignite flammable methane-air mixtures. The potential for cold-gas probing was demonstrated with minimally intrusive measurements (i.e., not causing ignition) of equivalence ratio in a highly flammable methane-air flow.

Bibliography

[1] S. Oh, S. Bae, C. D. Carter and H. Do, Laser pulse width control using inverse-Bremsstrahlung photon absorption, Optics Letters 44 (2019) 3721-3724.

[2] S. Oh, C. D. Carter, Y. Park, S. Bae and H. Do, Non-intrusive laser-induced breakdown spectroscopy in flammable mixtures via limiting inverse-bremsstrahlung photon absorption, Combustion and Flame 215 (2020) 259-268.

[3] S. Oh, Y. Park, G. Seon, W. Hwang and H. Do, Impacts of N2 and CO2 diluent gas composition on flame emission spectroscopy for fuel concentration measurements in flames, International Journal of Heat and Mass Transfer 149 (2020) 119174 - 119181.

[4] S. P. Kearney, R. W. Schefer, S. J. Beresh and T. W. Grasser, Temperature imaging in nonpremixed flames by joint filtered Rayleigh and Raman scattering, Applied Optics 44 (2005) 1548-1558.

[5] J. Kiefer, J. W. Tröger, T. Seeger, A. Leipertz, B. Li, Z. Li and M. Aldén, Laser-induced breakdown spectroscopy in gases using ungated detection in combination with polarization filtering and online background correction, Measurement Science and Technology 21 (2010) 1-7.

[6] V. Sturm and R. Noll, Laser-induced breakdown spectroscopy of gas mixtures of air, CO2,N2, and C3H8 for simultaneous C, H, O, and N measurement, Applied Optics 42 (2003) 6221-6225.

[7] S. Maurice, R. C. Wiens, M. Saccoccio, B. Barraclough, O. Gasnault*, et al.*, The ChemCam instrument suite on the Mars science laboratory (MSL) rover: science objectives and mast unit description, Space Science Reviews 170 (2012) 95-166.

[8] N. Melikechi, R. Wiens, H. Newsom and S. Maurice, Zapping Mars: Using lasers to determine the chemistry of the red planet, Optics & Photonics News 24 (2013) 26-33.

[9] F. Colao, S. Almaviva, L. Caneve, G. Maddaluno, T. Fornal, P. Gasior, M. Kubkowska and M. Rosinski, LIBS experiments for quantitative detection of retained fuel, Nuclear Materials and Energy 12 (2017) 133-138.

[10] B. Bhatt, K. Hudson Angeyo and A. Dehayem-Kamadjeu, LIBS development methodology for forensic nuclear materials analysis, Analytical Methods 10 (2018) 791-798.

[11] J. Kiefer, J. W. Tröger, Z. S. Li and M. Aldén, Laser-induced plasma in methane and dimethyl ether for flame ignition and combustion diagnostics, Applied Physics B 103 (2010) 229-236.

[12] F. Ferioli and S. Buckley, Measurements of hydrocarbons using laser-induced breakdown spectroscopy, Combustion and Flame 144 (2006) 435-447.

[13] M. Kotzagianni, R. Yuan, E. Mastorakos and S. Couris, Laser-induced breakdown spectroscopy measurements of mean mixture fraction in turbulent methane flames with a novel calibration scheme, Combustion and Flame 167 (2016) 72-85.

[14] M. Kotzagianni and S. Couris, Femtosecond laser induced breakdown for combustion diagnostics, Applied Physics Letters 100 (2012) 264104-264104-4.

[15] L. G. Blevins, C. R. Shaddix, S. M. Sickafoose and P. M. Walsh, Laser-induced breakdown spectroscopy at high temperatures in industrial boilers and furnaces, Applied Optics 42 (2003) 6107-6118.

[16] M. Noda, Y. Deguchi, S. Iwasaki and N. Yoshikawa, Detection of carbon content in a high-temperature and highpressure environment using laser-induced breakdown spectroscopy, Spectrochimica Acta Part B: Atomic Spectroscopy 57 (2002) 701–709.

[17] S. Joshi, D. B. Olsen, C. Dumitrescu, P. V. Puzinauskas and A. P. Yalin, Laser-induced breakdown spectroscopy for in-cylinder equivalence ratio measurements in laser-ignited natural gas engines, Applied spectroscopy 63 (2009) 549-554.

[18] M. Buschbeck, F. Büchler, T. Halfmann and S. Arndt, Laser-induced breakdown spectroscopy for lambda quantification in a direct-injection engine, Spectrochimica Acta Part B: Atomic Spectroscopy 74-75 (2012) 103-108.

[19] L. Zimmer, K. Okai and Y. Kurosawa, Combined laser induced ignition and plasma spectroscopy: Fundamentals and application to a hydrogen–air combustor, Spectrochimica Acta Part B: Atomic Spectroscopy 62 (2007) 1484-1495.

[20] H. Do, C. D. Carter, Q. Liu, T. M. Ombrello, S. Hammack, T. Lee and K.-Y. Hsu, Simultaneous gas density and fuel concentration measurements in a supersonic combustor using laser induced breakdown, Proceedings of the Combustion Institute 35 (2015) 2155-2162.

[21] C. Barnett, E. Cahoon and J. R. Almirall, Wavelength dependence on the elemental analysis of glass by Laser Induced Breakdown Spectroscopy, Spectrochimica Acta Part B: Atomic Spectroscopy 63 (2008) 1016–1023.

[22] L. St-Onge, V. Detalle and M. Sabsabi, Enhanced laser-induced breakdown spectroscopy using the combination of fourth-harmonic and fundamental Nd:YAG laser pulses, Spectrochimica Acta Part B: Atomic Spectroscopy 57 (2002) 121–135.

[23] T. X. Phuoc, Laser spark ignition: experimental determination of laser-induced breakdown thresholds of combustion gases, Optics Communications 175 (2000) 419–423.

[24] H. Do and C. Carter, Hydrocarbon fuel concentration measurement in reacting flows using short-gated emission spectra of laser induced plasma, Combustion and Flame 160 (2013) 601-609.

[25] P. S. Hsu, M. Gragston, Y. Wu, Z. Zhang, A. K. Patnaik, J. Kiefer, S. Roy and J. R. Gord, Sensitivity, stability, and precision of quantitative Ns-LIBS-based fuel-air-ratio measurements for methane-air flames at 1-11 bar, Applied Optics 55 (2016) 8042-8048.

[26] T. A. Labutin, V. N. Lednev, A. A. Ilyin and A. M. Popov, Femtosecond laser-induced breakdown spectroscopy, Journal of Analytical Atomic Spectrometry 31 (2016) 90-118.

[27] A. K. Patnaik, P. S. Hsu, Y. Wu, M. Gragston, Z. Zhang, J. R. Gord and S. Roy, Ultrafast laser-induced-breakdown spectroscopy (LIBS) for F/A-ratio measurement of hydrocarbon flames, 2018 AIAA Aerospace Sciences Meeting, 1-5

[28] A. Talebpour, M. Abdel-Fattah, A. D. Bandrauk and S. L. Chin, Spectroscopy of the gases interacting with intense femtosecond laser pulses, Laser Physics 11 (2001) 68–76.

[29] H. L. Xu, A. Azarm, J. Bernhardt, Y. Kamali and S. L. Chin, The mechanism of nitrogen fluorescence inside a femtosecond laser filament in air, Chemical Physics 360 (2009) 171-175.

[30] F. Martin, R. Mawassi, F. Vidal, I. Gallimberti, D. Comtois, H. P. Pin, J. C. Kieffer and H. P. Mercure, Spectroscopic study of ultrashort pulse laser-breakdown plasmas in air, Applied spectroscopy 56 (2002) 1444 - 1452.

[31] S. L. Chin, T. J. Wang, C. Marceau, J. Wu, J. S. Liu*, et al.*, Advances in intense femtosecond laser filamentation in air, Laser Physics 22 (2011) 1-53.

[32] Z. Z. Wang, Y. Deguchi, M. Kuwahara, J. J. Yan and J. P. Liu, Enhancement of laser-induced breakdown spectroscopy (LIBS) Detection limit using a low-pressure and short-pulse laser-induced plasma process, Applied spectroscopy 67 (2013) 1242-1251.

[33] J. Noack and A. Vogel, Laser-induced plasma formation in water at nanosecond to femtosecond time scales: calculation of thresholds,

absorption coefficients, and energy density, IEEE Journal Of Quantum Electronics 35 (1999) 1156-1167.

[34] H. Li, W. Chu, H. Xu, Y. Cheng, S. L. Chin, K. Yamanouchi and H. B. Sun, Simultaneous identification of multi-combustion-intermediates of alkanol-air flames by femtosecond filament excitation for combustion sensing, Scientific Reports 6 (2016) 1-7.

[35] N. G. Glumac, G. S. Elliott and M. Boguszko, Temporal and spatial evolution of a laser spark in air, AIAA Journal 43 (2005) 1984-1994.

[36] Z. Zhang, T. Li and S. Huang, Influence of the pressure and temperature on LIBS for gas concentration measurements, Spectrochimica Acta Part B: Atomic Spectroscopy 155 (2019) 24-33.

[37] L. Suneetha, P. Randive and K. M. Pandey, Numerical investigation on mixing behavior of fuels inreacting and non-reacting flow condition of a cavity-strut based scramjet combustor, International Journal of Hydrogen Energy 44 (2019) 16718-16734.

[38] M. Karaca, N. Lardjane and I. Fedioun, Implicit Large Eddy Simulation of high-speed non-reacting and reacting air/H2 jets with a 5th order WENO scheme, Computers & Fluids 62 (2012) 25-44.

[39] S. De, K. N. Lakshmisha and R. W. Bilger, Modeling of nonreacting and reacting turbulent spray jets using a fully stochastic separated flow approach, Combustion and Flame 158 (2011) 1992-2008.

[40] M. S. Mansour, A. M. Elbaz, W. L. Roberts, M. S. Senosy, M. F. Zayed, M. Juddoo and A. R. Masri, Effect of the mixing fields on the stability and structure of turbulent partially premixed flames in a concentric flow conical nozzle burner, Combustion and Flame 175 (2017) 180-200.

[41] A. Sengissen, J. Vankampen, R. Huls, G. Stoffels, J. Kok and T. Poinsot, LES and experimental studies of cold and reacting flow in a swirled partially premixed burner with and without fuel modulation, Combustion and Flame 150 (2007) 40-53.

[42] L. W. Kostiuk, K. N. C. Bray and R. K. Cheng, Experimental study of premixed turbulent combustion in opposed streams. Part I-Nonreacting flow field, Combustion and Flame 92 (1993) 377-395.

[43] Z. S. Li, M. Rupinski, J. Zetterberg and M. Aldén, Mid-infrared PS and LIF detection of CH4 and C2H6 in cold flows and flames at atmospheric pressure, Proceedings of the Combustion Institute 30 (2005) 1629-1636.

[44] G. Magnotti, U. Kc, P. L. Varghese and R. S. Barlow, Raman spectra of methane, ethylene, ethane, dimethyl ether, formaldehyde and propane for combustion applications, Journal of Quantitative Spectroscopy and Radiative Transfer 163 (2015) 80-101.

[45] C. Espey, J. E. Dec, T. A. Litzinger and D. A. Santavicca, Planar laser Rayleigh scattering for quantitative vapor-fuel imaging in a diesel jet, Combustion and Flame 109 (1997) 65-86.

[46] J. Fielding, J. H. Frank, S. A. Kaiser, M. D. Smooke and M. B. Long, Polarized/Depolarized Rayleigh scattering for determining fuel concentrations in flames, Proceedings of the Combustion Institute 29 (2002) 2703–2709.

[47] Y. Krishna, A. M. Elbaz, Y. Yue and G. Magnotti, Mole fraction measurement through a transparent quarl burner using filtered Rayleigh scattering, Applied Optics 58 (2019) 5575-5586.

[48] J. A. Sutton and J. F. Driscoll, Rayleigh scattering cross sections of combustion species at 266, 355, and 532 nm for thermometry applications, Optics Letters 29 (2004) 2620-2622

[49] M. Thiyagarajan and S. Thompson, Optical breakdown threshold investigation of 1064 nm laser induced air plasmas, Journal of Applied Physics 111 (2012) 073302 - 073310.

[50] J. Stricker and J. G. Parker, Experimental investigation of electrical breakdown in nitrogen and oxygen induced by focused laser radiation at 1.064 μ, Journal of Applied Physics 53 (1982) 851-855.

[51] G. V. Ostrovskaya and A. N. Zaidel, Laser spark in gases, Soviet Physics Uspekhi 16 (1973) 834-855.

[52] V. Bulatov, L. Xu and I. Schechter, Spectroscopic Imaging of Laser-Induced Plasma, Analytical Chemistry 68 (1996) 2966–2973.

[53] N. Glumac and G. Elliott, The effect of ambient pressure on laser-induced plasmas in air, Optics and Lasers in Engineering 45 (2007) 27-35.

[54] F. W. Perkins and E. J. Valeo, Thermal Self-Focusing of Electromagnetic Waves in Plasmas, Physical Review Letters 32 (1974) 1234-1237.

[55] A. K. Patnaik, Y. Wu, P. S. Hsu, M. Gragston, Z. Zhang, J. R. Gord and S. Roy, Simultaneous LIBS signal and plasma density measurement for quantitative insight into signal instability at elevated pressure, Optics Express 26 (2018) 25750-25760

[56] L. J. Radziemski and D. A. Cremers, Laser-induced plasmas and applications, Marcel Dekker, New York, 1989

[57] G. M. Weyl, Ionisation path formation in gases using a laser with retractable focus, Journal of Physics D: Applied Physics 12 (1979) 33-49.

[58] D. I. Rosen and G. Weyl, Laser-induced breakdown in nitrogen and the rare gases at 0.53 and 0.357μm, Journal of Physics D: Applied Physics 20 (1987) 1264-1276.

[59] C. G. Morgan, Laser-induced breakdown of gases, Reports on Progress in Physics 38 (1975) 621-665.

[60] C. Feng, X. Xu and J. C. Diels, High-energy sub-phonon lifetime pulse compression by stimulated Brillouin scattering in liquids, Optics Express 25 (2017) 12421-12434.

[61] J. Norin, Development of a Laser-Pulse Compression Device based on Stimulated Brillouin Scattering, M.S. thesis, Lund University, 1998.

[62] Z. Bai, Y. Wang, Z. Lu, H. Yuan, Z. Zheng, *et al.*, High Compact, High Quality Single Longitudinal Mode Hundred Picoseconds Laser Based on

Stimulated Brillouin Scattering Pulse Compression, Applied Sciences 6 (2016) 1-8.

[63] Y. Kalisky, A. B.-A. Baranga, Y. Shimony and M. R. Kokta, Cr 4+ doped garnets: novel laser materials and non-linear saturable absorbers, Optical Materials 8 (1997) 129-134.

[64] K. Han, S. Oh, H. Do and W. Hwang, The effect of laser-induced breakdown on particle dispersion, 73rd Annual Meeting of the APS Division of Fluid Dynamics, 1

[65] B. Pokrzywka, A. Mendys, K. Dzierżęga, M. Grabiec and S. Pellerin, Laser light scattering in a laser-induced argon plasma: Investigations of the shock wave, Spectrochimica Acta Part B: Atomic Spectroscopy 74-75 (2012) 24-30.

[66] H. Yin, Z. Hou, T. Yuan, Z. Wang, W. Ni and Z. Li, Application of spatial confinement for gas analysis using laser-induced breakdown spectroscopy to improve signal stability, Journal of Analytical Atomic Spectrometry 30 (2015) 922-928.

[67] K. Dzierże¸Ęga, A. Mendys and B. Pokrzywka, What can we learn about laser-induced plasmas from Thomson scattering experiments, Spectrochimica Acta Part B: Atomic Spectroscopy 98 (2014) 76-86.

[68] Y. B. Zel'dovich and Y. P. Raizer, Physics of Shock Waves and High-Temperature Hydrodynamic Phenomena, Academic Press, Cambridge, Massachusetts, 1967

[69] H. R. Griem, Validity of Local Thermal Equilibrium in Plasma Spectroscopy, Physical Review 131 (1963) 1170-1176.

[70] S. Zhang, X. Wang, M. He, Y. Jiang, B. Zhang, W. Hang and B. Huang, Laser-induced plasma temperature, Spectrochimica Acta Part B: Atomic Spectroscopy 97 (2014) 13-33.

[71] S. Joshi, H. El-Rabii, C. Dumitrescu, P. Puzinauskas and A. P. Yalin, Temperature and Electron Density Measurements of Laser-Induced Plasmas in Air at Elevated Pressures, Spectroscopy Letters 44 (2011) 103-112.

[72] K. Kobayashi, M. S. Bak, H. Tanaka, C. Carter and H. Do, Laser-induced breakdown emission in hydrocarbon fuel mixtures, Journal of Physics D: Applied Physics 49 (2016) 155201 - 155208.

[73] G. J. Bastiaans and R. A. Mangold, The Calculation of Electron-Density and Temperature in Ar Spectroscopic Plasmas from Continuum and Line Spectra, Spectrochimica Acta Part B: Atomic Spectroscopy 40 (1985) 885-892.

[74] H. R. Griem, Principles of Plasma Spectroscopy, Cambridge University Press, Cambridge, England, 1997

[75] E. Oks, Stark Broadening of Hydrogen and Hydrogenlike Spectral Lines in Plasmas, Alpha Science International, Ltd., Oxford, UK, 2006

[76] A. Skramida, Y. Ralchenko, J. Reader and NIST ASD Team (2020). NIST Atomic Spectra Database (ver. 5.2), Available: https://physics.nist.gov/asd [Sun Dec 20 2020]. National Institute of Standards and Technology, Gaithersburg, MD.

[77] H. Kopecek, H. Maier, G. Reider, F. Winter and E. Wintner, Laser ignition of methane–air mixtures at high pressures, Experimental Thermal and Fluid Science 27 (2003) 499-503.

[78] E. H. Lim, A. Mcllory, P. D. Ronney and J. A. Syage, Detailed Characterization of Minimum ignition Energies of Combustible Gases Using Laser Ignition Sources, in: S. H. Chan (Ed), Transport Phenomena in combustion, Taylor & Francis, New York, 1996, pp. 176-184.

[79] H.-Y. Moon, B. W. Smith and N. Omenetto, Temporal behavior of line-to-continuum ratios and ion fractions as a means of assessing thermodynamic equilibrium in laser-induced breakdown spectroscopy, Chemical Physics 398 (2012) 221-227.

[80] C. J. Kliewer, High-spatial-resolution one-dimensional rotational coherent anti-Stokes Raman spectroscopy imaging using counterpropagating beams, Optics Letters 37 (2012) 229-231.

[81] M. C. Escoda and M. B. Long, Rayleigh scattering measurements of the gas concentration field in turbulent jets, AIAA Journal 21 (1983) 81-84.

[82] V. N. Nori and J. M. Seitzman, CH* chemiluminescence modeling for combustion diagnostics, Proceedings of the Combustion Institute 32 (2009) 895-903.

[83] M. Slack and A. Grillo, High Temperature Rate Coefficient Measurements of CO + O Chemiluminescence, Combustion and Flame 59 (1985) 89-196.

[84] M. Kopp, M. Brower, O. Mathieu, E. Petersen and F. Güthe, CO2* chemiluminescence study at low and elevated pressures, Applied Physics B: Lasers and Optics 107 (2012) 529-538.

[85] T. S. Cheng, Y.-Y. Cheng, Y.-C. Chao, Y.-H. Li and C.-Y. Wu, Development of Chemiluminescence Sensor for Equivalence Ratio and Temperature Measurements in Turbulent Hydrocarbon Flames, International Colloquium on the Dynamics of Explosions and Reactive Systems, 1-4

[86] Y. Ikeda, J. Kojima and H. Hashimoto, Local Chemiluminescence Spectra Measurements in a High-pressure Laminar Methane/air Premixed Flame, Proceedings of the Combustion Institute 29 (2002) 1495–1501.

[87] T. M. Muruganandam, B. H. Kim, M. R. Morrell, V. Nori, M. Patel, B. W. Romig and J. M. Seitzman, Optical equivalence ratio sensors for gas turbine combustors, Proceedings of the Combustion Institute 30 (2005) 1601-1609.

[88] J. Kojima, Y. Ikeda and T. Nakajima, Spatially Resolved Measurement of OH*, CH*, and C2* Chemiluminescence in the Reaction Zone of Laminar Methane/air Premixed Flames, Proceedings of the Combustion Institute 28 (2000) 1757–1764.

[89] M. Tamura, P. A. Berg, J. E. Harrington, J. Luque, J. B. Jeffries, G. P. Smith and D. R. Crosley, Collisional Quenching of CH(A), OH(A), and NO(A) in

Low Pressure Hydrocarbon Flames, Combustion and Flame 114 (1998) 502-514.

[90] J. Kojima, Y. Ikeda and T. Nakajima, Basic Aspects of OH(A), CH(A), and C2(d) Chemiluminescence in the Reaction Zone of Laminar Methane–air Premixed Flames, Combustion and Flame 140 (2005) 34-45.

[91] G. Zizak, Flame Emission Spectroscopy: Fundamentals and Applications, ICS Training Course on Laser Diagnostics of Combustion Processes, 1-29

[92] M. A. Gregor and A. Dreizler, A quasi-adiabatic laminar flat flame burner for high temperature calibration, Measurement Science and Technology 20 (2009) 1-7.

[93] G. Hartung, J. Hult and C. F. Kaminski, A flat flame burner for the calibration of laser thermometry techniques, Measurement Science and Technology 17 (2006) 2485-2493.

국 문 초 록

레이저 유도 플라스마 분광법(LIBS)은 나노초(ns) 시간 범위에서 유체의 밀도 및 화학적 구성 정보를 측정하는 광학 유동 계측 방법이다. LIBS의 계측 신호는 측정 지점에서 레이저 광분해로 생성된 고온 플라스마의 자가 빛 방출을 기반으로 한다. 플라스마를 생성하기 위한 중성 유전체 가스의 광분해는 광자-분자, 광자-전자 및 전자-분자 간의 상호작용을 거쳐 이루어진다. 특정 시점부터 전자는 역제동(inverse-Bremsstrahlung) 메커니즘을 통해 플라스마 에너지 흡수를 증폭시키지만, 계측 대상 유동에 간섭을 피하기 위해서는 해당하는 역제동 광흡수의 시점과 강도가 적절히 제한되어야 한다. 본 연구에서는 이러한 광자-물질 상호작용을 제어하는 새로운 기법을 개발하여 유동 간섭을 최소화하는 LIBS 기술에 응용한다.

역제동 광흡수 효과는 레이저 펄스 폭과 밀접한 상관관계가 있지만, 일반적인 고출력 레이저의 펄스 폭은 가변적이지 않다. 나노초 레이저 펄스는 가스에 집광 시 과도한 역제동 효과를 수반하여, 유동에 원치 않는 간섭(충격파 등)을 일으키기도 한다. 이를 해결하고자 본 연구에서는 나노초 레이저 펄스를 제어하는 새로운 레이저 펄스 변조 기술을 고안하였다. 펄스 제어 장치는 레이저 공진기 외부에 설치된 가변 압력 챔버이며, 입력 레이저 펄스는 챔버 내부 가스 파괴를 유도하기 위해 가압 집광 된다. 역제동 광흡수에 의하여 출력 레이저 펄스의 시간적 후단은 흡수되지만, 전단은 플라스마의 영향을 받지 않고 순수하게 투과된다. 즉, 초점 부 광분해시 관측되는 강렬한 광흡수는

순간적으로 초점 매질을 불투명하게 하여 레이저 빔을 차단하는 가상적 셔터 역할을 수행할 수 있다. 가변 셔터링 시간은 셀 압력과 레이저 세기를 조절함으로써 제어되었으며, "레이저 셔터링 시간" 의존성 상관관계를 확립하였다.

종래의 LIBS 계측을 수행하기 위해 필요한 플라스마는 측정 대상 내에 화학 반응 증폭, 충격파, 급격한 온도 상승 등을 수반하기에 한정적인 환경에서만 사용되었다. 본 연구에서 개발한 펄스 폭 변조 기술은 이러한 한계를 뛰어넘는 최소 침습적 LIBS 를 개발하는데 응용되었다. 앞서 개발된 펄스 폭 변조 기술을 LIBS 계측에 적용하여 (1) 가스 분해 및 플라스마 생성을 효과적으로 유도하면서 (2) 동시에 유동 간섭을 억제하는 안정적인 LIBS 측정이 가능함을 증명하였다. 더욱이, 제안한 LIBS 측정 방식은 기존 방식에 비해 향상된 시공간 분해능을 제공하였다.

마지막으로, 본 연구에서 개발한 최소 침습적 LIBS 기술을 가연성이 매우 높은 유동 환경에서 수행하여 연구의 가능성 및 실효성을 효과적으로 입증하였다. 역제동 흡수식 제어를 통해 생성된 피코초 레이저 펄스는 LIBS 측정에 사용되었으며, 이를 통해 가연성 유동의 1, 2 차원 연료 농도 분포가 성공적으로 측정되었다.

주요어: 레이저 유도 플라스마, 광학 계측, 레이저 펄스 폭 제어, 플라스마 분광법

학번: 2015-22716